University of Strathclyde
Department of Naval Architecture, Ocean and Marine Engineering

Study on mixing, modelling and control of an SCR system

by

Xinna Tian

A thesis presented in fulfilment of the requirements
for the degree of Doctor of Philosophy

Glasgow, UK
June, 2016

This thesis is the result of the author's original research. It has been composed by the author and has not been previously submitted for examination which has led to the award of a degree.

To my parents, Guihai Tian & Xiaohua Xu

ABSTRACT

In recent years, more and more research attention has been paid to the NO_x emissions caused by marine diesel engines. Selective catalytic reduction (SCR) system has been proven to be an effective technology for the removal of NO_x emitted from marine diesel engines. In order to comply with stringent International Maritime Organization (IMO) Tier III NO_x emission regulations, a number of engine manufacturers have developed their own SCR systems with an option of installing SCR reactors before or after the turbines of engine turbochargers. This thesis focuses on modelling of evaporation and decomposition of urea-water-solution (UWS) droplets, design and optimisation of static mixers, modelling of an SCR reactor and developing model-based urea dosing control strategy.

The amount of ammonia converted from UWS has a significant effect on the NO_x removal efficiency of SCR systems. Due to a limited installation space for SCR systems on board, choosing the location of urea injection nozzle appropriately has become a critical issue for SCR system design. An evaporation and decomposition model of UWS droplets has been developed in this research in order to determine the total depletion time of a UWS droplet, which is helpful to calculate the proper length between the urea nozzle and reactor of an SCR system.

In order to achieve a high NO_x removal rate and reduce the quantity of NH_3 slip, static mixers are commonly used before SCR reactors to improve the mixing between ammonia and exhaust gases. 4 novel static mixers have been designed and the performance of the mixers is compared in the study. An experiment has been conducted to validate the mixing performance and pressure loss of the static mixers developed. It shows that there is a satisfied agreement between the simulation and experiment results.

A mathematical model of SCR reactors has been established. The unknown parameters of the model are identified by minimising the error between the model predicted and measured values of both the temperature and the species concentration

after the SCR reactor. The SCR reactor model is further used in a simulation for the purpose of developing model-based urea dosing control strategies.

A state observer is used to determine the actual states in the reactor which supplies the mandatory information for developing model-based urea dosing control strategies. The NH_3 cross-sensitivity of NO_x sensors can be described by a linear equation. The simulation results of the observer show that the NH_3 cross-sensitivity of NO_x sensors can be neglected when estimating the actual states of the reactor if NH_3 is of a low concentration in the exhaust.

ACKNOWLEDGEMENT

I would like to gratefully acknowledge various people who have been journeyed with me during my study on this thesis. First and foremost, my deepest gratitude and appreciation go to my supervisors, Professor Peilin Zhou and Professor Wenping Zhang, for their valuable suggestion and insightful guidance throughout my years of study at the University of Strathclyde and Harbin Engineering University. As a joint training student, I have been engaged in research groups both in the UK and China. My supervisors have always set the highest standards for me throughout the pursuit of this degree and provided me much appreciated support for smoothly conducting the research.

I am extremely grateful to Associate Professor Youhong Xiao whom I have collaborated with during the work at Harbin Engineering University. Whenever I encounter any problems either from the research or daily life he would help me without hesitation. His assistance and encouragement have helped me endure the hardest time of my research.

I also need to thank my teammates, Zhenhao Chu, Wei Zheng, Yanzhong Shao, Guofeng Zhao and Guoxue Lyu who have actively supported me and made the experimental work enjoyable.

I am deeply indebted to my parents Guihai Tian and Xiaohua Xu who always give me comfort and help throughout the study. Their love is the greatest gift that I have ever received.

Thanks are also due to Lloyd's Register the financial support from which is greatly appreciated.

Last but not least, I am grateful to my colleagues and friends who have accompanied me and given me such a warm atmosphere throughout the study.

CONTENTS

ABSTRACT I
ACKNOWLEDGEMENT III
CONTENTS IV
LIST OF FIGURES VIII
LIST OF TABLES XII
NOMENCLATURE XIII
Chapter 1. INTRODUCTION 1
1. 1 Background 1
1. 2 NO_x emission control technology 3
1. 3 Review of SCR systems for marine engines 4
1. 4 Aim and objectives of the project 8
1. 5 Outline of the thesis 10
Chapter 2. DECOMPOSITION OF UREA-WATER-SOLUTION 13
2.1 Modelling of depletion of UWS droplet 14
2.1.1 Evaporation of water 17
2.1.2 Decomposition of urea 23
2.1.3 Motion of droplet 24
2.2 Properties of medium 26
2.3 Numerical solution procedure 31
2.4 Numerical results and discussion 33
2.4.1 Comparison between evaporation of water and UWS droplets 33
2.4.2 Model validation 35
2.4.3 The effect of relative velocity on UWS droplet depletion time 36
2.4.4 Droplet motion 38
2.5 Chapter summary 40
Chapter 3. PERFORMANCE STUDY OF STATIC MIXERS 42
3.1 Introduction of static mixers 43
3.1.1 Working mechanisms of static mixers 43
3.1.2 Application status of static mixers 44
3.1.3 Evaluation indexes of static mixers 46

3.2 Experiment on static mixers 48
3.2.1 Experimental objectives 48
3.2.2 Experimental test rig 48
3.2.3 Experimental arrangement 51
3.2.4 Experimental results 52
3.3 Simulation on static mixers 54
3.3.1 3D modelling of static mixers 54
3.3.2 Case study 55
3.3.3 Evaluation of mixing quality and sampling points 55
3.3.4 Simulation results 56
3.4 Comparison between simulation and experiment 60
3.5 Analysis on the performance of static mixers 62
3.6 Chapter summary 70
Chapter 4. DYNAMIC MODELLING OF AN SCR REACTOR 71
4.1 Governing equations of monolithic catalyst 72
4.1.1 Introduction of monolithic catalyst 72
4.1.2 Heterogeneous reaction mechanism 73
4.1.3 Universal governing equation of fluid dynamics 74
4.1.4 Assumptions in monolithic catalyst 76
4.2 Modelling of an SCR reactor 79
4.2.1 Chemical kinetics model 79
4.2.2 3-state chemical dynamic equations 83
4.2.3 1-state chemical dynamic equations 84
4.2.4 Temperature equation 85
4.3 Implementation of modelling 86
4.3.1 Implementation of 3-state chemical dynamic equations 87
4.3.2 Implementation of 1-state chemical dynamic equations 89
4.3.3 Implementation of temperature equation 89
4.3.4 Boundary and initial conditions 90
4.4 Parameter estimation and model validation 90
4.4.1 Introduction of parameter estimation 90
4.4.2 Experiment for parameter estimation 92

4.4.3 Initial values of parameter estimation 95
4.4.4 Parameter estimation results 98
4.4.5 Model validation 99
4.5 Adequacy of 1-state chemical dynamic equations 107
4.6 Chapter summary 109
Chapter 5. MODEL-BASED UREA CONTROL STRATEGY 110
5.1 Basic rules of the urea dosing controller 110
5.2 Linearisation of nonlinear SCR model 112
5.3 Controllability and observability analysis 114
5.4 Sliding mode control 115
5.4.1 Sliding mode control theory 115
5.4.2 Desired NO concentration and desired NO conversion rate control strategies 117
5.4.3 Desired NH_3 slip control strategy 119
5.4.4 Sliding mode controller implementation 121
5.5 Optimal control 122
5.5.1 Optimal control theory 122
5.5.2 Optimal controller design 127
5.5.3 Optimal controller implementation 128
5.6 Simulation results 129
5.7 Chapter summary 133
Chapter 6. STATE ESTIMATION 135
6.1 NH_3 cross-sensitivity of NO_x sensors 135
6.2 State observer 137
6.3 Observer simulation 138
6.4 Chapter summary 143
Chapter 7. CONCLUSIONS AND RECOMMENDATIONS 144
7.1 Conclusions 144
7.2 Contributions 146
7.3 Innovations 147
7.4 Recommendations for future work 148
Publications. 149

References. 152
Appendix 1. SCR EXPERIMENTAL TEST RIG 164
Appendix 2. CATALYST PARAMETERS IN SCR REACTOR MODELLING .. 167
Appendix 3. COMPARISON OF UREA CONTROL STRATEGIES 168

LIST OF FIGURES

Figure 1-1 Maximum allowable NO_x emission for marine diesel engines 2
Figure 1-2 Map of global emission control areas [3] 3
Figure 1-3 Total number of vessels with SCR installations [14] 5
Figure 1-4 Operating temperature ranges of Johnson Matthey's SCR catalysts [20] .. 7
Figure 1-5 Interconnections of research topics 12
Figure 2-1 Infinite diffusion model for the droplet interior 17
Figure 2-2 Evaporation model of a UWS droplet 18
Figure 2-3 Numerical solution procedure 32
Figure 2-4 Comparison of the droplet surface temperature of water and UWS droplets during the evaporation processs under conditions: T_∞ =673K, ... 33
Figure 2-5 Evolution of the mass fractions of urea and water in a UWS droplet during the evaporation process under conditions: T_∞ =673K, P_∞ =0.11MPa, u_g =0, $T_{s,0}$ =300K, D_0 =70μm, u_d =0, Y_u =0.325, A =0.42kg/(s.m), E_a =6.9×10^{4}J/mol 34
Figure 2-6 Evolution of droplet surface temperature of a UWS droplet during the evaporation and thermolysis process under conditions: T_∞ =673K,..... 35
Figure 2-7 Evolution of squared diameter of a UWS droplet during the evaporation and thermolysis process under conditions: T_∞ =673K, P_∞ =0.11MPa, u_g =0, $T_{s,0}$ =300K, D_0 =70μm, u_d =0, Y_u =0.325, A =0.42kg/(s.m),..... 36
Figure 2-8 Evaporation time of a UWS droplet varying with relative velocity under conditions: T_∞ =673K, P_∞ =0.11MPa, $T_{s,0}$ =300K, D_0 =20μm, Y_u =0.325, A =0.42kg/(s.m), E_a =6.9×10^{4}J/mol 37
Figure 2-9 Total depletion time of a UWS droplet varying with relative velocity under conditions: T_∞ =673K, P_∞ =0.11MPa, $T_{s,0}$ =300K, D_0 =20μm, Y_u =0.325,..... 37
Figure 2-10 Travel distance of a UWS droplet throughout the whole depletion of the droplet under conditions: T_∞ =673K, P_∞ =0.11MPa, $T_{s,0}$ =300K, D_0 =20μm,..... 38

Figure 2-11 Evaporation time of a UWS droplet under conditions: P_{∞} =0.11MPa, $T_{s,0}$ =300K, Y_u =0.325, A =0.42kg/(s.m), E_a =6.9×10^{4}J/mol 39
Figure 2-12 Total depletion time of a UWS droplet under conditions: 40
Figure 3-1 Topsøe STAR® mixing system [69] 44
Figure 3-2 Sulzer mixers [70] 45
Figure 3-3 Alstom ammonia injection grid and IsoSwirl^{TM} mixers [71] 45
Figure 3-4 Experimental test rig for static mixers 49
Figure 3-5 Layout of experimental equipment 49
Figure 3-6 Sampling tubes and sampling points at each testing cross section 50
Figure 3-7 Layout of 7 testing sections along the pipeline 50
Figure 3-8 Assemblage of static mixers 52
Figure 3-9 CoV of NO concentration at each testing cross section 53
Figure 3-10 Simplified simulative model of static mixers 54
Figure 3-11 Schematic diagram of simulation 55
Figure 3-12 Locations of sampling points and distribution of NO concentration at a cross section of the pipeline 56
Figure 3-13 Contours of NO concentration distribution 57
Figure 3-14 Contours of velocity distribution 57
Figure 3-15 Contours of static pressure distribution 57
Figure 3-16 Comparison between surface integral method and sampling point method 59
Figure 3-17 Comparison between simulative and experimental pressure losses 60
Figure 3-18 Comparison between simulation and experiment in average NO concentration and the CoV of NO concentration 61
Figure 3-19 Simulative CoV of NO concentration at each analysed section 63
Figure 3-20 Fit curves of CoV of NO concentration after mixers 65
Figure 3-21 Values of B calculated based on each space interval after mixers 67
Figure 3-22 Gradients of B calculated based on each space interval after mixers 67
Figure 3-23 Average vorticity and CoV of axial velocity at each analysed section 68
Figure 4-1 A catalyst module packed with 4 monolithic catalyst elements 72
Figure 4-2 Two types of monolithic catalysts 73
Figure 4-3 Steps in a heterogeneous catalytic reaction [81] 74

Figure 4-4 3D monolithic catalyst model represented in Cartesian coordinates 77
Figure 4-5 2D axi-symmetric catalyst model represented in cylindrical coordinates 77
Figure 4-6 1D catalyst model represented with a single channel in axial direction .. 77
Figure 4-7 Parameter estimation process 91
Figure 4-8 Layout of experiment for parameter estimation 93
Figure 4-9 Validation of temperature under steady state engine operating points of 25% load (75 kW) and 100% load (300 kW) 100
Figure 4-10 Validation of species concentration under steady state engine operating points of 25% load (75 kW) and 100% load (300 kW) 101
Figure 4-11 Validation of temperature under steady state engine operating points of 50% load (150 kW) and 75% load (225 kW)..... 102
Figure 4-12 Validation of species concentration under steady state engine operating points of 50% load (150 kW) and 75% load (225 kW) 103
Figure 4-13 Validation of temperature under transient state engine operating condition..... 104
Figure 4-14 Validation of species concentration under transient state engine operating condition..... 105
Figure 4-15 Simulation relative errors for 1-state SCR model 108
Figure 5-1 Target NO_x conversion rate map 119
Figure 5-2 NO sliding mode control diagram 122
Figure 5-3 NH_3 sliding mode control diagram..... 122
Figure 5-4 Optimal control strategy diagram..... 129
Figure 5-5 Comparison of sliding mode control and optimal control strategies under steady state engine operating points of 25% load (75 kW) and 100% load (300 kW) 130
Figure 5-6 Comparison of sliding mode control and optimal control strategies under steady state engine operating points of 50% load (150 kW) and 75% load (225 kW) 131
Figure 5-7 Comparison of sliding mode control and optimal control strategies under transient state engine operating condition..... 132
Figure 6-1 Layout of experiment on NH_3 cross-sensitivity of NO_x sensor..... 136
Figure 6-2 Data fitting results of NH_3 cross-sensitivity of NO_x sensor 137

Figure 6-3 Tracking performance of observers to the actual states 140
Figure 6-4 Framework of comprehensive control simulation..... 141
Figure 6-5 Validation of observers in a comprehensive simulation 142

LIST OF TABLES

Table 1-1 MARPOL Annex VI NO_x emission limits 2
Table 1-2 Comparison of SCR systems from each manufacturer 8
Table 3-1 Repeatability of sensors 51
Table 3-2 Design specification of static mixers 52
Table 3-3 Values of B_{mixer} of the mixers 64
Table 3-4 Best fit results of A and B 65
Table 3-5 Pressure loss factor Z of static mixers 69
Table 4-1 The specific forms of ϕ, Γ and S in universal governing equation 76
Table 4-2 E3 test cycle for propeller-law-operated engine application 93
Table 4-3 Experimental operating points and NSR 95
Table 4-4 Kinetic parameters of SCR catalysts given in the references 97
Table 4-5 Estimation results of the parameters in the 3-state SCR model 99

NOMENCLATURE

Latin letters

A: Pre-exponential factor

A: System matrix

A: Coefficients

A_{cat}: Total area of exchange surface between monolithic catalyst and ambient, m^2

B: Input matrix

B: Coefficients to be fitted

B_{mixer}: Mixing ability coefficient of mixer

B_m: Mass transfer number

C: Output matrix

C: Concentration, mol/m^3

C_i: Measured values

$\hat{C}_i$: Estimated values

C_D: Drag coefficient

c_p: Thermal capacity, J/(kg.K)

D: Droplet diameter, m

D: Pipeline diameter, m

D: Diffusion coefficient, m^2/s

E: Activation energy, J/mol

e: The difference of the measured and desired concentration

$\vec{F}$: Forces acting on droplet, N

$\vec{f}$: The 3-state chemical dynamic equations

$\vec{g}$: Gravitational acceleration, m/s^2

H_u: Enthalpy of urea thermolysis reaction, J/kg

H: Hamiltonian function

h: Time step size

h: Heat transfer coefficient, $W/(m^2.K)$

i: Index of L/D

i: The number of the sample

J: Objective function

K_{cs}: Cross-sensitivity factor

K: Coefficient

k_B: Gradient of B

k: Reaction rate constant, s^{-1} or $m^3/(mol.s)$

L: Latent heat of vaporisation, J/kg

L: Pipeline length, m

L_{mixer}: Mixer length, m

$\vec{L}$: Observer gains

M: Molecular weight, kg/kmol

M: Coefficient

M_{cat}: Total mass of catalyst, kg

m: Droplet mass, kg

$\dot{m}$: Mass transfer rate, kg/(m^2.s)

$\dot{m}$: Mass flow rate, kg/s

n: Number of sampling points

n: Number of discretized cell

P: Pressure, Pa

P: Matrixes

$\overline{P}$: Matrixes

Q: Positive semi-definite real symmetric matrix, $Q = Q^T \geq 0$

Q: Volumetric flow rate, m^3/s

$\dot{Q}$: Heat transfer rate, W

$\bar{Q}$: Normalised flow rate, s^{-1}, $\bar{Q} = \frac{Q}{V}$

R: Positive definite real symmetric matrix, $R = R^T > 0$

R: Reaction rate, mol/(m^3.s)

R: Universal gas constant, R =8.314 J/(mol.K)

Re[]: Take the real part of a complex number

r: Radius of an arbitrary section surrounding droplet, m

S: Sliding surface

S: Free and active catalyst site

S: Source term

T: Temperature, K

t: Time, s

$\vec{u}$: Velocity, m/s

u: Urea injection amount

u: Input vector

U_O: Observability matrix

V: Opening volume of catalyst, m^3

W: Disturbance matrix

w_j: Ammonia concentration at a sampling point

$\bar{w}$: Average of ammonia concentration

$X_{l,w}$: Mole fraction of water in UWS droplet

x: State vector

$\hat{x}$: Estimated states

$\vec{x}_d$: Droplet travel distance, m

Y: Mass fraction

y: Output vector

y: Solution of the ODE

Greek letters

ρ:	Fluid density, kg/m^3
μ:	Dynamic viscosity, Pa s
φ:	Coefficient
λ:	Heat conductivity coefficient, W/(m·K)
$\lambda(t)$:	Co-state variable vector
$\lambda_i()$:	The eigenvalue of a matrix
λ:	Thermal conductivity, Pa.s
ξ:	Coefficient
α:	Coefficient
θ:	NH_3 surface coverage fraction
θ^*:	Coefficient
Ω:	NH_3 storage capacity of catalyst, mol/m^3
ϕ:	Universal variables
ϕ	Thickness of the boundary layer
γ:	Weighted factor
Γ:	Universal diffusion coefficient
η_{des}:	Desired NO concentration rate
ω:	Disturbance vector

Dimensionless numbers

Nu:	Nusselt number
Re:	Reynolds number
Pr:	Prandtl number
Le:	Lewis number

Superscripts and subscripts

∞:	Infinity
0:	Initial value
a:	Exhaust
ads:	Ammonia adsorption reaction
B:	Buoyancy
cat:	Catalyst
D:	Drag
d:	Droplet
des:	Ammonia desorption reaction
des:	Desired concentration
g:	Gas
i:	Position of L/D=i
in:	Inlet of a cell
j:	Species
l:	Liquid
Max:	Upper limitation
Min:	Lower limitation
m:	Mass
m:	Monolith
mix:	Mixture of water vapour and exhaust
n:	Time index
ox:	Ammonia oxidation reaction
st:	Standard SCR reaction
s:	Droplet surface
s:	Simulated
T:	Heat
t:	Tested
u:	Urea
u:	X direction
u:	Thermolysis
v:	Y direction
vap:	Vaporization
w:	Z direction
w:	Water vapour

Abbreviation

SCR:	Selective catalytic reduction
UWS:	Urea-water-solution
ECAs:	Emission control areas
EGR:	Exhaust gas recirculation
NTP:	Non-thermal plasma
CoV:	Coefficient of variation
CFD:	Computational fluid dynamics
NSR:	Normalised Stoichiometric Ratio

Chapter 1.

INTRODUCTION

1. 1 Background

Nitrogen oxides (NO_x) are harmful air pollutants formed during the combustion process of diesel engines. The majority of NO_x in exhaust are emitted in the form of nitrogen monoxide (NO) which accounts for approximate 90% of the NO_x emissions. NO can be oxidised easily to nitrogen dioxide (NO_2) in the atmosphere, thus NO and NO_2 are lumped together with the designation of NO_x. NO_x emissions can cause adverse effects on human bodies and environment.

NO_x emissions from shipping are reported at about 10 million tonnes per annum which is around 14% of the total global NO_x emissions from fossil fuel combustion [1][2]. The International Maritime Organization (IMO) has adopted an International Convention for the Prevention of Pollution from Ships, known as MARPOL 73/78, to prevent ship pollution. MARPOL Annex VI (regulations for the Prevention of Air Pollution from Ships) sets limits of NO_x and sulphur oxides (SO_x) emissions from ship exhaust. NO_x emission limits are divided into three 'tiers'. Tier I standard of NO_x emission regulation was adopted in 1997 while Tier II and Tier III standards were introduced by Annex VI amendments in 2008.

NO_x emission limits for diesel engines are set according to rated engine speed, as shown in Table 1-1 and presented graphically in Figure 1-1. Tier III standard is only applicable to NO_x emission control areas (ECAs) where are mapped in Figure 1-2.

Tier II standard applies outside the Tier III designated areas.

Table 1-1 MARPOL Annex VI NO_x emission limits

Tier	Ship construction date on or after	NO_x limit (g/kWh)		
		n<130 rpm	130≤ n <2000 rpm	n≥2000 rpm
Tier I	2000	17.0	$45 \cdot n^{-0.2}$	9.8
Tier II	2011	14.4	$44 \cdot n^{-0.23}$	7.7
Tier III	2016	3.4	$9 \cdot n^{-0.2}$	2.0

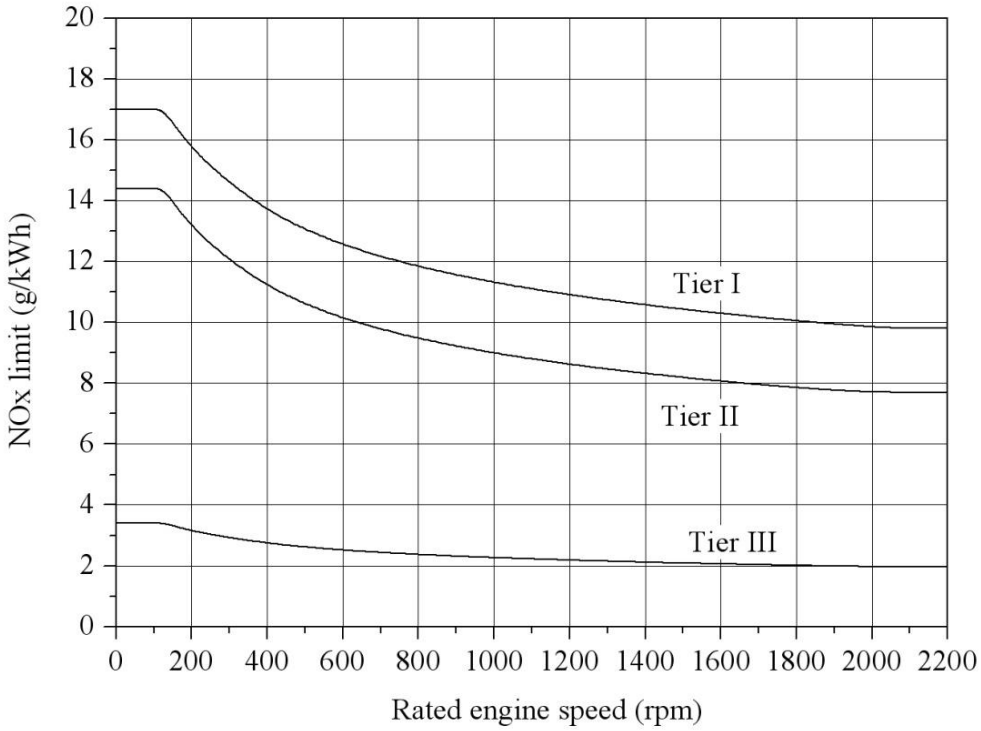

Figure 1-1 Maximum allowable NO_x emission for marine diesel engines

Figure 1-2 Map of global emission control areas [3]

1. 2 NO_x emission control technology

Generally, NO_x emission control technologies can be divided into two groups: primary methods and after-treatment methods [4]. Primary methods include those techniques which aim to prevent the formation of NO_x during the combustion process in the engine cylinder. In contrary to that, after-treatment methods focus on removing NO_x emissions from exhaust by a downstream cleaning device.

NO_x is formed from both atmospheric nitrogen (N_2) and nitrogen contained fuels under the environment of a high combustion temperature. Thus, primary methods address the NO_x emission control issue by using low nitrogen content fuel, lowering the peak combustion temperature, reducing oxygen partial pressure in cylinder and shortening the residence time of combustion at a high temperature. Lowering the maximum combustion temperature and reducing oxygen partial pressure can be conducted through charge air treatment including exhaust gas recirculation (EGR), charge air cooling and charge air humidification. Many design parameters of an engine, such as compression ratio, injection timing, injection rate profile and combustion chamber geometry, also have a noticeable effect on the reduction of NO_x.

It has been reported that a low NO_x emission can be obtained by retarding fuel injection timing, adopting pre-combustion chamber and reducing air-fuel ratio [5].

a

Studies on after-treatment methods for NO_x emission control remain mainly in non-thermal plasma (NTP) [6][7] and selective catalytic reduction (SCR) technologies [8][9][10][11]. NTP technology can achieve NOx reduction efficiency of 60% to 70% but with a fuel penalty around 6% due to the cost of electric power and addition of unburnt hydrocarbons for obtaining a high NO_x conversion efficiency [12]. SCR technology reduces NO_x emission by a chemical reactor with a NO_x removal efficiency over 90% possible with little or no fuel penalty [13]. Thus, SCR technology has been considered as a viable after-treatment method for marine diesel engines.

1. 3 Review of SCR systems for marine engines

The working principle of SCR technology is to reduce NO_x emissions in exhaust by injecting urea-water-solution into the exhaust pipeline. The ammonia (NH_3) generated from urea-water-solution will react with NO_x in SCR catalysts above a temperature of approximate 250˚C resulting in only N_2 and water (H_2O) being emitted to the atmosphere after SCR reactors. SCR systems are applicable to a wide range of engines which utilise fuels with different sulphur content and operate in different modes. A vessel operating worldwide is obligatory to comply with IMO Tier II standard where SCR systems may be shut off in this circumstance. However when the vessel enters into ECA zones, SCR systems are required to put into operation for compliance with IMO Tier III standard. SCR systems are commercially available from a range of manufactures. It has been reported that SCR systems have been installed on over 500 vessels during the last 30 years which is illustrated in Figure 1-3 [14].

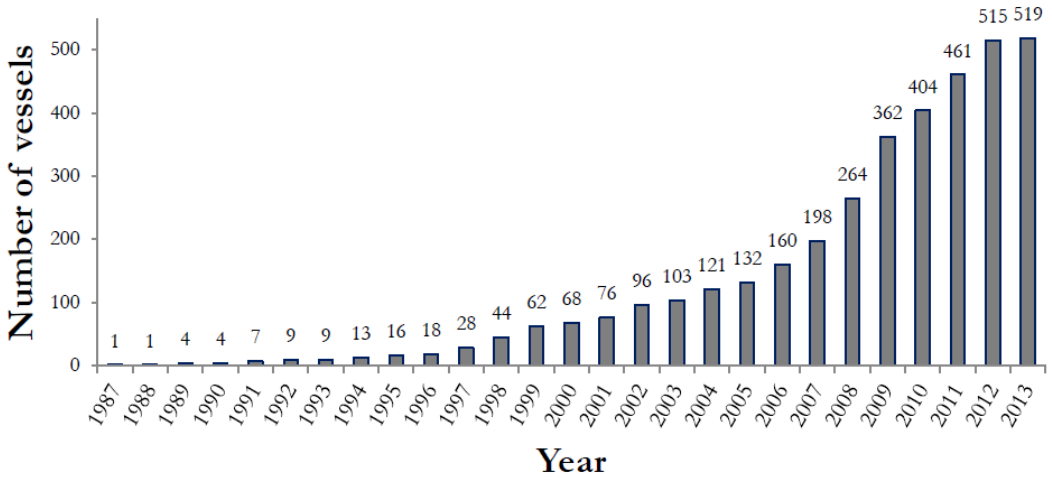

Figure 1-3 Total number of vessels with SCR installations [14]

There are two schemes of SCR system installation. One is placing SCR systems before the turbines of turbochargers, which results in a high temperature of exhaust in SCR pipelines. When high sulphur content oil used, NH_3 will react with sulphur to generate ammonium bisulphate which may block catalyst under a low temperature of exhaust gas (< 200°C). Thus for a low speed 2-stroke diesel engine, SCR systems are often installed before turbines to avoid the formation of ammonium bisulphate due to the low temperature of exhaust gas. When the catalyst works at a high temperature, the volume of catalyst can be reduced and thus less investment cost is required. However, this pre-turbine arrangement may have adverse impact on the efficiency of turbochargers due to the heat capacity of SCR reactors [15]. The other installation scheme is placing SCR systems after turbines with a much lower temperature of exhaust gas in SCR reactors. The post-turbine arrangement does not need to make changes to diesel engines but requires catalysts that could work under a low temperature environment.

MAN Diesel & Turbo

MAN Diesel & Turbo has successfully made 4-stroke marine engines to be IMO Tier III-compliant based on the SCR technology. In September 2014, DNV GL awarded the company a Tier III-compatibility certificate for its MAN 8L21/31

4-stroke engine. The engine alone meets IMO Tier II emission criteria whilst the SCR system makes the whole system compliant to the Tier III criteria [16].

The SCR system from MAN Diesel & Turbo is placed on the high pressure side of the turbine (before the turbine) in a turbocharger in order to utilise the high temperature of exhaust and thus allow a compact size of SCR catalyst. When operating in Tier II mode, the SCR system is cut off so that the exhaust passes directly to the turbocharger by a reactor bypass. When operating in Tier III mode, the SCR system will be engaged while the bypass will be closed.

Wärtsilä

Wärtsilä developed its own SCR system named the Wärtsilä NO_x Reducer (NOR). The Wärtsilä NOR was first released in 2009 and has now been further developed with a more compact and flexible design for easier installation onboard. The NOR operates at a temperature of 300 – 450 ℃, covering Wärtsilä medium-speed diesel engines for marine applications [17]. For a typical SCR system there is usually a bypass installed beside reactor. When the temperature of exhaust gas is under the minimum operating temperature of SCR catalyst, the valve before the reactor will be shut off and the exhaust will be guided into the bypass for the purpose of extending catalyst life. However, the Wärtsilä NOR make the bypass omissible by remaining soot blowing in operation even the reactor is not working.

DANSK TEKNOLOGI

DANSK TEKNOLOGI has manufactured and marketed the BLUNOX SCR system for marine diesel engines. By the end of 2011, six Royal Danish Navy patrol vessels named from ‘P520’ till ‘P525’ have been installed with the BLUNOX SCR systems which are in compliance with IMO Tier III standard [18]. Traditional SCR systems use air-assisted nozzle to inject urea-water-solution. However, the BLUNOX SCR system is more compact and economic due to using airless Twin Jet Nozzles [19].

Johnson Matthey

Johnson Matthey has equipped more than 120 engines over 30 ships worldwide with the SINOx® exhaust gas cleaning systems [20]. Johnson Matthey offers catalysts operating at temperatures between 200 ℃ and 500 ℃. The operating temperature ranges of SCR catalysts supplied by Johnson Matthey are shown in Figure 1-4.

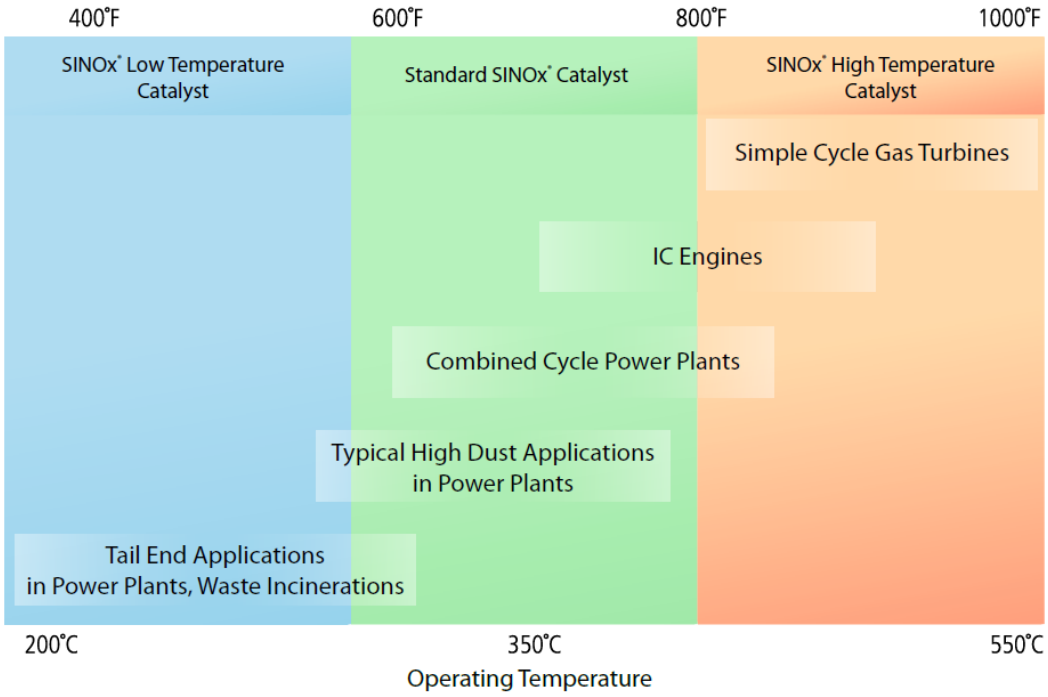

Figure 1-4 Operating temperature ranges of Johnson Matthey's SCR catalysts [20]

The SCR systems from each manufacturer are summarised in Table 1-2.

Table 1-2 Comparison of SCR systems from each manufacturer

	MAN Diesel & Turbo	**Wärtsilä**	**DANSK TEKNOLOGI**	**Johnson Matthey**
Diesel engine	Low-speed	Medium-speed	Wide range	Wide range
Installation	Before turbine	After turbine	After turbine	After turbine
Reactor size	Compact	Regular	Compact	Regular
Urea injecton	Air-assisted	Airless	Airless	Air-assisted
SCR cut off / Bypass operating condition	Tier II mode	Bypass not used	Tier II mode	Tier II mode

The after-turbine SCR system is investigated in the thesis. The diesel engine uses low sulphur fuel with the sulphur concentration of 0.05 wt % during engine operation. Thus, the adverse effect of sulphur on the NO_x conversion rate of the SCR system is not considered in the study.

1. 4 Aim and objectives of the project

The aim of this study is to deal with the problems that may be encountered during the design of an SCR system including determining the location of a urea nozzle, promoting the distribution uniformity of ammonia (NH_3) and calculating urea dosing rate. The results of the study are beneficial to the design of an SCR system.

Urea-water-solution (UWS) is used commonly as the reductant for SCR systems. The UWS injected in exhaust will evaporate and decompose to NH_3 which actually takes part in SCR reactions. The distance between UWS nozzle and reactor may affect the decomposition process of UWS and thus affect the concentration of NH_3 in

the reactor. Therefore, the evaporation and decomposition of a UWS droplet are modelled in this thesis in order to determine the optimal distance between the UWS nozzle and reactor for the purpose of obtaining a complete conversion of urea to NH_3 in the reactor.

The distribution of NH_3 in the reactor has a significant effect on the NO_x conversion rate of a reactor and the amount of NH_3 slip. Thus, a uniform distribution of NH_3 is pursued in the design of an SCR system. Static mixers are widely used in SCR systems before reactors to promote the mixing of NH_3 and exhaust. Some of the existing static mixers on the market are of a satisfied mixing performance, but many of them may cause excessively high pressure loss which can affect engines' performance. Therefore, 4 novel static mixers are developed in this thesis to deal with the mixing problem.

In order to predict the NO_x conversion rate and the amount of NH_3 slip of the SCR system, an SCR reactor model is established in this thesis. The reactor model is developed based on the mechanism of SCR reactions on the catalyst and calibrated by experiments. The reactor model are further used for developing model-based urea control strategies which are beneficial to limiting excessive NH_3 slip during the abrupt temperature rising operating condition of an engine. The model-based urea control strategies require full information of the states in the reactor. Thus, a state observer is established in order to estimate the values of the states.

The objectives of the study are summarised below.

- Develop a depletion model of UWS droplets to calculate the optimal distance between urea nozzle and reactor for the purpose of complete conversion of urea to NH_3 before the reactor.

- Design efficient static mixers in order to obtain a uniform distribution of NH_3 before the reactor for the purpose of improving NO_x reduction rate. Uniform

NH_3 distribution before the reactor is also the foundation of 1-dimensional modelling of the reactor.

- Establish a reactor model to predict the NO_x reduction rate and the amount of NH_3 slip of an SCR system.

- Develop urea dosing control strategies based on the reactor model to achieve a high conversion rate of NO_x and avoide excessive NH_3 slip of an SCR system.

1. 5 Outline of the thesis

Outline of the forthcoming chapters is given below.

- Chapter 2 deals with the evaporation and decomposition of UWS droplets. The evaporation and decomposition process of a UWS droplet in exhaust pipe is simulated by implementing a Matlab scripts program.

- Chapter 3 designs 4 novel static mixers to address the mixing between NH_3 and exhaust gas before SCR reactors. An experiment is conducted to evaluate the mixing performance and pressure losses of each static mixer.

- Chapter 4 establishes a mathematical model of an SCR reactor. The unknown parameters of the model are estimated using the least-squares fitting method based on experimental data.

- Chapter 5 develops model-based urea dosing control strategy.

- Chapter 6 shows NH_3 cross-sensitivity of NO_x sensors and establishes a state observer which provides the information of the states in the SCR reactor model for developing model-based urea dosing control strategies.

- Chapter 7 presents conclusions and recommendations of this study and recommendations for future research.

The interconnections of the research topics are given below.

The urea decomposition model in chapter 2 and the performance study of static mixers in chapter 3 are the foundation of 1D modelling of the SCR reactor which is in chapter 4. This is because that it assumes complete conversion of urea to ammonia in the reactor and the ammonia distributes homogeneously in the reactor. Thus, chapter 2 ensures complete conversion of urea to ammonia by calculating the optimal distance between the urea nozzle and the reactor. Chapter 3 ensures homogeneous distribution of ammonia by installing static mixers before the reactor.

The reactor model established in chapter 4 is the foundation of developing model-based urea control strategies because it provides the knowledge of the controlled system which is necessary for the design of a controller in chapter 5. The reactor also provides the knowledge of the unknown states in the reactor which is necessary for the design of a state estimator in chapter 6.

Model-based control strategies require full information of the states in the reactor. However, some of the states like the ammonia surface coverage fraction in the catalyst cannot be measured by sensors. Thus, the state estimator established in chapter 6 provides the information of the ammonia surface coverage fraction for the controller designed in chapter 5.

The interconnections of the research topics are demonstrated in Figure 1-5.

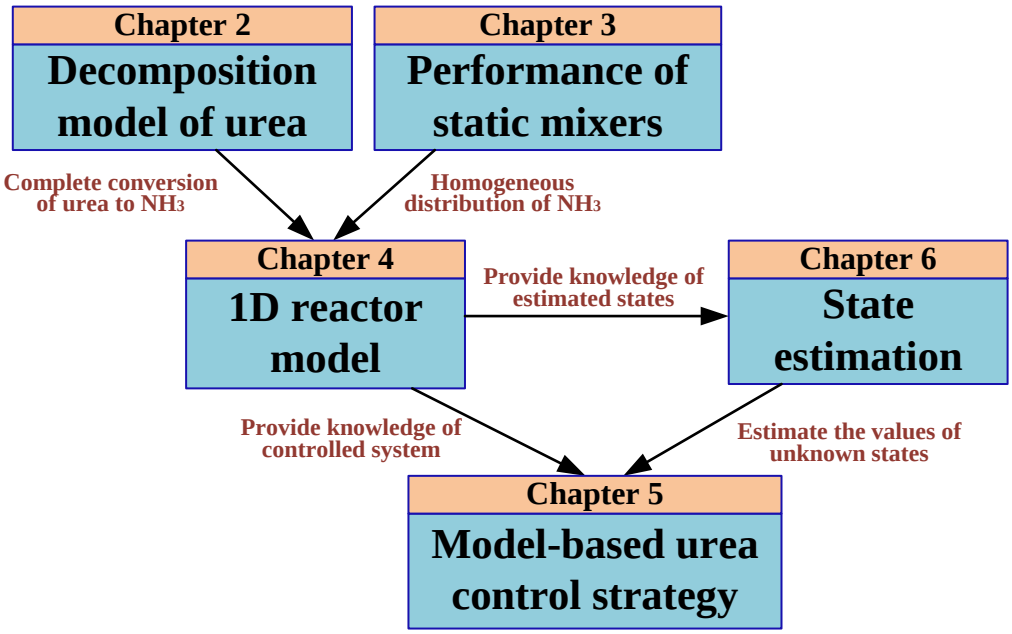

Figure 1-5 Interconnections of research topics

Chapter 2.

DECOMPOSITION OF UREA-WATER-SOLUTION

Injection of urea-water-solution (UWS) into the pipelines before SCR reactors is a widely used method for generating ammonia (NH_3) which actually takes part in the NO_x reducing reactions in SCR catalysts. UWS usually contains urea of concentration of 32.5 wt % for automobile applications because the UWS has the lowest crystallization temperature at this concentration. However, UWS of a concentration of 40 wt % of urea is often used for marine SCR systems.

This chapter is focused on investigating the optimal distance between UWS nozzle and reactor from the perspective of UWS droplet evaporation and decomposition. A numerical model describing UWS droplet evaporation and decomposition is established and the simulation is implemented in MATLAB. A droplet motion equation is solved in the model and the result of droplet travel distance can be used to determine the optimal distance between UWS nozzle and reactor. Section 2.1 gives a brief review of studies on modelling of UWS droplet and equations incorporated in the model. Section 2.2 calculates the properties of medium and section 2.3 illustrates the procedure of numerical solution. The simulation results are presented in section 2.4.

2.1 Modelling of depletion of UWS droplet

The position where UWS nozzle should be located is important to the design of an SCR system because it may affect the conversion rate of urea to ammonia. If the distance between UWS nozzle and reactor is not long enough, the UWS droplets injected will probably not evaporate and decompose completely by the time when it reaches the reactor. The amount of ammonia converted from UWS droplets has a significant influence on SCR conversion efficiency. Incomplete decomposition of UWS droplets will result in insufficient supply of ammonia for the SCR reactions, hence, reduce the NO_x conversion efficiency. Besides, the deposits generated during UWS decomposition combined with undecomposed urea will stick to the surface of catalysts. This may block the flow and degrade the performance of catalysts [21]. Therefore it is necessary to calculate the optimal position of UWS nozzle in order to ensure that the UWS droplets injected in exhaust evaporate completely and the solid or molten urea decomposes at least into gas NH_3 and HNCO when it reaches the reactor. Smeets *et al.* [22] calculated the theoretical reactor length in which UWS droplets can evaporate completely and decompose into HNCO and NH_3. Yu [21] presented a graph describing the distance that the UWS droplets in various diameters need to evaporate completely under different temperature. Abu-Ramadan *et al.* [23] denoted that the distance between UWS nozzle and catalyst is of a length of 1.5 to 7 times of the exhaust pipe diameter. However, the exact evaporation and decomposition time of UWS droplets have not been presented in previous publications.

Developing a reliable numerical model capable of predicting the depletion of UWS droplets is complicated because two components exist throughout the evaporation and decomposition process of UWS droplets. However, several researchers have conducted experiments on the decomposition process of either pure solid urea or UWS, which can be used to develop numerical models. Lundström *et al.* [24] conducted a set of experiments of urea thermolysis. The results of the experiments showed that the water in UWS droplets evaporates from approximate 25˚C to 90˚C, urea melts at 133˚C, and the decomposition of urea takes place in a temperature

range of 150˚C to 210˚C. The thermolysis reaction of urea becomes obvious when the temperature of urea is above 152˚C. The experiments conducted by Yim *et al.* [25] showed that urea decomposes completely into NH_3 and HNCO at 350˚C when the residence time of urea in the flow is longer than 0.1 s. Wang *et al.* [26] investigated the evaporation behaviour of UWS droplets using suspended droplets, which helps to understand the evaporation characteristics of UWS droplets.

The products generated during the evaporation and decomposition of UWS droplets are mainly NH_3 and HNCO. Deposits in front of catalysts have been observed in many urea-SCR systems [27][28]. It is reported that the formation of deposits is the result of an inappropriate design of UWS spray [27][28][29]. Several authors [30][31][32][33][34] have reported that the formation of high molecular compounds degrades the performance of SCR systems by sticking to the catalyst surface and consuming a part of urea which results in insufficient ammonia left for the NO_x reduction reactions [33]. These complex phenomena render the modelling of the decomposition of UWS droplets complicated. From the perspective of engineering applications, a simple depletion model of UWS droplets is used in this study. The generation of high molecular compounds during the process of urea breakdown is omitted. It assumes that the consumption of pure solid urea happens when the water from UWS droplets has evaporated completely. Thus, the mechanism of UWS decomposition is simplified as the following steps:

Step 1: Complete evaporation of water in a UWS droplet, leading to the formation of pure solid urea and water vapour.

$$(NH_2)_2CO(\text{aq.sol.}) \rightarrow (NH_2)_2CO(\text{s or l}) + xH_2O(g) \qquad \textbf{(2-1)}$$

Step 2: Thermolysis of pure solid urea into equimolar amounts of ammonia and isocyanic acid.

$$(NH_2)_2CO(\text{s or l}) \rightarrow NH_3(g) + HNCO(g) \qquad \textbf{(2-2)}$$

Step 3: Hydrolysis of isocyanic acid into ammonia and carbon dioxide.

$$HNCO(g)+H_2O(g) \rightarrow NH_3(g)+CO_2(g) \quad \textbf{(2-3)}$$

The isocyanic acid formed during the thermolysis process is stable enough to remain totally unreactive until it reaches the catalyst surface. However, Kleemann *et al.* [35] reported that the overall hydrolysis rate of HNCO on SCR catalysts is about two orders of magnitude higher than the SCR reaction rate. Yim *et al.* [25] also observed that SCR catalyst is able to hydrolyse HNCO rapidly to NH_3 even at a temperature of as low as 150˚C. The hydrolysis of HNCO to NH_3 can also occur without catalyst if the reaction temperature is sufficiently high (≥400˚C) [36]. In this study, the hydrolysis of isocyanic acid is not considered in the design of the length between UWS nozzle and reactor because that both NH_3 and HNCO are in gas phases. They won't block the flow and HNCO can be hydrolysed to NH_3 rapidly with the presence of SCR catalyst. Thus, only water evaporation and pure solid urea thermolysis are concerned in the modelling.

The depletion of water in UWS droplet can be described as an evaporation process whilst the urea depletion in UWS droplet can be modelled by three ways: an evaporation process, an Arrhenius expression, or a conversion efficiency factor [23][37][38][39][40][41]. Birkhold *et al.* [37][38] proposed a two-stage depletion model of UWS droplet, in which it assumes that urea decays after complete water evaporation. Abu-Ramadan *et al.* [23] simulated the depletion of UWS droplet as a multicomponent vaporization model instead of separating the decomposition process into two distinct and consecutive processes. Strӧm *et al.* [41] modelled the decomposition process as a heat transfer limited process at a constant temperature of 152˚C.

Previous studies have shown the UWS decomposition time at a specific temperature [23] and the length needed for UWS evaporation [21]. However, there is not enough referential data in engineering application for the design of the location of a urea nozzle. Thus, this chapter aims to provide the evaporation and decomposition time of

UWS droplets in various diameters under different temperature. The travel distance of UWS droplet calculated is helpful to determining the distance between the urea nozzle and reactor. In this study, Birkhold's theory is used to model the depletion process of UWS droplet due to its easy implementation, but with a droplet motion equation incorporated additionally.

2.1.1 Evaporation of water

The mass transfer rate of water evaporated from UWS droplet is limited by the heat transfer process during the entire evaporation. The evaporation rate of water is related to the pressure, temperature and fluid regime of exhaust, initial temperature and diameter of the droplet, and the relative velocity between the droplet and exhaust. Some assumptions are made to simplify the evaporation model. The UWS droplet is treated as a perfect sphere and no distorting happens during the process of water evaporation and urea thermolysis. This is because that the relative velocity between the droplet and exhaust is small at the beginning of urea decomposition in comparison with the high viscosity of the melted urea, which will effectively slow down any development of droplet deformation [41]. The infinite diffusion model (rapid mixing model) is used in the numerical model, which assumes infinitely high diffusivities of heat and interspecies for the liquid phase [42][43]. The infinite diffusion model is presented in Figure 2-1.

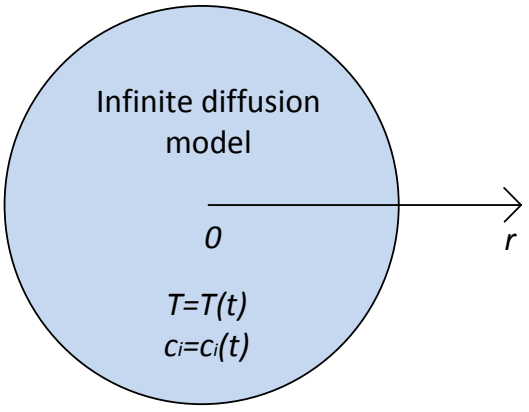

Figure 2-1 Infinite diffusion model for the droplet interior

The infinite diffusion model means that the distribution of the temperature *T* and the species concentration *ci* in the droplet are spatially uniform and temporally varying. The radiative heat between the droplet and environment is neglected. It is postulated that there is a gas film surrounding the UWS droplet where both water vapour and exhaust exist in the mixture film. The droplet surface is thus an interface of liquid and gas phases. A schetch of the evaporation model of a UWS droplet is demonstrated in Figure 2-2. The symbols presented in Figure 2-2 will be introduced and used in the following sections.

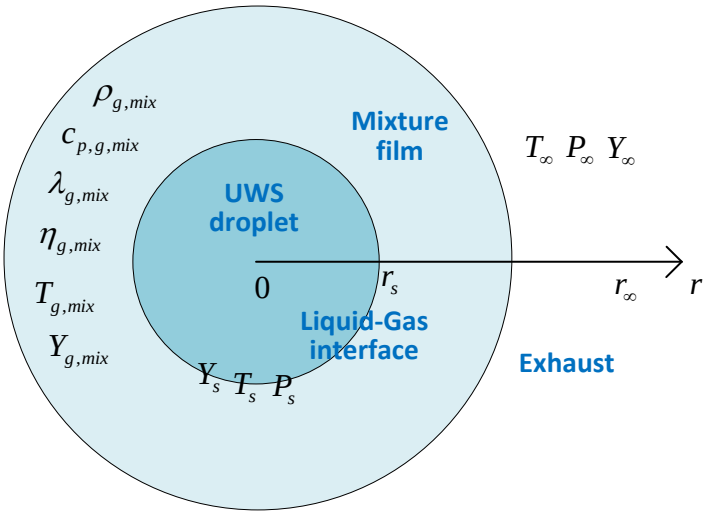

Figure 2-2 Evaporation model of a UWS droplet

1) Mass transfer modelling

Assuming the evaporation process of the droplet to be quasi-steady, the evaporation rate of vaporising water can be expressed as [44]:

$$\dot{m}_d = -\rho_{g,mix} D_c \frac{dY}{dr} + Y \cdot \dot{m}_d$$
$$\Rightarrow \dot{m}_d = -\rho_{g,mix} D_c \frac{1}{1-Y} \frac{dY}{dr} \quad \textbf{(2-4)}$$

Where:

$\dot{m}_d$: Mass transfer rate of vaporising water at an arbitrary section surrounding droplet, kg/(m^2.s)

$\rho_{g,mix}$: Density of the mixture of water vapour and exhaust, kg/m^3

D_c : Mass diffusion coefficient, m^2/s

Y : Mass fraction of water vapour at an arbitrary section surrounding droplet

r : Radius of an arbitrary section surrounding droplet, m

According to mass conservation, the mass transfer rate of vaporising water at an arbitrary section surrounding droplet equals to the mass transfer rate at droplet surface, there is,

$$\begin{aligned} & 4\pi r_s^2 \dot{m}_{d,s} = 4\pi r^2 \dot{m}_d \\ & \Rightarrow \dot{m}_d = \frac{r_s^2}{r^2} \dot{m}_{d,s} \end{aligned} \quad \textbf{(2-5)}$$

Where:

$\dot{m}_{d,s}$: Mass transfer rate of vaporising water at droplet surface, kg/(m^2.s)

r_s : Droplet radius, m

Combining Equation (2-4) with Equation (2-5), it obtains:

$$\dot{m}_{d,s} r_s^2 \frac{1}{r^2} dr = -\rho_{g,mix} D_c \frac{1}{1-Y} dY \quad \textbf{(2-6)}$$

The evaporation process model is subject to the following boundary conditions:

$$r = r_s,\ Y = Y_s; \quad \textbf{(2-7)}$$

$$r = r_\infty,\ Y = Y_\infty = 0; \quad \textbf{(2-8)}$$

Where:

r_∞ : Radius at infinity, m

Y_s : Mass fraction of water vapour at droplet surface

Y_∞ : Mass fraction of water vapour at infinity

By taking the integral of Equation (2-6) within the boundaries shown in Equations (2-7) and (2-8) it obtains:

$$\int_{r_s}^{r_\infty} \dot{m}_{d,s} r_s^2 \frac{1}{r^2} dr = \int_{Y_s}^{Y_\infty} -\rho_{g,mix} D_c \frac{1}{1-Y} dY \qquad \textbf{(2-9)}$$

Thus, the following equation for calculating mass transfer rate of vaporising water at droplet surface is obtained:

$$\dot{m}_{d,s} = -\left[\rho_{g,mix} D_c \ln(1-Y_s) \right] / r_s \qquad \textbf{(2-10)}$$

The mass transfer number B_m is calculated as:

$$B_m = \frac{Y_s}{1-Y_s} \qquad \textbf{(2-11)}$$

Where:

B_m : Mass transfer number

The ratio of thermal diffusivity to mass diffusivity is defined as the Lewis number which is shown in Equation (2-12):

$$Le = \frac{\lambda_{g,mix}}{\rho_{g,mix} D_c c_{p,g,mix}} \qquad \textbf{(2-12)}$$

If Le is assumed to equal 1, $\rho_{g,mix} D_c$ can be replaced by $\lambda_{g,mix}/c_{p,g,mix}$. Thus, the temporal changing rate of droplet mass is obtained as:

$$\frac{dm}{dt} = 4\pi r_s^2 \dot{m}_{d,s} = 2\pi D \left(\frac{\lambda_{g,mix}}{c_{p,g,mix}} \right) \ln(1 + B_m) \quad \textbf{(2-13)}$$

Where:

m : Droplet mass, kg

t : Time, s

$\lambda_{g,mix}$: Thermal conductivity of the mixture of water vapour and exhaust, W/(m. K)

D : Droplet diameter, m

$c_{p,g,mix}$: Thermal capacity of the mixture of water vapour and exhaust, J/(kg.K)

Le : Lewis number

2) Heat transfer modelling

The heat transferred from the exhaust to droplet is consumed by the heating process of the droplet and water vaporisation.

$$\dot{Q}_{g,s} = \dot{Q}_l + \dot{Q}_{vap} \quad \textbf{(2-14)}$$

Where:

$\dot{Q}_{g,s}$: Heat transfer rate from exhaust to droplet, W

$\dot{Q}_l$: Heat transfer rate of droplet heating, W

$\dot{Q}_{vap}$: Heat transfer rate of vaporisation, W

The heat transfer rate from the exhaust to droplet is expressed in terms of heat transfer coefficient, which can be nondimensionalised by a Nusselt number.

$$\dot{Q}_{g,s} = 4\pi r_s^2 h\left(T_\infty - T_s\right) = \pi DNu\lambda_{g,mix}\left(T_\infty - T_s\right) \quad \textbf{(2-15)}$$

Where:

h : Heat transfer coefficient, W/(m^2.K)

Nu : Nusselt number

T_∞ : Exhaust temperature, K

T_s : Droplet temperature, K

The thermal power used to heat up the droplet is written as:

$$\dot{Q}_l = mc_{p,l}\frac{dT_s}{dt} \quad \textbf{(2-16)}$$

Where:

$c_{p,l}$: Heat capacity of the droplet, J/(kg.K)

The power consumed by water vaporisation is:

$$\dot{Q}_{vap} = L\frac{dm}{dt} = 2\pi DL\left(\frac{\lambda_{g,mix}}{c_{p,g,mix}}\right)\ln(1+B_m) \quad \textbf{(2-17)}$$

Where:

L : Latent heat of vaporisation, J/kg

Thus the temporal differential of the droplet temperature can be obtained based on Equations (2-14) to (2-17):

$$\frac{dT_s}{dt} = \frac{\pi DNu\lambda_{g,mix}\left(T_\infty - T_s\right) - 2\pi DL\left(\frac{\lambda_{g,mix}}{c_{p,g,mix}}\right)\ln(1+B_m)}{mc_{p,l}} \quad \textbf{(2-18)}$$

2.1.2 Decomposition of urea

It is reported that urea starts to decompose at a temperature of a range from 406K to 433K [31][34][45][46][47], resulting in the formation of isocyanic acid and ammonia. In a current study, it is assumed that after all water is vaporised from UWS droplet, the pure solid urea left begins to decompose when the droplet reaches a temperature of 425K [31]. There is no mass exchange under the temperature of 425K. To describe the rate of urea decomposition, an Arrhenius expression can be used:

$$\frac{dm_u}{dt} = -\pi DAe^{(-E_a/RT_s)} \quad \textbf{(2-19)}$$

Where:

m_u : Urea mass, kg

A : Pre-exponential factor, kg/(s.m)

E_a : Activation energy, J/mol

R : Universal gas constant, R =8.314 J/(mol.K)

The kinetic parameters of urea decomposition are chosen from the work of Birkhold *et al.* [38] who obtained the values of kinetic parameters by least squares fitting method using experimental data:

$$A = 0.42 \text{ kg/(s.m)} \quad \textbf{(2-20)}$$

$$E_a = 69000 \text{ J/mol} \quad \textbf{(2-21)}$$

Since water does not exist in the UWS droplet after vaporisation, the heat transferred to the droplet is thus used for heating up the droplet and urea decomposition. The heat balance equation can be expressed as:

$$\dot{Q}_{g,s} = \dot{Q}_l + \dot{Q}_u \quad \textbf{(2-22)}$$

The reaction heat needed for urea thermolysis reaction can be calculated from:

$$\dot{Q}_u = -H_u \frac{dm_u}{dt} \quad \textbf{(2-23)}$$

Where:

$\dot{Q}_u$: Heat transfer rate of urea thermolysis reaction, W

H_u : Enthalpy of urea thermolysis reaction, J/kg

2.1.3 Motion of droplet

The droplet trajectory equation that used to determine the travel distance of a droplet, is written in terms of the derivative of position vector:

$$\frac{d\vec{x}_d}{dt} = \vec{u}_d \quad \textbf{(2-24)}$$

Where:

$\vec{x}_d$: Droplet travel distance, m

$\vec{u}_d$: Droplet velocity, m/s

By analysing the relevant forces acting on a droplet, the momentum transfer between the droplet and exhaust can be calculated according to the Newton's second law of motion:

$$m\frac{d\vec{u}_d}{dt} = \sum \vec{F} \quad \textbf{(2-25)}$$

Where:

$\vec{F}$: Forces acting on droplet, N

Drag force and buoyancy force are the most concerned two forces acting on the droplet. Other forces can be ignored compared to the two forces [27][48].

Drag force is calculated as:

$$\vec{F}_D = C_D \frac{\pi D^2}{4} \frac{\rho_g \left|\vec{u}_g - \vec{u}_d\right| \left(\vec{u}_g - \vec{u}_d\right)}{2} \quad \textbf{(2-26)}$$

Where:

$\vec{F}_D$: Drag force, N

C_D : Drag coefficient

ρ_g : Exhaust density, kg/m^3

$\vec{u}_g$: Exhaust velocity, m/s

For a spherical droplet, a well-known correlation is available for calculating the droplet drag coefficient [49].

$$C_D = \begin{cases} \frac{24}{Re_d}\left(1 + 0.15 Re_d^{0.687}\right) & Re_d < 1000 \\ 0.44 & Re_d \geq 1000 \end{cases} \quad \textbf{(2-27)}$$

Where:

Re_d : Reynolds number

Buoyancy force is described as:

$$\vec{F}_B = m \frac{\vec{g}\left(\rho_d - \rho_g\right)}{\rho_d} \quad \textbf{(2-28)}$$

Where:

$\vec{F}_B$: Buoyancy force, N

$\vec{g}$: Gravitational acceleration, m/s^2

ρ_d: Droplet density, kg/m^3

Combining Equations (2-25), (2-26) and (2-28), the momentum balance equation of the droplet is rewritten by:

$$\frac{d\vec{u}_d}{dt} = \frac{3}{4}\frac{\rho_g}{\rho_d}\frac{C_D}{D}\left|\vec{u}_g - \vec{u}_d\right|\left(\vec{u}_g - \vec{u}_d\right) + \left(1 - \frac{\rho_g}{\rho_d}\right)\vec{g} \qquad \textbf{(2-29)}$$

Since the exhaust will gain momentum from the droplet when the droplet loses velocity by drag force, the velocity change of the exhaust will have significant effect on the momentum exchange process. However, the amount of UWS droplets is substantially less than that of exhaust gas in SCR systems. Thus, it is assumed that the motion of exhaust gas is not affected by UWS droplets and there is no momentum obtained from UWS droplets.

2.2 Properties of medium

The mass fraction of urea in a UWS droplet increases with the evaporation of water. Most of the properties of medium of the UWS droplet are temporal varying with the droplet temperature, thus varying property correlations are used in the simulation. The mass fraction of water vapour at the droplet surface can be determined from the Raoult's law [50]:

$$Y_s = \frac{P_s X_{l,w} M_w}{P_s X_{l,w} M_w + \left(P_\infty - P_s X_{l,w}\right) M_a} \qquad \textbf{(2-30)}$$

Where:

P_s : Saturation pressure of water vapour at droplet surface, Pa

P_∞ : Exhaust pressure, Pa

$X_{l,w}$: Mole fraction of water in UWS droplet

M_w : Molecular weight of water, kg/kmol

M_a : Molecular weight of exhaust, kg/kmol

The saturation pressure of water vapour at the droplet surface is associated with droplet temperature according to Clausius-Clapeyron equation [51]:

$$P_s = 1000 \exp\left(16.4116 - \frac{3891.69}{T_s - 43}\right) \quad \textbf{(2-31)}$$

The qualitative temperature of the mixture film and the mass fraction of water vapour in the mixture film are evaluated using the 1/3 mixing rule [52]:

$$T_{g,mix} = T_s + \frac{1}{3}(T_\infty - T_s) \quad \textbf{(2-32)}$$

$$Y_{g,mix,w} = Y_s + \frac{1}{3}(Y_\infty - Y_s) \quad \textbf{(2-33)}$$

$$Y_{g,mix,a} = 1 - Y_{g,mix,w} \quad \textbf{(2-34)}$$

Where:

$T_{g,mix}$: Qualitative temperature of the mixture of water vapour and exhaust

$Y_{g,mix,w}$: Mass fraction of water vapour in the mixture of water vapour and exhaust

$Y_{g,mix,a}$: Mass fraction of exhaust in the mixture of water vapour and exhaust

The dynamic viscosity of the mixture film is calculated as [53]:

$$\mu_{g,mix} = \frac{M_w Y_{g,mix,w} \mu_{g,w}}{M_w Y_{g,mix,w} + M_a Y_{g,mix,a} \varphi_{w,a}} + \frac{M_a Y_{g,mix,a} \mu_{g,a}}{M_a Y_{g,mix,a} + M_w Y_{g,mix,w} \varphi_{a,w}} \quad \textbf{(2-35)}$$

Where:

$\mu_{g,a}$: Dynamic viscosity of exhaust, Pa.s

$\mu_{g,w}$: Dynamic viscosity of water vapour, Pa.s

$\mu_{g,mix}$: Dynamic viscosity of the mixture of water vapour and exhaust, Pa.s

$\varphi_{w,a}$: Coefficient

$\varphi_{a,w}$: Coefficient

The coefficients $\varphi_{w,a}$ and $\varphi_{a,w}$ are calculated as follow:

$$\varphi_{w,a} = \left[1 + \left(\frac{\mu_{g,w}}{\mu_{g,a}}\right)^{1/2} \cdot \left(\frac{M_w}{M_a}\right)^{1/4}\right]^2 \Bigg/ \left[8\left(1 + \frac{M_a}{M_w}\right)\right]^{1/2} \quad \textbf{(2-36)}$$

$$\varphi_{a,w} = \varphi_{w,a} \frac{\mu_{g,w}}{\mu_{g,a}} \frac{M_w}{M_a} \quad \textbf{(2-37)}$$

The thermal conductivity of the mixture film is calculated as [53]:

$$\lambda_{g,mix} = \frac{M_w Y_{g,mix,w} \lambda_{g,w}}{M_w Y_{g,mix,w} + M_a Y_{g,mix,a} \xi_{w,a}} + \frac{M_a Y_{g,mix,a} \lambda_{g,a}}{M_a Y_{g,mix,a} + M_w Y_{g,mix,w} \xi_{a,w}} \quad \textbf{(2-38)}$$

Where:

$\lambda_{g,a}$: Thermal conductivity of exhaust, W/(m. K)

$\lambda_{g,w}$: Thermal conductivity of water vapour, W/(m. K)

$\lambda_{g,mix}$: Thermal conductivity of the mixture of water vapour and exhaust, W/(m. K)

$\xi_{w,a}$: Coefficient

$\xi_{a,w}$: Coefficient

The coefficients $\xi_{w,a}$ and $\xi_{a,w}$ are calculated as follow:

$$\xi_{w,a} = \left[1+\left(\frac{\eta_{g,w}}{\eta_{g,a}}\right)^{1/2}\cdot\left(\frac{M_a}{M_w}\right)^{1/4}\right]^2 \Bigg/ \left[8\left(1+\frac{M_w}{M_a}\right)\right]^{1/2} \quad \textbf{(2-39)}$$

$$\xi_{a,w} = \left[1+\left(\frac{\eta_{g,a}}{\eta_{g,w}}\right)^{1/2}\cdot\left(\frac{M_w}{M_a}\right)^{1/4}\right]^2 \Bigg/ \left[8\left(1+\frac{M_a}{M_w}\right)\right]^{1/2} \quad \textbf{(2-40)}$$

The specific heats for both liquid and gas phases can be obtained by:

$$c_{p,g,mix} = c_{p,g,w}Y_{g,mix,w} + c_{p,g,a}Y_{g,mix,a} \quad \textbf{(2-41)}$$

Where:

$c_{p,g,mix}$: Thermal capacity of the mixture of water vapour and exhaust, J/(kg.K)

$c_{p,g,w}$: Thermal capacity of water vapour, J/(kg.K)

$c_{p,g,a}$: Thermal capacity of exhaust, J/(kg.K)

The initial density of the UWS droplet is determined by an experimental correlation which is obtained from an experiment carried out in Harbin Engineering University under the pressure of 1 atm and temperature of 20˚C. At each time step during the simulation, the droplet mass and droplet diameter are obtained first. The droplet density is calculated by dividing the droplet mass by its diameter. The droplet temperature varies temporally throughout the simulation. The properties of the droplet are temperature dependent and are calculated starting from the saturation pressure of water vapour at the droplet surface which is shown in Equation (2-31). The correlation of the initial density of the UWS droplet is presented in below:

$$\rho_d = 1000\left(0.283Y_u + 0.9952\right) \quad \textbf{(2-42)}$$

Where:

ρ_d : Initial droplet density, kg/m^3

Y_u : Mass fraction of urea in UWS droplet

The density of the mixture film can be determined by the following equation:

$$\rho_{g,mix} = \frac{\rho_{g,w}\rho_{g,a}}{\rho_{g,w}Y_{g,mix,a} + \rho_{g,a}Y_{g,mix,w}} \quad \textbf{(2-43)}$$

Where:

$\rho_{g,mix}$: Density of the mixture of water vapour and exhaust, kg/m^3

$\rho_{g,w}$: Density of water vapour, kg/m^3

$\rho_{g,a}$: Density of exhaust, kg/m^3

The Nusselt number is obtained by the correlation [41]:

$$Nu = 2 + 0.552 Re^{1/2} \cdot Pr^{1/3} \quad \textbf{(2-44)}$$

Where:

Nu : Nusselt number

Re : Reynolds number

Pr : Prandtl number

The latent heat of vaporisation of the water depends on the droplet temperature [54]:

$$L = 1000 exp\left(\frac{647.3 - T_s}{247.15}\right)^{0.3237} \quad \textbf{(2-45)}$$

The urea decomposition includes the sublimation and thermolysis of urea. Thus a combined equivalant enthalpy of 3096 kJ/kg is used as the enthalpy of urea decomposition [41].

$$H_u = 3096 \text{ kJ/kg} \quad \textbf{(2-46)}$$

2.3 Numerical solution procedure

The temporal evolutions of droplet temperature and concentration are evaluated by using a MATLAB simulation code. The mass and temperature differential equations of a UWS droplet are discretized using the Euler explicit finite difference method. To compromise the accuracy of the solution results and computational time, a time step of 10^{-6} s is used in the simulation to save the simulation running time. Figure 2-3 shows the numerical solution procedure.

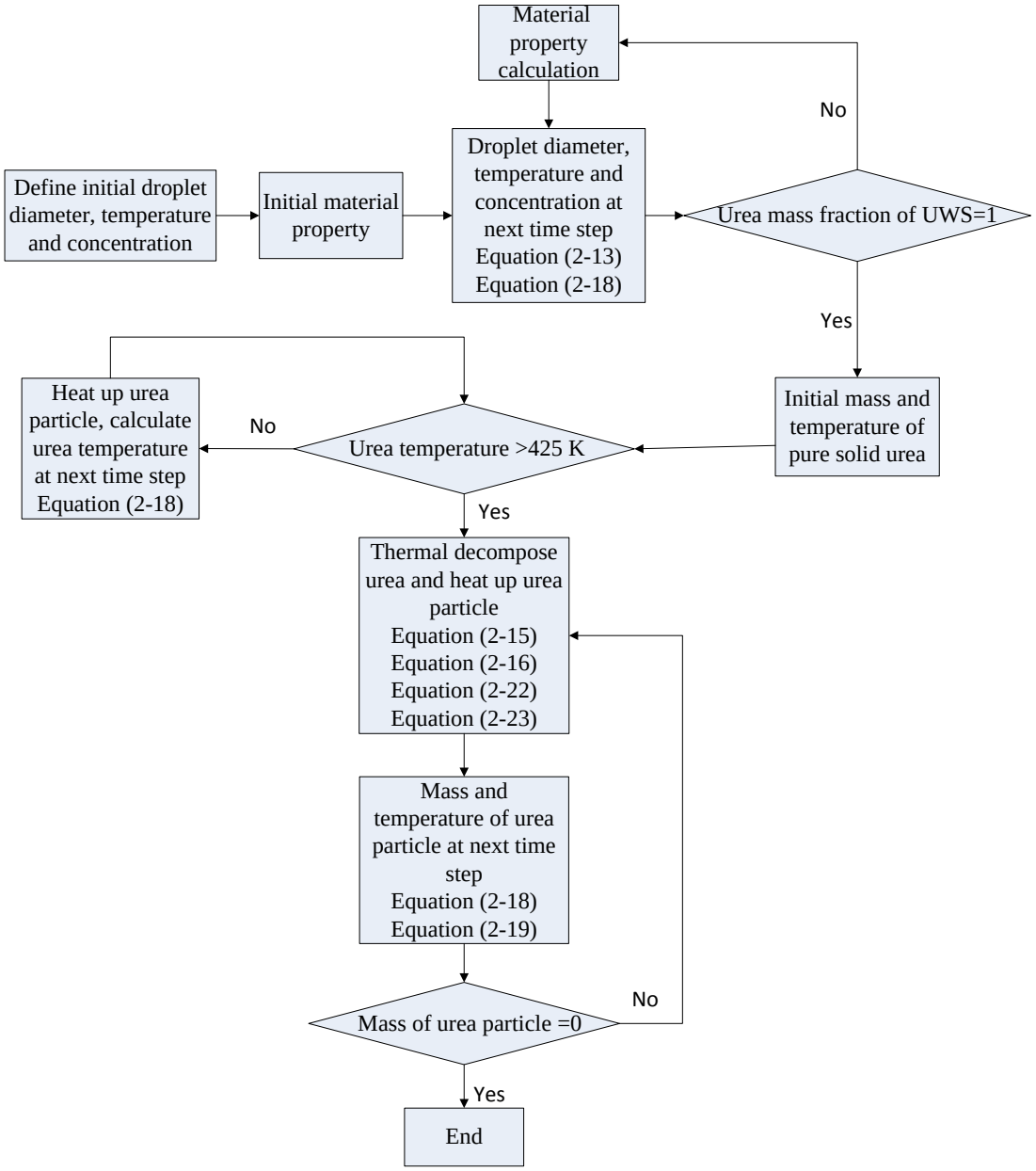

Figure 2-3 Numerical solution procedure

2.4 Numerical results and discussion

2.4.1 Comparison between evaporation of water and UWS droplets

The evaporation models of both water and UWS droplets have been established in this study. They are simulated under the same conditions for the purpose of comparison. The operating conditions are set as T_∞=673K, P_∞=0.11MPa, and u_g=0. The initial conditions for both the droplets are $T_{s,0}$=300K, D_0=70μm and u_d=0. The urea concentration in the UWS droplet is Y_u=0.325, and the kinetic parameters of urea thermolysis are A=0.42kg/(s.m), E_a=6.9×10^4 J/mol.

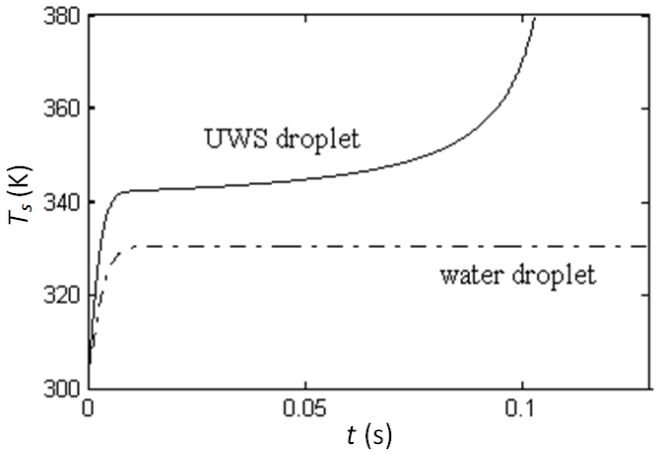

Figure 2-4 Comparison of the droplet surface temperature of water and UWS droplets during the evaporation processs under conditions: T_∞=673K, P_∞=0.11MPa, u_g=0, $T_{s,0}$=300K, D_0=70μm, u_d=0, Y_u=0.325, A=0.42kg/(s.m), E_a=6.9×10^{4}J/mol

Figure 2-4 presents that the temperature of both the droplets during the evaporation process increases rapidly at the beginning of evaporation. This is because that the heat transfer rate of a droplet is much higher than its mass transfer rate at the beginning of evaporation. During this period, the heat transferred to the droplets will be used for both heating up the droplets and evaporation. When the saturated

temperature of water vapour is reached, all the heat transferred to the water droplet will be used for evaporation and the temperature of the water droplet will remain a constant Compared to that, the temperature of the UWS droplet increases continuously throughout the evaporation process. This is because that the existence of urea in the UWS droplet decreases the pressure of water vapour at droplet surface, yielding a smaller evaporation rate of water vapour from the UWS droplet and thus less cooling due to evaporation.

Another difference between the water and UWS droplets is that the UWS droplet contains two components which are urea and water. The evaporation of water results in the urea concentration of the UWS droplet changing with the process of evaporation, which makes the properties of the UWS droplet time dependent. The evolution of the mass fractions of urea and water in the UWS droplet is depicted in Figure 2-5. It can be seen from the figure that the urea in the UWS droplet is of a concentration of 32.5 wt % at the beginning of evaporation. The urea concentration increases continually with the evaporation of water from the UWS droplet until all water has been evaporated at the time point of t =0.11s.

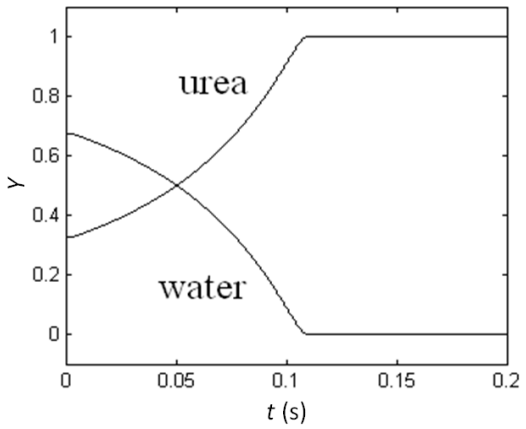

Figure 2-5 Evolution of the mass fractions of urea and water in a UWS droplet during the evaporation process under conditions: T_∞**=673K,** P_∞**=0.11MPa,** u_g**=0,** $T_{s,0}$**=300K,** D_0**=70μm,** u_d**=0,** Y_u**=0.325,** A**=0.42kg/(s.m),** E_a**=6.9×10^{4}J/mol**

2.4.2 Model validation

The numerical model of the decomposition of a UWS droplet developed in this study is validated by comparing its results with that reported by Birkhold *et al.* [38]. Figure 2-6 and Figure 2-7 show a comparison between the simulation results and Birkhold *et al*'s study. The operating conditions are set as the same values where T_∞=673K, P_∞=0.11MPa, and u_g=0. The droplet initial conditions are $T_{s,0}$=300K, D_0=70μm, u_d=0, Y_u=0.325, and the kinetic parameters of urea thermolysis are A =0.42kg/(s.m), E_a=6.9×10^{4}J/mol.

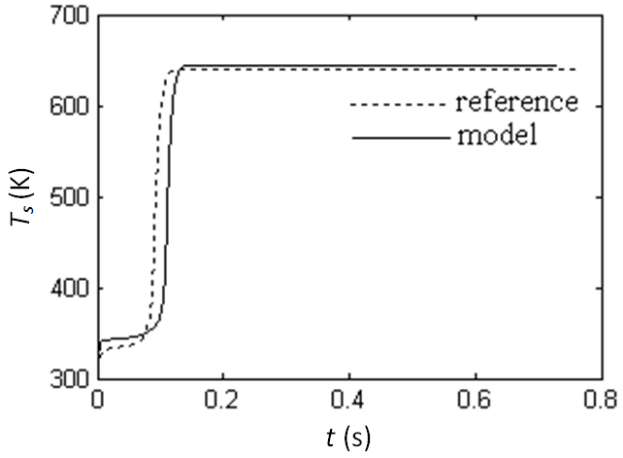

Figure 2-6 Evolution of droplet surface temperature of a UWS droplet during the evaporation and thermolysis process under conditions: T_∞=673K, P_∞=0.11MPa, u_g=0, $T_{s,0}$=300K, D_0=70μm, u_d=0, Y_u=0.325, A=0.42kg/(s.m), E_a=6.9×10^{4}J/mol

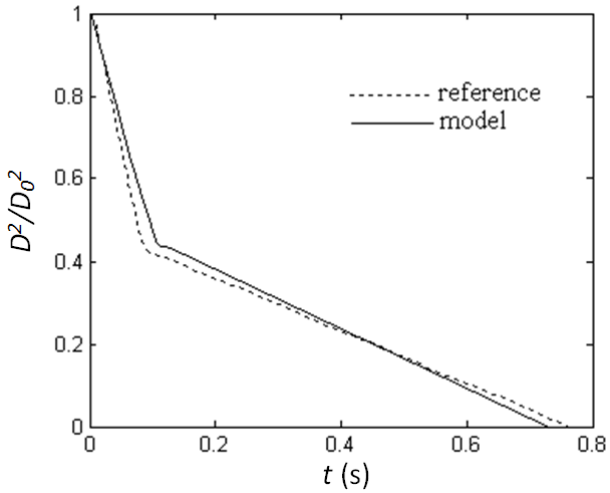

Figure 2-7 Evolution of squared diameter of a UWS droplet during the evaporation and thermolysis process under conditions: T_∞ =673K, P_∞ =0.11MPa, u_g =0, $T_{s,0}$ =300K, D_0 =70μm, u_d =0, Y_u =0.325, A =0.42kg/(s.m), E_a =6.9×10^{4}J/mol

It can be seen from Figure 2-6 and Figure 2-7 that both the droplet surface temperature and the droplet diameter obtained from the model agree well with Birkhold's data. The differences between the results of the two models may be caused by the medium properties calculated. Furthermore, the process of extracting data from Birkhold's graphs may also contribute to the errors. However, the results of the two models show the same changing trend. Thus, the accuracy of the model developed in this work is acceptable for engineering applications.

2.4.3 The effect of relative velocity on UWS droplet depletion time

The model developed is used to predict the travel distance, evaporation time and total depletion time of a UWS droplet of 20μm in diameter with various exhaust velocity values and initial droplet velocity values under the conditions of T_∞ =673K, P_∞ =0.11MPa, $T_{s,0}$ =300K, Y_u =0.325, A =0.42kg/(s.m), E_a =6.9×10^{4}J/mol. The varying tendencies of the evaporation time and total depletion time of a UWS droplet are plotted in Figure 2-8 and Figure 2-9.

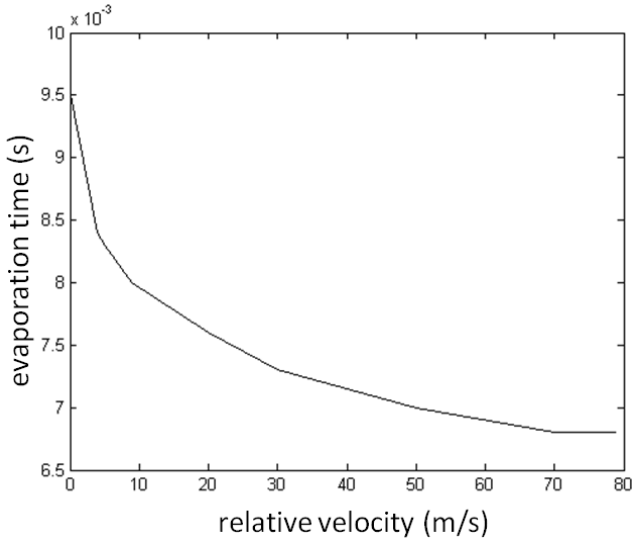

Figure 2-8 Evaporation time of a UWS droplet varying with relative velocity under conditions: T_∞=673K, P_∞=0.11MPa, $T_{s,0}$=300K, D_0=20μm, Y_u=0.325, A =0.42kg/(s.m), E_a=6.9×10^{4}J/mol

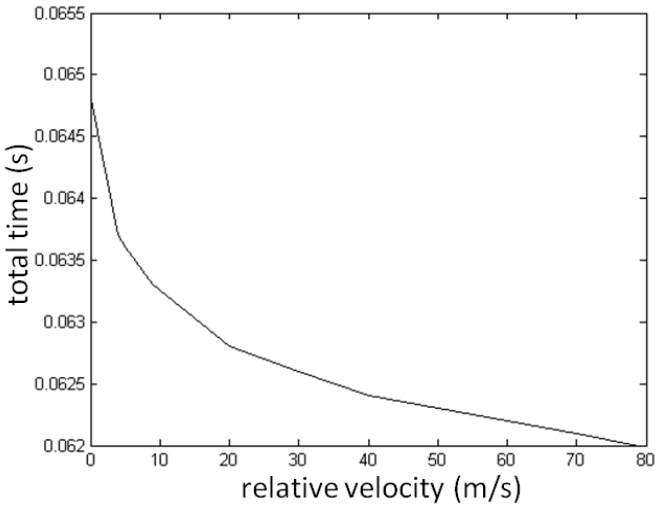

Figure 2-9 Total depletion time of a UWS droplet varying with relative velocity under conditions: T_∞=673K, P_∞=0.11MPa, $T_{s,0}$=300K, D_0=20μm, Y_u=0.325, A =0.42kg/(s.m), E_a=6.9×10^{4}J/mol

It can be seen from Figure 2-8 and Figure 2-9 that the evaporation time and total depletion time of the UWS droplet are related to the relative velocity between the

droplet and exhaust. A high relative velocity results in a short depletion time for the UWS droplet of a specific size. This is because that a high relative velocity results in a large value of the Reynolds number. The strong convective heat exchange between the UWS droplet and exhaust makes the droplet evaporate fast. When the relative velocity is zero, the droplet needs the longest time to evaporate.

2.4.4 Droplet motion

The total depletion time of a UWS droplet depends on the relative velocity between the droplet and exhaust. However, the travel distance of a UWS droplet depends on both the exhaust velocity and droplet initial velocity. The travel distance of a UWS droplet increases with an increase in either the exhaust velocity or the droplet initial velocity. This is much more obvious when increasing the exhaust velocity because that the mass of the droplet is much smaller compared to that of the exhaust. The droplet will reach the velocity of the bulk exhaust after a period of acceleration or deceleration. Thus, the exhaust velocity is critical to the travel distance of the UWS droplet. The travel distance of a UWS droplet is depicted in Figure 2-10.

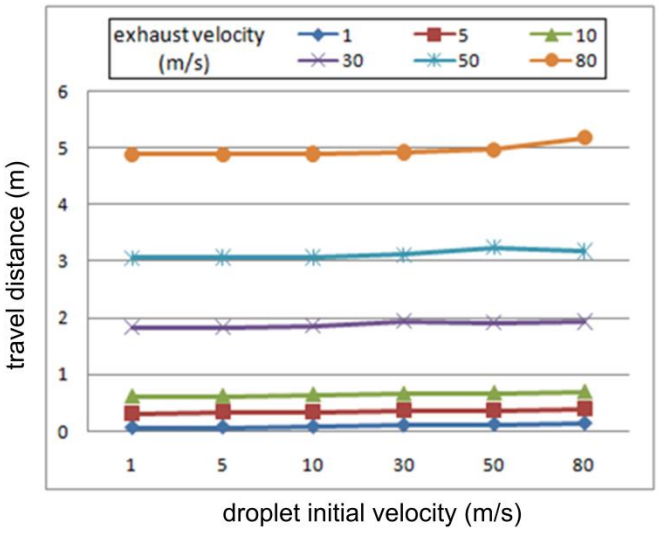

Figure 2-10 Travel distance of a UWS droplet throughout the whole depletion of the droplet under conditions: T_∞ **=673K,** P_∞ **=0.11MPa,** $T_{s,0}$ **=300K,** D_0 **=20μm,** Y_u **=0.325,** A **=0.42kg/(s.m),** E_a **=6.9×10^{4}J/mol**

When the droplet initial velocity equals to the exhaust velocity, the relative velocity between the droplet and exhaust is zero. Thus the travel distance of the droplet can be obtained easily by multiplying the total depletion time of the droplet and exhaust velocity. Nevertheless, if the relative velocity exists, the acceleration and deceleration processes of the droplet may need to be taken into account. Figure 2-11 and Figure 2-12 present the evaporation time and total depletion time of UWS droplets with different diameters under varying exhaust temperature when the relative velocity between the droplet and exhaust is zero. The results can be used for calculating the travel distance of a UWS droplet or designing the distance between the nozzle and reactor of an SCR system.

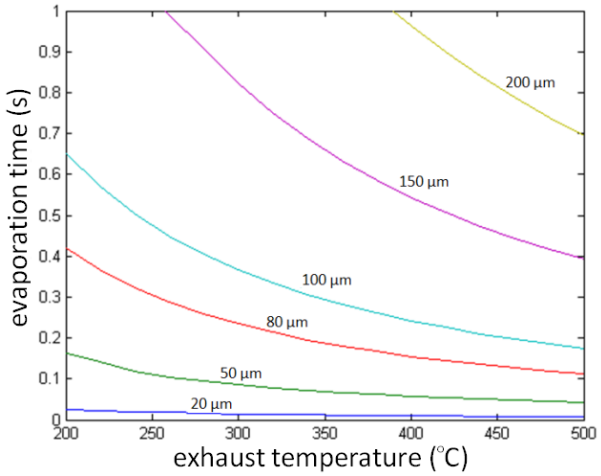

Figure 2-11 Evaporation time of a UWS droplet under conditions: P_{∞} =0.11MPa, $T_{s,0}$ =300K, Y_u =0.325, A =0.42kg/(s.m), E_a =6.9×10^{4}J/mol

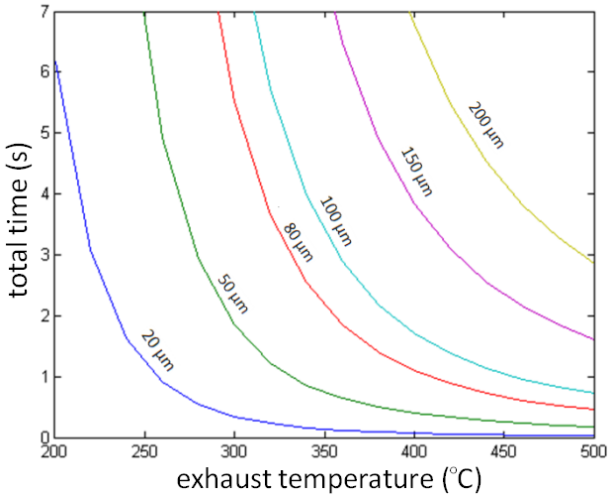

Figure 2-12 Total depletion time of a UWS droplet under conditions:
P_∞ =0.11MPa, $T_{s,0}$ =300K, Y_u =0.325, A =0.42kg/(s.m), E_a =6.9×10^{4}J/mol

Figure 2-11 and Figure 2-12 show that both the evaporation time and total depletion time of a UWS droplet depend heavily on the droplet diameter and exhaust temperature. A droplet of a large size needs more time to decay, thus, it may travel far away from the nozzle. When the exhaust temperature increases, the reaction rate of urea thermolysis rises exponentially. That can result in an abrupt slope of the total depletion time of the UWS droplet as shown in Figure 2-12.

2.5 Chapter summary

The travel distance of a UWS droplet depends on the total droplet depletion time, bulk exhaust velocity and droplet initial velocity. The UWS droplet can travel far away from the nozzle with a long depletion time, a high bulk exhaust velocity and a high droplet initial velocity. There are many factors that can influence the droplet depletion time, including the droplet diameter, the mass fraction of urea in the UWS droplet, the relative velocity between the droplet and exhaust, the pressure and temperature of exhaust, and the temperature of the droplet. Even with the same depletion time, the droplet travel distance can change significantly with the exhaust velocity. However, the effect of the initial droplet velocity on the droplet travel distance is minor as shown in Figure 2-10. Thus, the droplet travel distance can be

obtained easily by multiplying the total droplet depletion time and bulk exhaust velocity. The velocity of the exhaust in engine pipeline ranges from approximate 30 m/s to 50 m/s. The simulation results presented in Figure 2-10 suggest that a distance from 2m to 3m is recommended for the design of the distance between the urea nozzle and the reactor for an SCR system.

The numerical model developed in this study is calculated under an exhaust temperature of 673K which is a high operating temperature for an SCR system. The total depletion time and droplet travel distance provided in the study can be regarded as the minimum values to be satisfied when choosing the location of a UWS nozzle under a lower exhaust temperature. Thus, the distance between the UWS nozzle and SCR reactor should be longer than this value if possible in order to obtain a complete decomposition of urea to ammonia.

Chapter 3.

PERFORMANCE STUDY OF STATIC MIXERS

Chapter 2 investigates the evaporation and decomposition process of a UWS droplet, which can be used to design the optimal distance between UWS nozzle and reactor. The urea injected in exhaust will decompose to ammonia that takes part in SCR reactions in the reactor. However, the distribution of ammonia in the exhaust may not be even before it reaches the reactor. Thus, static mixers are widely used in SCR systems before reactors to promote the mixing of ammonia and exhaust stream. The volume rate of ammonia to exhaust can be smaller than 1/100. It is difficult to mix ammonia and exhaust uniformly at such a difference in flow rate under a short length of exhaust pipe. Although turbulence can help ammonia homogenisation, its influence is limited under certain conditions. The coefficient of variation (CoV) of ammonia before catalysts may have a significant influence on SCR conversion efficiency. Thus, it is necessary to improve the uniformity of ammonia distribution.

A brief review of the application status and evaluation indexes are introduced in section 3.1, followed by the investigations on the performance of static mixers, including self-designed and commercial static mixers, by both simulation and experiment in sections 3.2 and 3.3. The results are compared and analysed in sections 3.4 and 3.5.

3.1 Introduction of static mixers

Compared with dynamic mixers, static mixers have the advantages of low energy consumption and less pressure loss. Furthermore, they are much easier to install due to no moving parts in structures, and can be generally used for mixing fluids in a wide range of Reynolds number [55][56]. With the development of computational fluid dynamics (CFD) software, the design cycle and cost of static mixers can be significantly reduced and the optimisation of static mixers can be efficiently realised by adopting numerical simulation.

Studies of static mixers have mainly focused on revealing mixing mechanisms [55], optimizing the structures of static mixers [57][58] and evaluating the performance of static mixers [59][60][61]. Using a numerical simulation that is supported by an experiment is an effective way of investigating the characteristics of static mixers. The characteristics of static mixers varies depending on its application, but the characteristics primarily considered are the heat transfer ability [62][63][64], pressure loss [65], flow uniformity [66] and mixing homogenisation [67][68].

3.1.1 Working mechanisms of static mixers

The working mechanisms of static mixers can be divided into the following categories:

- Change flow volume by utilising abrupt expansion and contraction structures.
- Divert fluids and recombine them.
- Change flow direction by setting baffles.
- Increase the residence time of flow by utilising a maze structure.
- Generate swirling vortexes by inserting obstructions in flow.

3.1.2 Application status of static mixers

Some static mixers manufacturers have developed their products specifically for the SCR application. Topsøe [69] performed the mixing system design of STAR® for the SCR DeNO$_x$ unit on the Taishan power plant in China. The STAR® mixing system shown in Figure 3-1 is proved a very efficient mixer which has a low system pressure loss. Sulzer [70] has over 40 years' experience in the design of static mixers. Products such as CompaX^{TM}, SMV^{TM}, SMI^{TM} and Contour^{TM} (see Figure 3-2) have been prepared for SCR systems in order to increase the homogenisation of mixing. Alstom [71] developed a high efficient ammonia injection grid and the IsoSwirl™ mixer (see Figure 3-3) in order to meet the stringent NO$_x$ emission requirements. The IsoSwirl™ mixer ensures a thoroughly homogenous mixing of injected urea with exhaust.

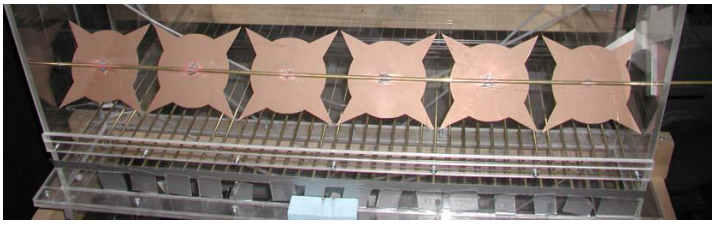

Figure 3-1 Topsøe STAR® mixing system [69]

Figure 3-2 Sulzer mixers [70]

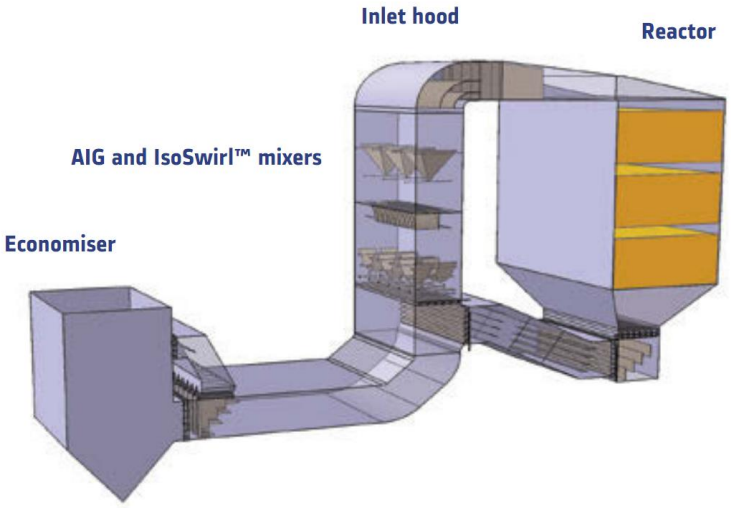

Figure 3-3 Alstom ammonia injection grid and IsoSwirl™ mixers [71]

Some of the existing static mixers on the market are of a satisfied mixing performance, but many of them may cause excessively high pressure loss which may

affect engine performance. Therefore, it is necessary to investigate more efficient static mixers which are applicable for marine SCR systems.

3.1.3 Evaluation indexes of static mixers

An evaluation standard must be established in order to evaluate the performance of static mixers. The following factors are generally taken into consideration when evaluating a static mixer.

Pressure drop

Pressure drop is one of the most important factors that must be considered when designing static mixers. A dimensionless parameter, referred as Z factor, is commonly used to evaluate the pressure loss of the flow generated by static mixers. Z factor is defined as the ratio of pressure drop over a static mixer to that over an empty pipe without a static mixer installed of the same length as the static mixer [65]. However, it can often be seen that a marine SCR reactor is combined with a muffler. Thus, the pressure loss of an SCR system comes not only from the reactor, but also from the structure of the muffler. This therefore puts forward a much more rigorous limitation for the design of static mixers. Under operational conditions, a limitation of pressure loss of 800 Pa for static mixers is recommended here since the maximum backpressure for an engine may be around 3 kPa.

Mixing distance

The concept of mixing distance means the distance between the nozzle where ammonia is injected and the section where a homogeneous mixing of the ammonia and exhaust is reached. This value represents the distance that needed for a static mixer to achieve a satisfied mixing.

Mixing quality

The mixing quality of ammonia and exhaust can be assessed by the distribution of ammonia concentration in the exhaust gas. The ratio of the standard deviation to the average value is commonly used to evaluate the mixing degree of a section. Here, the ratio of the standard deviation to the average value is called coefficient of variation (CoV) which is defined in Equation (3-1). CoV can also be used to evaluate the uniformity of the velocity and temperature of exhaust. A small value of CoV means an even distribution of ammonia [72]. The mixing is assumed to be homogenous when the value of CoV is less than 5% [73].

$$CoV = \frac{1}{\bar{w}} \sqrt{\frac{\sum_{j=1}^{n} (w_j - \bar{w})^2}{n}} \qquad \textbf{(3-1)}$$

Where:

CoV : Coefficient of variation

w_j : Ammonia concentration at a sampling point

$\bar{w}$: Average of ammonia concentration

n : Number of sampling points

Previous studies evaluated static mixers mainly concerning the species uniformity. However, the velocity uniformity and pressure drop of static mixers are also needed to consider for the static mixers in SCR systems. Thus, this study aims to develop novel static mixers which can present high mixing performance and generate low pressure loss over the flow. The static mixers will be evaluated comprehensively in respect of the species uniformity, velocity uniformity and pressure drop.

3.2 Experiment on static mixers

3.2.1 Experimental objectives

Enlightened by the mixing mechanism and the form of existing static mixers, 4 novel types of static mixers are developed and tested in this study. The experiment aims at investigating the pressure loss and the mixing performance of the static mixers developed. In the laboratory experiment, nitrogen oxide (NO) is used instead of ammonia to mix with exhaust due to lacking of ammonia sensors and the similarity of NO and ammonia because that they are both gas phases. Thus NO and air are mixed by each kind of the static mixers in the experiment to simulate the mixing of ammonia and exhaust in pipelines. The mixing quality is evaluated via collecting the data of NO concentration at sampling points and the mixing performance of each static mixer is evaluated according to the calculated CoV.

3.2.2 Experimental test rig

The experimental test rig comprises the pipeline, the static mixers, the pressure loss measurement instrument, the velocity measurement equipment, the NO gas supply system, the NO concentration measurement system and the data acquisition system. Figure 3-4 shows a picture of the experiential test rig and Figure 3-5 demonstrates a sketch of the layout of the experimental equipment.

Figure 3-4 Experimental test rig for static mixers

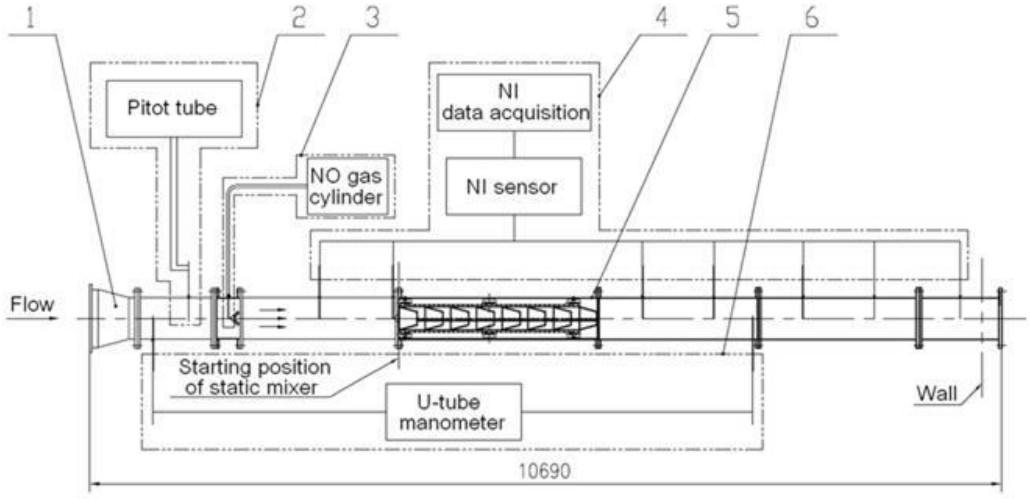

1----pipeline 2----velocity measurement equipment 3---- NO gas supply system

4---- NO concentration measurement system and data acquisition system

5----static mixers 6----pressure loss measurement instrument

Figure 3-5 Layout of experimental equipment

The air in the pipeline is supplied by an air compressor. NO is supplied by gas cylinders and introduced into the pipeline by an elbow bend pipe so that the NO discharge direction is in line with the flow. The sampling tubes and sampling points at each cross section of the pipeline are presented in Figure 3-6.

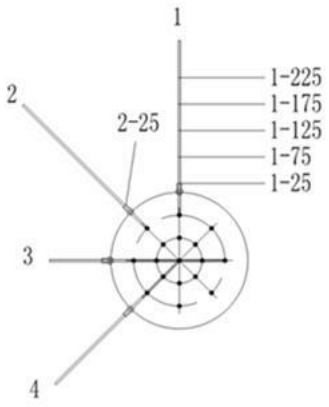

Figure 3-6 Sampling tubes and sampling points at each testing cross section

The mixture at the sampling points is sucked by vacuum pumps via 4 steel sampling tubes (No. 1-4 in Figure 3-6) that are inserted into the pipeline with depths of 10% (25 mm), 30% (75 mm), 50% (125 mm), 70% (175 mm) and 90% (225 mm) of the pipe diameter respectively. There are 7 testing sections selected in total in the experiment, among which the first 2 are located before the static mixers and the remaining 5 are after the static mixers as shown in Figure 3-7.

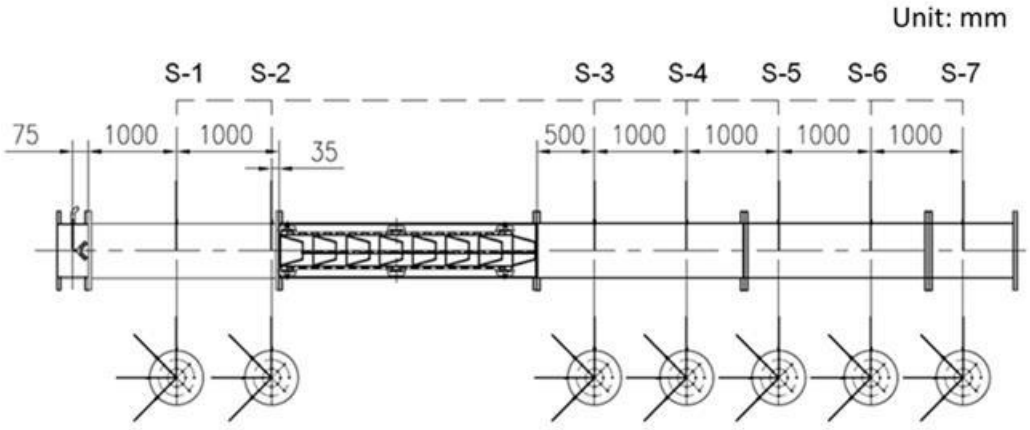

Figure 3-7 Layout of 7 testing sections along the pipeline

The concentration of NO is measured via 7 nitric oxide CiTiceL sensors (model type: 3NF/F) and recorded by an NI Multi-function data acquisition system (model type: USB-6289). The measured data are further processed using Labview software. A U-tube manometer is utilised to measure the pressure loss across the flow and the

velocity of the flow is calculated from data measured by a pitot tube. The repeatability of the sensors are listed in Table 3-1.

Table 3-1 Repeatability of sensors

Sensor	Measured varable	Repeatability
Pitot tube	Velocity	±1%
U-tube manometer	Pressure loss	±2.5%
NO sesnor	NO concentration	±2%

3.2.3 Experimental arrangement

Each static mixer is placed at the same position in the pipeline and tested individually throughout the experiment. It is unavoidable that the experiment has to be interrupted several times due to the change of static mixers; accordingly, the experimental conditions such as the flow rate of both air and NO and the temperature of the mixture cannot be maintained exactly the same each time. The flow velocity is set at 32 m/s to simulate the velocity of a diesel engine exhaust gas. The temperature of the mixture in the pipeline is 300K during the experiment. The theoretical concentration of NO based on the hypothesis of being well mixed is 150 ppm, which is calculated from the amount of NO dosed into the pipeline. A small amount of NO gas may be oxidised by air during the flow, which may introduce errors to the measurement of NO concentration. However, it has been reported in the literature [74] that the oxidation rate of NO gas is less than 4% at a temperature less than 623K. Thus, the oxidation of NO gas is ignored during the experiment.

The NO concentration distribution at the testing sections is measured with and without static mixers (denoted as the Empty pipe). The tested static mixers included 4 versions which were developed and designed under the project, i.e. Baffle mixer, Helix mixer, Torsion mixer and Box mixer. A commercially available static mixer (SV mixer) was also tested for the purpose of comparison. Figure 3-8 presents the static mixers assembled with connection pipeline. The design specifications are listed in Table 3-2.

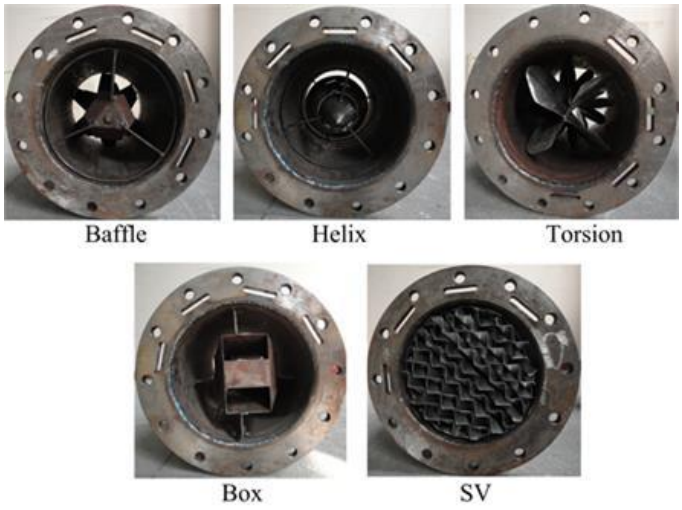

Figure 3-8 Assemblage of static mixers

Table 3-2 Design specification of static mixers

	Baffle	**Helix**	**Torsion**	**Box**	**Empty**
L_{mixer} (mm)	450	380	500	1240	250
D (mm)	250	250	250	250	250

Where:

L_{mixer} : Mixer length

D : Diameter of mixer connection pipeline

3.2.4 Experimental results

The CoV of NO concentration at each testing section and the velocity of the flow actually measured are illustrated in Figure 3-9. The experimental data are comparable because the operating conditions are the same for all the static mixers although the velocity of the flow is slightly different. The experimental results indicate that the Torsion mixer has a minimum pressure loss of 500 Pa and followed by the Box mixer of 690 Pa. Although the pressure loss of the Helix mixer is slightly higher than that of the Box mixer, the value of 950 Pa of the Helix mixer pressure loss is still acceptable for application, compared to the pressure loss of the Baffle

mixer at 2400 Pa. The SV mixer was tested with 1 and 4 mixing units installed in series respectively (denoted as SV-1, SV-4). They all show significant pressure losses of 2160 Pa and 6730 Pa individually.

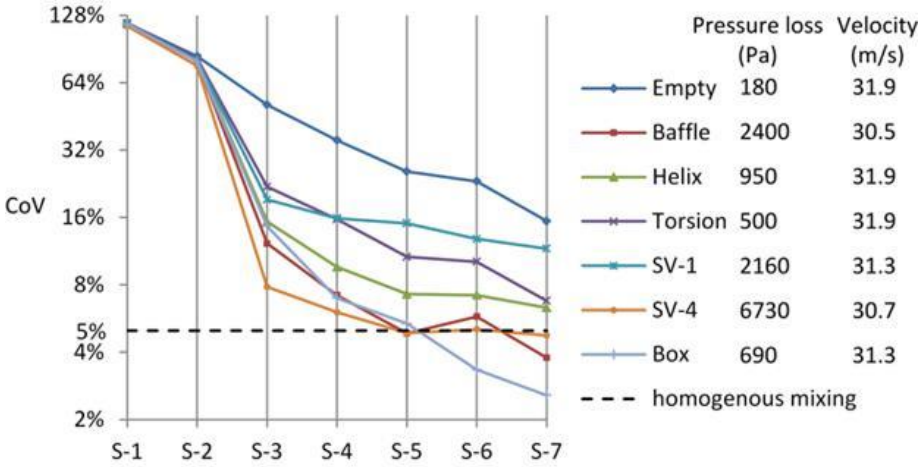

Figure 3-9 CoV of NO concentration at each testing cross section

Mixing can be carried out in a natural flow without the promotion of any mixers, but it takes a long time and the mixing quality may not be ensured within a short distance. For the reason of comparison, the mixing quality of a natural flow is measured first. The CoV of NO concentration of the Empty pipe reduces substantially from 117.6% at S-1 to 15.4% at S-7, meaning the mixing of NO and air is strengthened along the flow. However, the CoV at S-7 still does not meet the criterion for homogenous mixing because that the value of CoV at S-7 is higher than 5%.

Figure 3-9 shows that the Box mixer offers a better performance in terms of satisfying mixing homogenisation and less pressure loss generated. The CoV of NO concentration of the Box mixer at S-5 is 5.4% which almost meets the homogenous mixing criterion of 5% and it reaches the homogenous status from S-6. From the CoV changing trend of the Baffle mixer, NO possibly already distributes evenly from S-5 although the CoV at S-6 is slightly higher than 5%. That may be caused by errors in the experiment. The SV-4 mixer reaches the threshold of homogenous mixing at S-5 from where the CoV presents a gradually downward slope. However, it seems that the mixing qualities at S-7 of the SV-1 mixer, the Torsion mixer and the Helix

mixer are still substandard with their CoVs higher than 5%. The SV mixer consists of intersecting corrugated plates and channels through which the gas passes. The flow passing through small channels can be regarded as laminar flow. Hence, the turbulence of the flow inside the SV mixer channels may be hindered, which can degrade the mixing efficiency.

3.3 Simulation on static mixers

3.3.1 3D modelling of static mixers

The mixers are further simulated by commercial CFD software Fluent to compare with the experiment and provide more insightful information about the mixers. 3D models of the mixers are established by Pro/E software. In order to facilitate the meshing task for simulation, the mixers have been simplified to only retain the structures which play an important role in mixing. Simplified models of the mixers are shown in Figure 3-10.

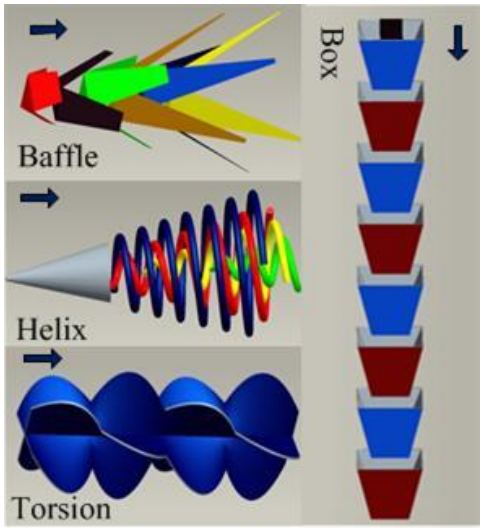

Figure 3-10 Simplified simulative model of static mixers

3.3.2 Case study

In line with the experiment, the connection pipeline for the mixers is 8.444 m long and 0.25 m in diameter in the simulation. All the mixers are simulated under the same operating conditions in order to supply a stringent environment for comparison. The inlet mass flow rate of NO is set at 0.0003 kg/s which is equivalent to 150 ppm of NO concentration used in the experiment, and the temperature of NO gas is the ambient temperature of 290K. The inlet mass flow rate of air is 1.93 kg/s with an operating temperature of 300K, which coincides with the experimental velocity and temperature. The outlet of the pipeline is set as pressure outlet boundary condition. The turbulent flow is described by a *k-ε* model. The computational domain is generally meshed with grids of size 15 mm in length in order to compromise the accuracy and the running time of the simulation. To obtain an accurate simulation result, the air inlet area and the elbow bend pipe area are meshed in a smaller size of 8 mm and 2 mm respectively in length for the grids. The simulation converged with residuals of 10^{-6} for the energy conservation equation and 10^{-3} for the momentum conservation equation, continuity equation, species conservation equation and turbulent model. A schematic diagram of the simulation is illustrated in Figure 3-11.

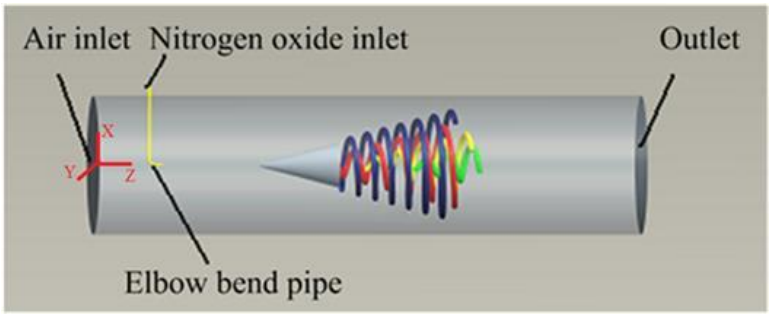

Figure 3-11 Schematic diagram of simulation

3.3.3 Evaluation of mixing quality and sampling points

The CoV presented in Equation (3-1) is used to evaluate the mixing quality of NO gas and air in the pipeline. The number of sampling points may affect the accuracy of the calculation result of CoV. Thus, two methods, the surface integral method and the sampling point method, are used in the simulation to calculate the CoV of NO

concentration at different cross sections of the pipeline. The surface integral method calculates the CoV of NO concentration at a cross section using the surface integral function of Fluent software. The precision of the result of CoV depends on the number of mesh grids of the simulation. Regarding the sampling point method, the sampling points are evenly distributed in radial directions at a cross section and the concentration of NO at each sampling points is recorded. The results of the CoV derived from the two methods are compared in order to investigate the effect of the number of sampling points on the value of CoV. The more sampling points are selected, the more accurate of the CoV can be obtained. 17 sampling points, however, are selected in the simulation to be in line with the experiment. Tecplot software is applied to acquire the concentration of NO at the sampling points concerned. The sampling points and the concentration distribution of NO at a cross section of the pipeline are illustrated in Figure 3-12.

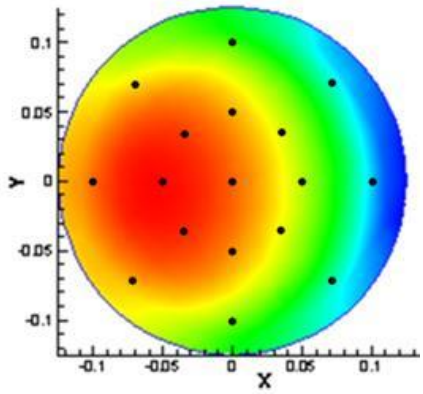

Figure 3-12 Locations of sampling points and distribution of NO concentration at a cross section of the pipeline

3.3.4 Simulation results

Contours of species, velocity and static pressure

For the purpose of clear observation of the distribution of NO concentration, flow velocity and static pressure after the mixers, Figure 3-13 to Figure 3-15 depict the contours in a range of 0-250 ppm, 0-50 m/s and -800 to 2000 Pa, respectively. Any areas where the values are beyond this range are revealed as blank.

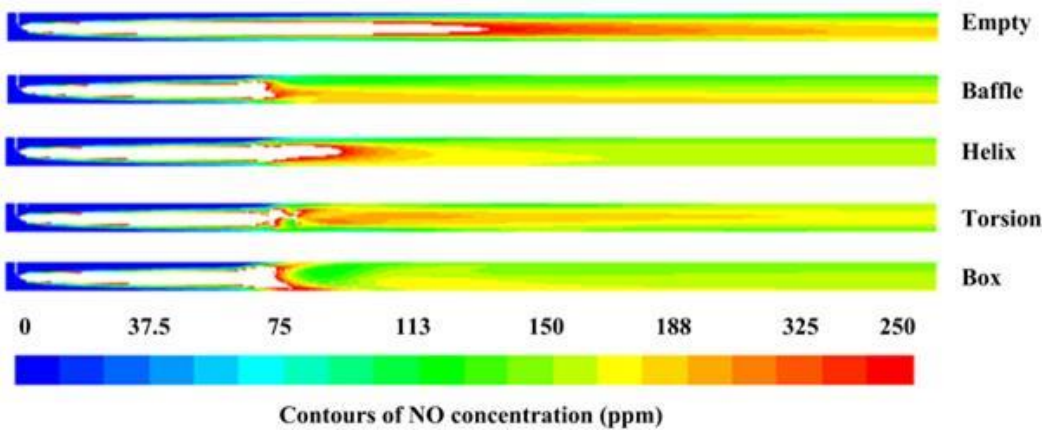

Figure 3-13 Contours of NO concentration distribution

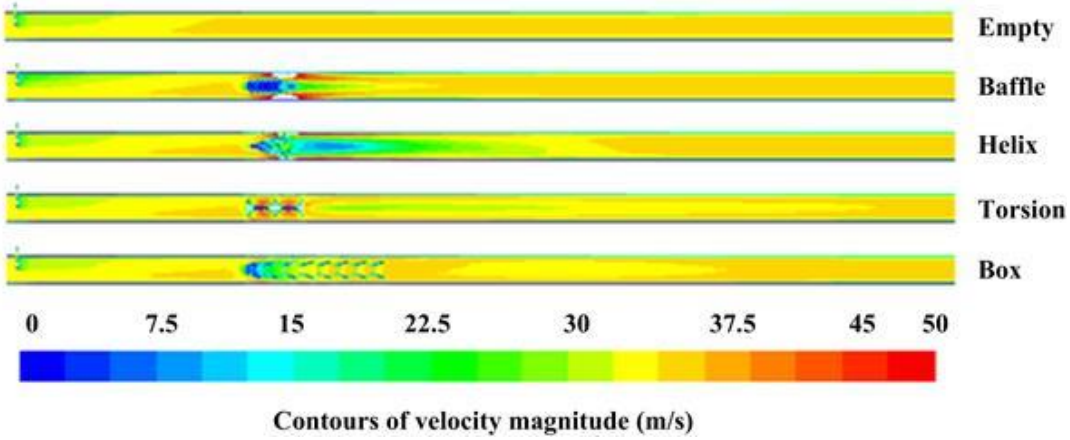

Figure 3-14 Contours of velocity distribution

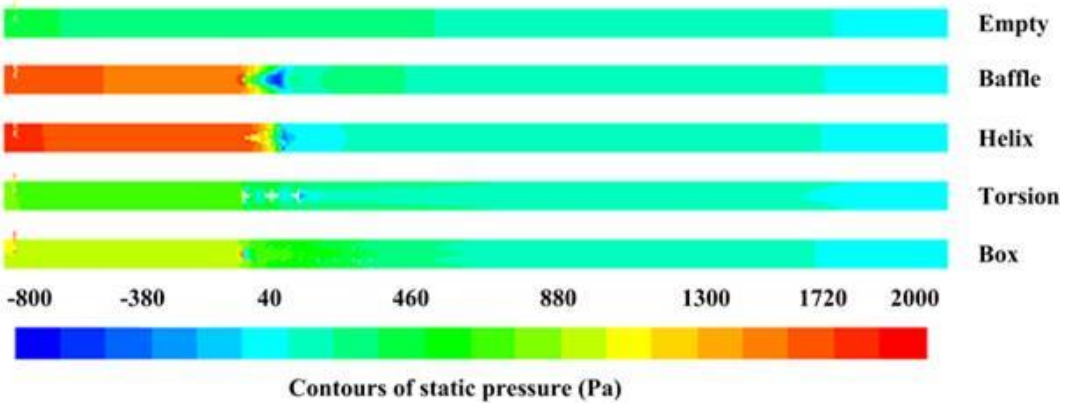

Figure 3-15 Contours of static pressure distribution

Figure 3-13 suggests that the contour of NO concentration distribution without any mixers installed in the pipeline shows an extreme uneven pattern. The homogenisation of mixing is considerably improved when mixers are installed. However, it is hard to compare the extent of improvement quantitively from the contour figures. Thus, the evaluation of mixing homogenisation by calculating the CoV of NO concentration at the cross sections is necessary. Figure 3-14 shows that the velocity of the flow is around 32 m/s when the uniform flow is established and the maximum velocity of 62 m/s where shows a blank area in the figure is observed with the Helix mixer installation. A minor flow disturbance is noticed near the elbow bend pipe where NO is introduced into the pipeline as shown in Figure 3-11. This effect nearly disappears when the flow reaches the region where the mixers are placed. However, the mixers can cause substantial disturbances of the fluid as the case of the Torsion mixer. This indicates that it may require a long distance after the Torsion mixer to achieve steady flow. Figure 3-15 presents that the pressure loss occurs mainly at the area where the mixers locate. There is a distinct pressure gradient over the mixers compared to the Empty pipe.

Average of NO concentration and its CoV at sampling sections

The average NO concentration and the CoV of NO concentration calculated from both the sampling point method and the surface integral method are presented in Figure 3-16. It shows that the values of these two parameters calculated by the two methods are different. The results from the surface integral method are more accurate towards the actual situation for the reason of sufficient sampling data obtained which are based on the mesh spacing. But it seems difficult in collecting abundant data in practice. The discrepancies of the average NO concentration and the CoV of NO concentration between the two methods can be regarded as another criterion to determine the homogenisation degree of a mixture. This is because that the mixture is becoming more and more homogenous with the mixing proceeding. The location of the sampling points is no longer important for a well-mixed flow. Another phenomenon noticed is that there are substantial differences of these two parameters between the values calculated from the two methods at S-1 and S-2. The relative

errors of the average NO concentration and the CoV of NO concentration between the values from the two methods reach up to 49% and 20% respectively before the mixers. However, they tend to become minor from S-3. The relative errors reduce considerably to less than 5% for the average NO concentration and approximate 8% for the CoV of NO concentration after the mixers. This suggests that it is feasible to use the sampling point method to obtain the average NO concentration and the CoV of NO concentration after the mixers. Hence, it proves the validity of the experimental method.

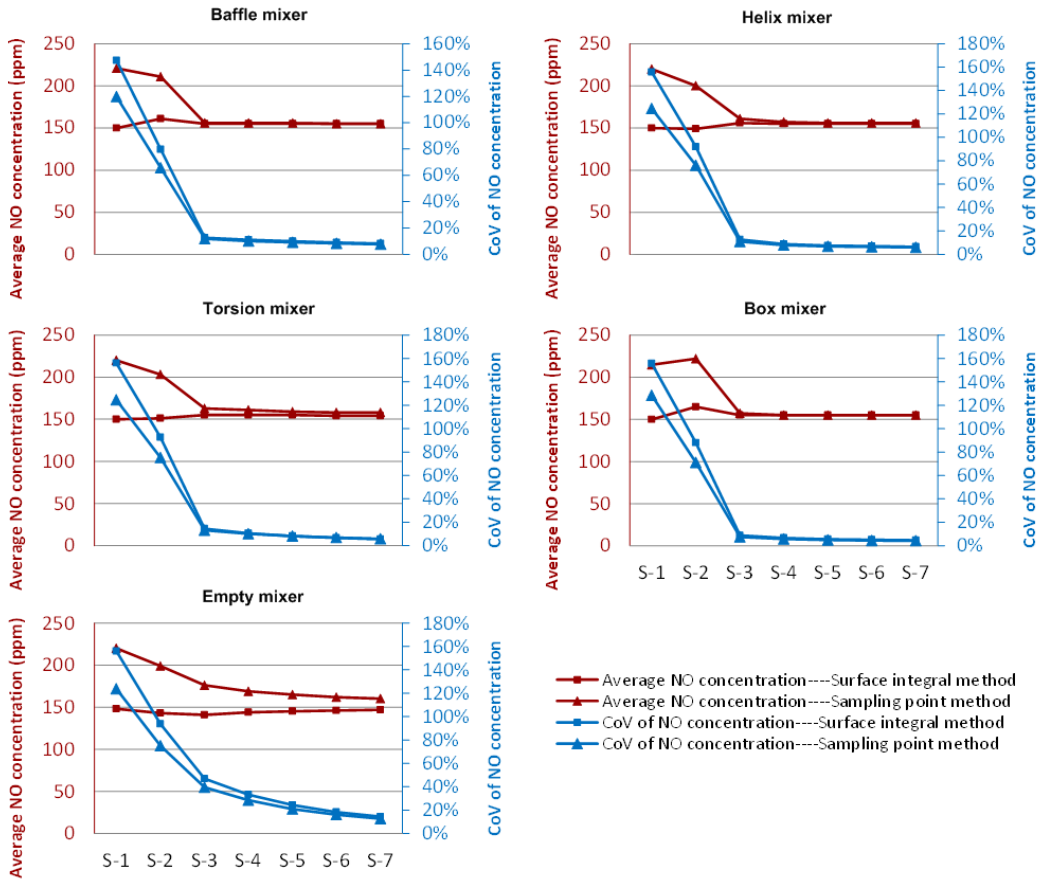

Figure 3-16 Comparison between surface integral method and sampling point method

3.4 Comparison between simulation and experiment

Figure 3-17 presents the results of pressure loss obtained from the simulation and experiment. It shows that the simulation pressure loss is generally higher than that of experiment except for the case of the Baffle mixer. The difference between the results of the simulation and experiment may be because that some unknown parameters such as roughness constant of the wall, model constants of the turbulent *k-ε* model and property parameters of the materials (like the viscosity) set in the simulation are different from the actual situation. Besides, the manufacture of the mixers may not be finished exactly the same as the models established in the simulation. Furthermore, the simulation of the mixers is conducted under an identical operating condition involving consistent velocity and temperature for easy comparison. However, operating conditions in the experiment cannot be maintained exactly the same for all the mixers. It is noticeable that the pressure loss of the Baffle mixer is opposite as the results of the other mixers. This may be caused by unexpected extra supports temporarily used during the installation of the Baffle mixer for the purpose of reducing vibration. Thus, much higher pressure loss is measured in the experiment for the Baffle mixer.

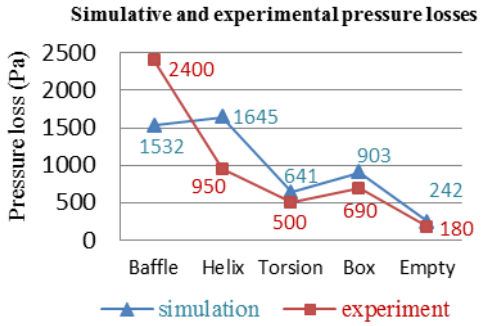

Figure 3-17 Comparison between simulative and experimental pressure losses

Figure 3-18 compares the results of the average NO concentration and the CoV of NO concentration from the simulation and experiment. The experimental data are obtained based on the sampling points on the testing sections and the values may substantially depend on the sampling points positions. Any discrepancies on the

locations of sampling points may cause immense differences on the experimental data if the stream is uneven. Although the sampling points in the simulation are selected in the same way as they are used in the experiment, the sampling points of the simulation and experiment may not coincide at the circumferential direction. This can cause the unmatchable results between the simulation and experiment. However, the results from both the simulation and experiment agree considerably along the testing sections. This suggests that the simulation predicts effectively on the mixing performance of the mixers.

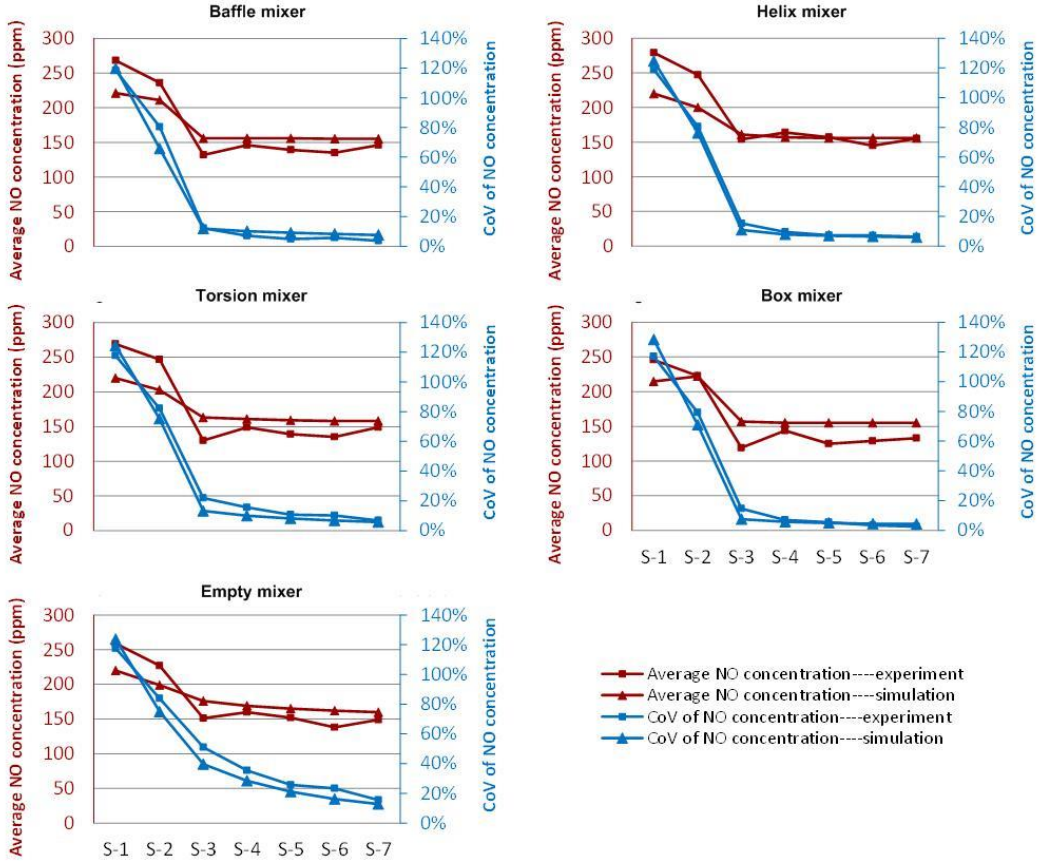

Figure 3-18 Comparison between simulation and experiment in average NO concentration and the CoV of NO concentration

3.5 Analysis on the performance of static mixers

Not only should the flow before SCR reactors be homogenous in species but also should it be even in velocity and temperature. The temperature homogenisation of the flow determines the reaction rate of SCR reactions inside each catalyst channel and thus affect NO conversion rate. Although the temperature of the exhaust gas in the nozzle area may decrease due to the spray of reductant, the cooling effect of the spray on the exhaust gas can be neglected because of the great difference on the amount of their mass flow rates. Thus, the heat transfer function of the mixers on the temperature homogenisation of the flow is out of concern. However, the velocity uniformity of the flow may still need to be considered. This is because that the velocity of the flow passing through the catalyst channels is related to the reaction residence time, which has a significant effect on NO conversion rate and ammonia slip. Based on the reasons above, the mixers are mainly evaluated by their performance on species homogenisation, velocity uniformity and pressure loss.

The performance of the mixers is analysed based on the simulation due to its flexibility in data generation. The analysed sections are selected both before and after the mixers and they are in a space interval of one diameter of the connection pipeline. The location where the mixers begin to be installed is marked as ‘0’. The position which is one diameter after each mixer is denoted as ‘1D’ and the position which is one diameter before ‘0’ is regarded as ‘-1D’. The rest symbols are marked in the same manner. The CoV of NO concentration of the Empty pipe is also analysed and compared with that of the mixers. The CoV of NO concentration at each analysed section is presented in Figure 3-19.

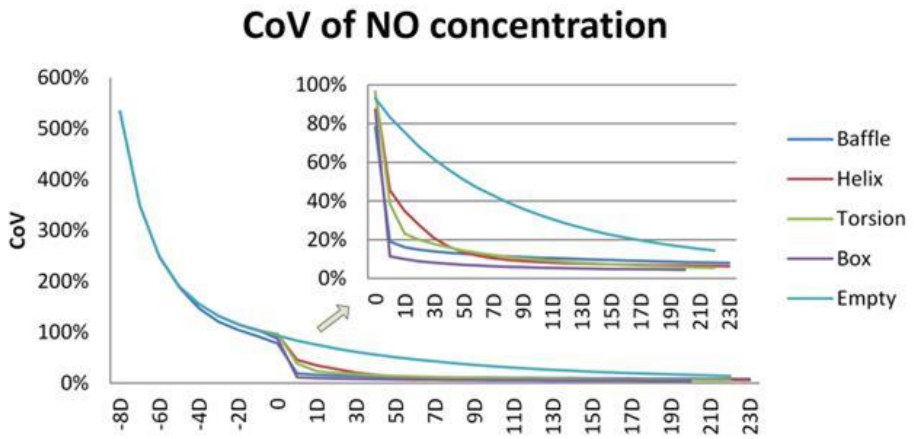

Figure 3-19 Simulative CoV of NO concentration at each analysed section

As introduced in literature [56], the CoV of NO concentration after mixers is usually associated with that before mixers. The expression is presented in Equation (3-2).

$$CoV_{mixer\_out} = CoV_{mixer\_in} \exp(-B_{mixer} \frac{L_{mixer}}{D}) \quad \textbf{(3-2)}$$

Where:

CoV_{mixer_out}: The CoV of NO concentration after mixers

CoV_{mixer_in}: The CoV of NO concentration before mixers

L_{mixer}: Mixer length

D: Diameter of mixer connection pipeline

B_{mixer}: Mixing ability coefficient of mixer

B_{mixer} is a coefficient for a given mixer and represents the mixing ability of the mixer. A high value of B_{mixer} means a high mixing efficiency of a mixer and thus is pursued. The values of B_{mixer} of the mixers are calculated based on the simulation results and listed in Table 3-3.

Table 3-3 Values of B_{mixer} of the mixers

	Baffle	**Helix**	**Torsion**	**Box**	**Empty**
L_{mixer} (mm)	450	380	500	1240	250
D (mm)	250	250	250	250	250
CoV_{mixer_in}	78.3%	95.9%	96.5%	87.2%	93.1%
CoV_{mixer_out}	19.2%	45.6%	38.5%	11.5%	83.3%
B_{mixer}	0.78	0.49	0.46	0.41	0.11

B_{mixer} of the Empty pipe shows the lowest value of 0.11. The values of B_{mixer} of the Helix mixer, the Torsion mixer and the Box mixer are close to each other ranging from 0.46 to 0.49. The Baffle mixer exhibits the highest mixing ability per unit length with 0.78 of B_{mixer}. However, the mixing process can also continue within a limited domain after mixers. This influence is called as 'mixing for free' [75][76][77] since no extra pressure loss is generated for the retained mixing effect. It utilises the turbulent flow after mixers to improve the homogenisation of mixing. Correspondingly, the changing trend of the CoV after mixers can also be expressed with an exponential equation as shown in Equation (3-3) with A and B estimated using least-squares fitting method. Figure 3-20 depicts the fit curves of CoV of NO concentration and its values at each sampling point after the mixers. The fit results are given in Table 3-2.

$$CoV = A\exp(-B\frac{L}{D}) \quad \textbf{(3-3)}$$

Where:

A, B : Coefficients to be fitted

$\frac{L}{D}$: The ratio of pipeline's length to its diameter

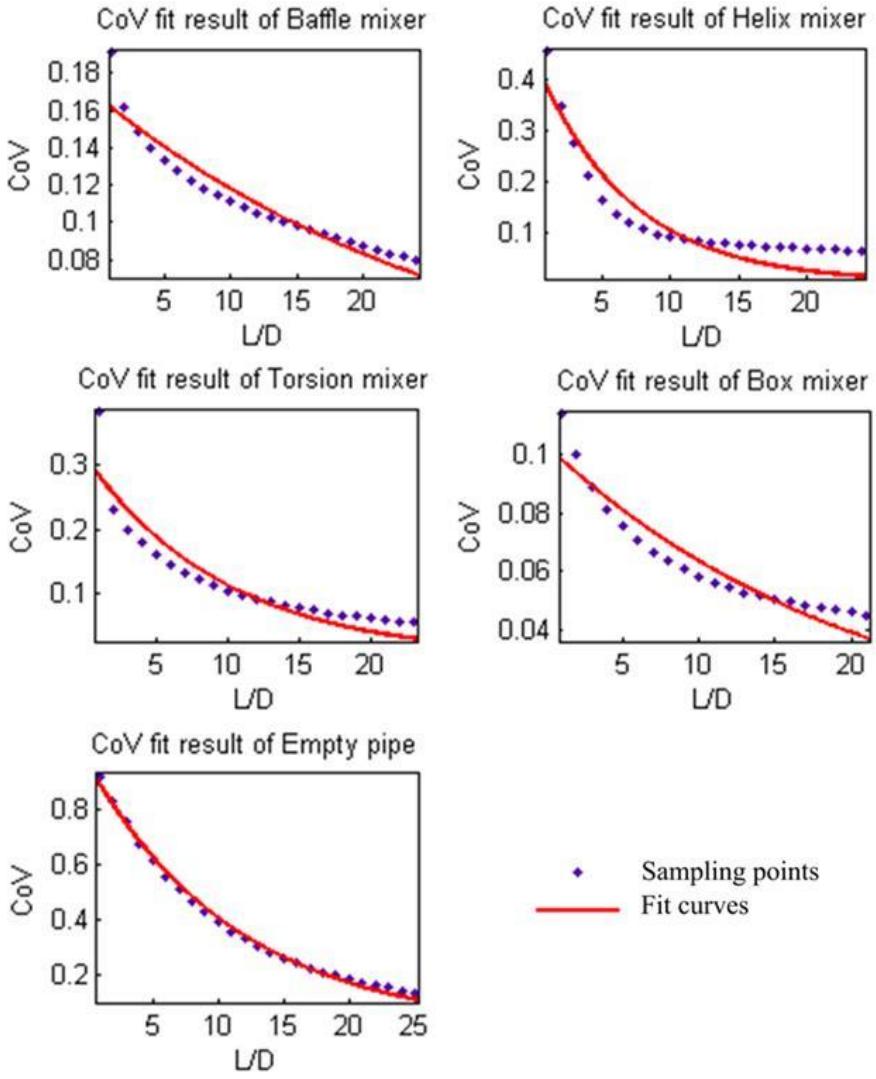

Figure 3-20 Fit curves of CoV of NO concentration after mixers

Table 3-4 Best fit results of A and B

		Baffle	Helix	Torsion	Box	Empty
Coefficients	A	0.161	0.383	0.283	0.098	0.805
	B	0.04	0.15	0.10	0.05	0.09

A indicates the CoV of NO concentration at the location where the evaluation of mixing begins and how the mixing homogenisation is there. A high value of A means an inhomogeneous mixing. B is a coefficient for a given flow. A high value of B means a high mixing ability of the mixer. Table 3-4 shows that the value of B of the Empty pipe is higher than that of the Baffle mixer and the Box mixer. This

seems inconsistent with the meaning of B standing for. However, it is necessary to consider the value of A when comparing the magnitude of B. The value of B can change substantially with the value of A even for an identical mixer [78]. A higher value of B may be obtained if the mixers locate at areas with a larger initial CoV and vice versa. Although the value of B (0.09) of the Empty pipe is higher than that (0.05) of the Box mixer, it does not mean that the 'mixing for free' ability of the Empty pipe is better than that of the Box mixer. The reason is that the maintained mixing ability of the Box mixer is evaluated beginning with a much smaller initial CoV (A=0.098), which is almost a tenth of that (A=0.805) of the Empty pipe. However, the 'mixing for free' abilities of the Baffle mixer and the Box mixer contrast reasonably due to a smaller value of B (0.04) of the Baffle mixer than that (0.05) of the Box mixer, though the Baffle mixer starting with a larger initial CoV (A=0.161) than that (A=0.098) of the Box mixer. Namely, the 'mixing for free' ability of the Box mixer is better than that of the Baffle mixer.

Figure 3-20 shows that the effectiveness of the fit curves of the Empty pipe presents the most satisfied result due to the agreement of CoV values between sampling points and fit curves. For the fit results of the mixers, the CoV of NO concentration after the mixers shows a sharp descent slope first and goes gently later. This reveals that it may be inappropriate to execute curve fit throughout the whole domain after the mixers since there may have a considerable irregular disturbance of the flow after the mixers. Hence, the value of B after the mixers is reasonably calculated within each space interval of one diameter of the connection pipeline. The gradient of B is defined in Equation (3-4).

$$k_B = B_{i+1} - B_i \qquad \textbf{(3-4)}$$

Where:

i : Index of L/D, i =1,2,3, ⋯

k_B : Gradient of B

B_{i+1}: The value of B at the position of L/D=i+1

B_i: The value of B at the position of L/D=i

The values of B based on each space interval are depicted in Figure 3-21 and the gradients of B are shown in Figure 3-22.

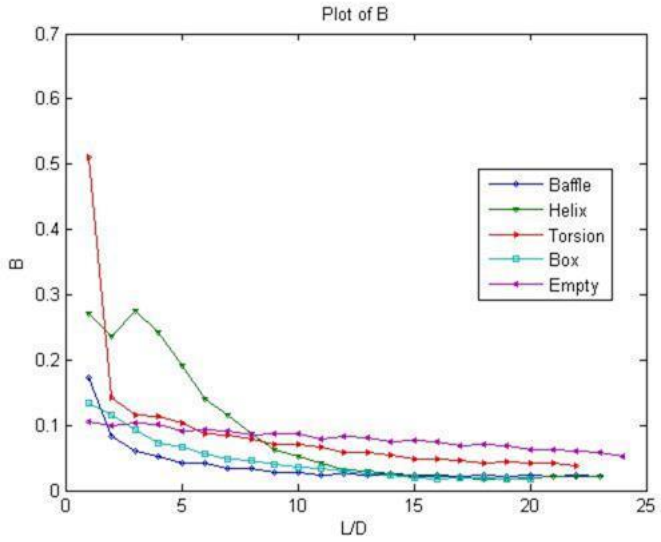

Figure 3-21 Values of B calculated based on each space interval after mixers

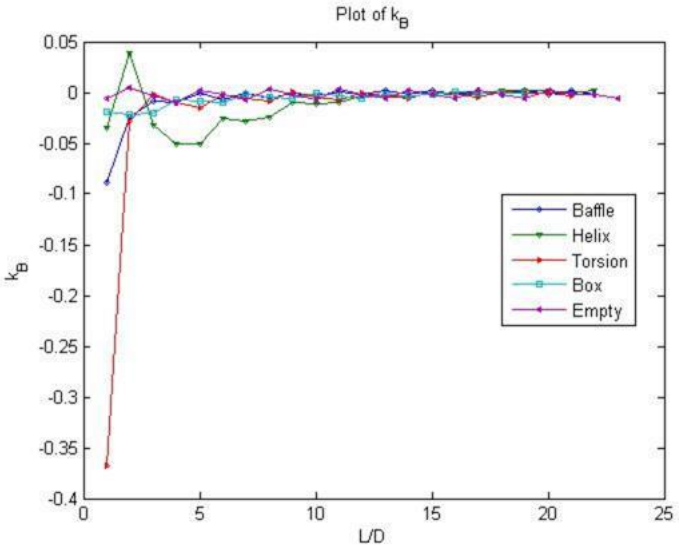

Figure 3-22 Gradients of B calculated based on each space interval after mixers

When the changing trend of the CoV exactly follows the exponential curve, the values of B calculated based on each space interval should be a constant. Figure 3-21 and Figure 3-22 show that the value of B drops sharply after the mixers for a distance. The location where shows an intense changing tendency of B can be regarded as the 'mixing for free' area. When the value of B tends to be steady (the value of k_B approaches zero), this 'mixing for free' ability is assumed to end and the following gas stream may mix naturally. This can be used to determine where to place another set of static mixers and maximally utilise the 'mixing for free'.

Apart from species homogenisation, velocity uniformity after the mixers is also considered. It is evaluated by the average vorticity and the CoV of the axial velocity at each analysed section. These variables are shown in Figure 3-23.

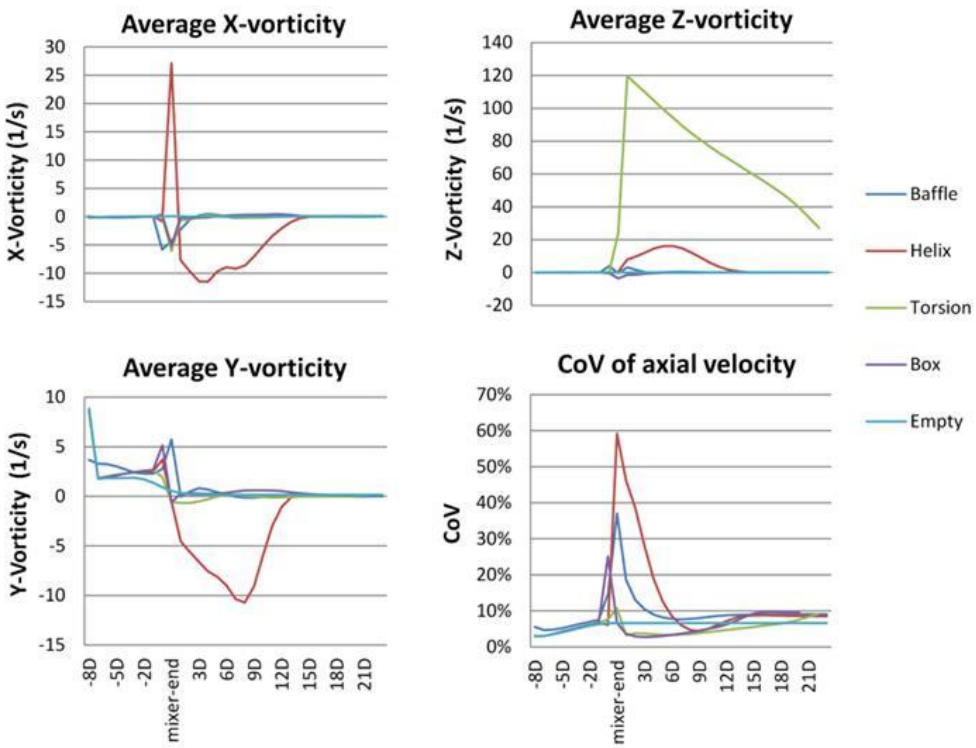

Figure 3-23 Average vorticity and CoV of axial velocity at each analysed section

The vorticity describes the spinning motion of the fluids. The average Z-vorticity suggests that the gas stream passing through the Torsion mixer swirls considerably circling the axis of the pipeline. The maximum Z-vorticity of the Torsion mixer at

the mixer-end section is 120 s^{-1}. Though the Z-vorticity decreases gradually with the flow, it still remains a value of around 30 s^{-1} by the exit of the pipeline. This is followed by the situation of the Helix mixer but the gas stream swirls with different axes, which can be seen from the average X and Y vorticities (the minus means the swirling direction). The vorticity of the Helix mixer almost reduces to 0 at the location of '12D' section. These results coincide with the flow through the Torsion mixer and the Helix mixer owing to their specific twist structures. The flow can be assumed to be uniform if the velocity CoV is less than 10%. A noticeable fact is that the Helix mixer has a substantial stretching effect on the fluids with the maximum CoV of the axial velocity of 60%. This is because that the Helix mixer is made of several spiral tubes and the deformation happens when the fluids pass across the tubes. The Baffle mixer deforms moderately on the fluids with the highest CoV of the axial velocity of 38% and the fluids thus tend to be uniform at the position of '3D' section. The Box mixer shows a low value of both the vorticity and the velocity CoV. This suggests that the fluids passing through the Box mixer can recover the original uniform flow within a short distance. Hence, the Box mixer not only mixes the fluids effectively but also ensures the velocity uniformity of the fluids.

In addition to species homogenisation and velocity uniformity, pressure loss is also an important index to evaluate the feasibility of the static mixers. As mentioned in section 3.1.3, pressure loss factor Z is usually utilised to assess the quantity of the pressure loss over the static mixers. Z factor represents how much extra pressure loss has generated due to the installation of static mixers. The values of Z factor are listed in Table 3-5 according to the simulation. It suggests that the Baffle mixer and the Helix mixer generate much higher pressure loss than that of the Torsion mixer and the Box mixer.

Table 3-5 Pressure loss factor Z of static mixers

	Baffle	**Helix**	**Torsion**	**Box**	**Empty**
Z	6.3306	6.7975	2.6488	3.7314	1

Based on the analysis above, it can be inferred that the Box mixer performs much better than the others if it makes a compromise between pressure loss and mixing homogenisation. Benefiting its irregular spacial structure, the Box mixer disturbs the gas stream by changing its flow direction. A part of flow passes through the central passage of the Box mixer where mixing takes place, while the others are guided into the outer part of the Box mixer by the plates. The flow from the central passage of the fore Box mixer unit is then divided into two parts again: the central part and the outer part. By this way, the flow is separated and merged repeatedly. The Box mixer owes the low pressure loss to its large flow area, thus it can be practically applied on SCR systems.

3.6 Chapter summary

This chapter presents a brief review of the static mixers used in SCR systems. An evaluation method of static mixers is developed in order to compare the performance of static mixers considering the species homogenisation, velocity uniformity and pressure loss of the mixers. The 'mixing for free' ability of the mixers is determined by the value of B after the mixers. When there is an intense changing tendency of B, the flow can be regarded as the 'mixing for free' area. When the value of B tends to be steady (the gradient of B approaches zero), this 'mixing for free' ability is assumed to end and the following gas stream may mix naturally.

4 noval static mixers are designed in order to promote the mixing degree of ammonia before the reactor. The performance of the mixers is further investigated by simulation and experiment. Both the results show that the Box mixer performs effectively in respect of the pressure loss and the mixing homogenization of flow. Besides, due to the simple structure, it is much easier to manufacture. Furthermore, the Box mixer is composed by several reduplicate mixing units, which makes it flexible to assemble. In conclusion, the Box mixer takes the priority to be recommended for actual applications on SCR systems.

Chapter 4.

DYNAMIC MODELLING OF AN SCR REACTOR

The interactions between various physical and chemical processes occurring within catalyst channels and on the walls of channels are complex. Experimental study on monolithic catalysts is costly and time consuming while numerical simulation provides a potential alternative for better understanding the physical and chemical phenomena inside monoliths. Mathematical modelling of monolithic catalysts is beneficial to predicting the behaviour and performance of SCR reactors in a wide range of operating conditions. Moreover, urea dosing control strategy design and geometry optimisation of reactors can be carried out based on the reactor model established. This will enormously reduce the time spent on reactor design and improve SCR conversion efficiency. As mentioned above, in order to increase the system design efficiency the development of mathematical modelling of monolithic catalysts is important.

Section 4.1 introduces the governing equations of monolithic catalyst. Section 4.2 reports a 3-state SCR reactor model and a 1-state SCR reactor model respectively. The models are further executed in section 4.3. The 3-state SCR reactor model comprises 3 differential equations of SCR reactions and a temperature equation. The unknown parameters of the 3-state SCR model are estimated and validated in section 4.4. The parameters estimated in the 3-state SCR reactor model are further utilised in the 1-state SCR model to investigate the adequacy of the 1-state SCR model, which is discussed in section 4.5.

4.1 Governing equations of monolithic catalyst

4.1.1 Introduction of monolithic catalyst

Monolithic catalyst is widely used in devices such as SCR, three-way catalytic converter, lean NO_x trap and diesel oxidation catalyst for reducing harmful emissions from internal combustion engines. Monolith can be coated with different catalysts in the form of washcoat on substrates for different purposes of use. It has the advantages of high heat and mass transport rates, small transverse temperature gradients and ease of scale-up. Monolithic structures are exceptionally durable with high anti-crush strength when used at temperatures below 800 ℃ [79]. The substrates of monolithic catalyst offer high specific surface and low pressure drop at high space velocity.

Monolithic catalyst consists of a vast number of parallel straight channels through which reacting gases usually flow in a laminar regime. The straight channels normally have circular, square or triangular cross-sections. The cell density of monolith commonly ranges from 25 to 400 channels per square inch (cpsi). It is common that a monolithic catalyst element is manufactured in a square shape with each side length of 150 mm for the purpose of easy assembly to a module. A monolithic catalyst module is shown in Figure 4-1.

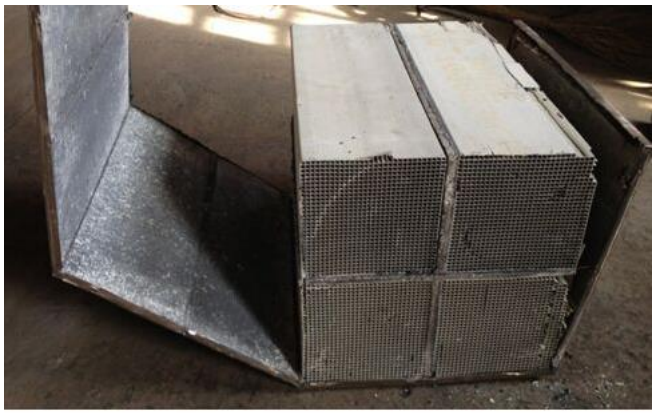

Figure 4-1 A catalyst module packed with 4 monolithic catalyst elements

There are two types of monolithic catalysts: one makes entire monolith walls of catalytic materials by an extruding method and the catalytic reactions occur on the whole monolith walls by internal diffusion. The other type of monolithic catalyst is to cover substrates with a washcoat by an impregnation method or a coating method. For this type of monolithic catalyst, only the washcoat layers (less than 0.1 mm in thickness) [80] close to the gas-solid interface is considered to be catalytically active and the reactions only occur at the washcoat surface without any internal diffusion effect. A schematic representation of the two kinds of monolithic catalysts is illustrated in Figure 4-2.

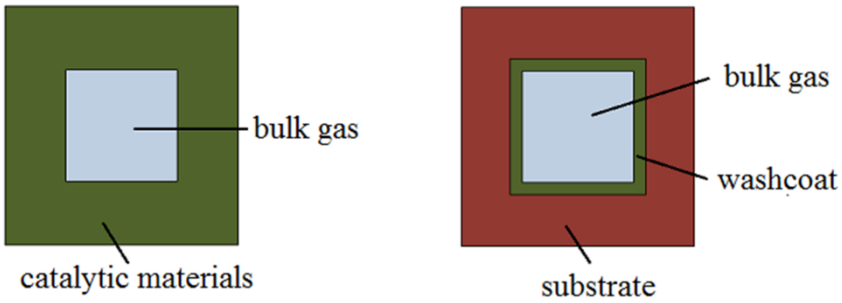

Figure 4-2 Two types of monolithic catalysts

4.1.2 Heterogeneous reaction mechanism

The chemical reactions taking place in SCR catalyst are complex and a heterogeneous reaction mechanism is commonly used to describe the phenomena in a catalyst channel. The heterogeneous reaction mechanism separates the solid catalyst from the gas reactants and products of the reactions. The steps in a heterogeneous catalytic reaction are presented in Figure 4-3 [81].

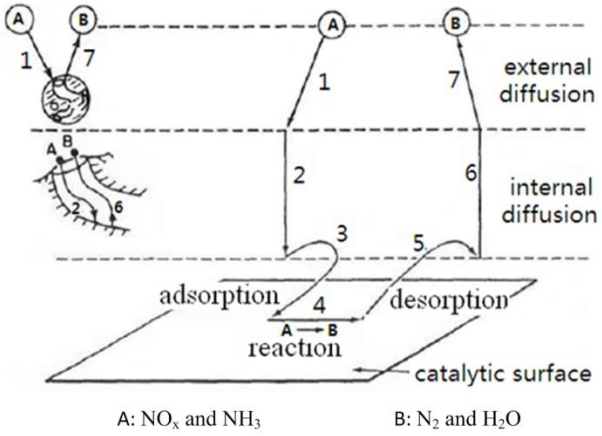

Figure 4-3 Steps in a heterogeneous catalytic reaction [81]

As shown in Figure 4-3, NO_x and NH_3 diffuse from the exhaust to the catalyst surface through external diffusion and internal diffusion as shown in steps 1 and 2. The NH_3 will further adsorb on the catalyst surface to produce intermediate species which is regarded as the adsorbed NH_3 as shown in step 3. It is reported that SCR reactions are subject to E-R mechanism [82]. The NO_x at the catalyst surface can react with the adsorbed NH_3 without adsorption. After reacting, the reaction products N_2 and H_2O diffuse in an opposite way.

4.1.3 Universal governing equation of fluid dynamics

Having understood the reaction mechanism inside catalyst channels, dynamic modelling of monolithic catalyst can be proceeded. The governing equations for the flow, heat transfer and reactions inside monolithic catalyst are developed based on the universal governing equation of fluid dynamics and a number of assumptions for the monolithic catalyst. The universal governing equation of fluid dynamics can be presented as [83]:

$$\frac{\partial(\rho\phi)}{\partial t} + \mathrm{div}(\rho\bar{u}\phi) = \mathrm{div}(\Gamma \mathrm{grad}\phi) + S \qquad \textbf{(4-1)}$$

Where:

ρ : Fluid density, kg/m^3

t : Time, s

$\vec{u}$: Fluid velocity, m/s

ϕ : Universal variables

Γ : Universal diffusion coefficient

S : Universal source term

They are transient term, convective term, diffusive term and source term in turn from the left hand of the universal governing equation in Equation (4-1). The universal governing equation has the following formulation in Cartesian coordinates:

$$\frac{\partial(\rho\phi)}{\partial t}+\frac{\partial(\rho u\phi)}{\partial x}+\frac{\partial(\rho v\phi)}{\partial y}+\frac{\partial(\rho w\phi)}{\partial z}=\frac{\partial}{\partial x}\left(\Gamma\frac{\partial\phi}{\partial x}\right)+\frac{\partial}{\partial y}\left(\Gamma\frac{\partial\phi}{\partial y}\right)+\frac{\partial}{\partial z}\left(\Gamma\frac{\partial\phi}{\partial z}\right)+S \quad \textbf{(4-2)}$$

Where:

u, v, w : Fluid velocity in x, y and z direction, m/s

The continuity equation, momentum conservation equation, energy conservation equation and species conservation equation can be derived from the universal governing equation by replacing ϕ, Γ and S with specific expressions listed in Table 4-1. In addition, the universal governing equation shown in Equation (4-2) will be further simplified with the assumptions discussed in the next section.

Table 4-1 The specific forms of ϕ, Γ and S in universal governing equation

	ϕ	Γ	S
continuity equation	1	0	S_m
x-momentum conservation equation	u	μ	$-\frac{\partial p}{\partial x}+S_u$
y- momentum conservation equation	v	μ	$-\frac{\partial p}{\partial y}+S_v$
z- momentum conservation equation	w	μ	$-\frac{\partial p}{\partial z}+S_w$
energy conservation equation	c_pT	$\frac{\lambda}{c_p}$	S_T
species conservation equation	Y_j	$D_j\rho$	S_j

Where:

Y_j : Mass fraction of species j, dimensionless

D_j : Diffusion coefficient of species j, m^2/s

λ : Heat conductivity coefficient, W/(m K)

T : Temperature, K

c_p : Specific heat capacity, J/(kg K)

μ : Dynamic viscosity, Pa s

S_m : Mass source, kg/(m^3.s)

S_u, S_v, S_w : Momentum source in x, y and z direction, Pa/s

S_j : Species mass source, kg/(m^3.s)

S_T : Heat source, J/(m^3.s)

4.1.4 Assumptions in monolithic catalyst

Mathematical modelling of monolithic catalyst can be conducted based on the universal governing equation and a number of assumptions. Although flow through monolithic catalyst is inherently three-dimensional (3D) with a different conversion

rate in each channel, 3D simulation is time consuming. Assuming the profiles of temperature and concentration are identical to all channels, the 3D model can be simplified to a two-dimensional (2D) model. When neglecting radial heat conduction, the 2D model can be further simplified to a one-dimensional (1D) model which is the most extensively applied at present for the modelling of monolithic catalyst. In contrast to a 3D model, a 1D catalyst single channel model is computationally efficient and can be used for real time simulation of monolithic catalyst. A 1D catalyst single channel model can be used to calibrate the kinetic parameters of catalyst by experiments. Then the kinetic parameters obtained from calibration can be incorporated in a fully 3D catalyst model in order to further understand the phenomena occurring inside catalyst. Figure 4-4 to Figure 4-6 demonstrate the simplification procedure of monolithic catalyst, leading to the development of a 1D catalyst single channel model.

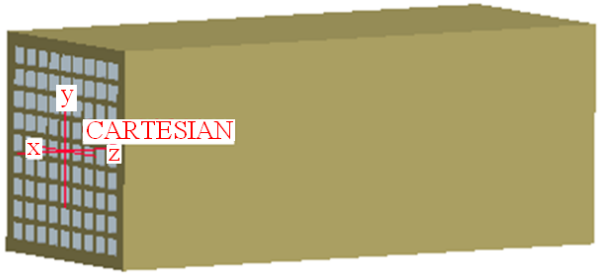

Figure 4-4 3D monolithic catalyst model represented in Cartesian coordinates

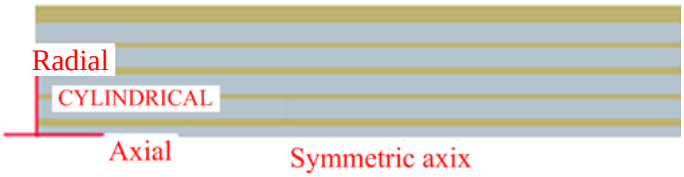

Figure 4-5 2D axi-symmetric catalyst model represented in cylindrical coordinates

Figure 4-6 1D catalyst model represented with a single channel in axial direction

In order to obtain the governing equations of the mass and heat transfer for 1D catalyst single channel model the various assumptions made by researchers [80][84][85][86][87][88][89] are used in this study. These assumptions are considered not compromising the reliability of the model. The gas in a catalyst channel is assumed to flow in *x* direction as shown in Figure 4-4. External and internal diffusion shown in Figure 4-3 is neglected for the purpose of convenient modelling. Thus, the species concentration of the bulk gas is equal to that on catalyst surface and the governing equations of monolithic catalyst are developed based on assumptions made on the flow in a catalyst channel.

The mass flow of the bulk gas is affected slightly by the adsorption and desorption reactions, suggesting that there is no source term in the continuity equation, thus S_m =0. The bulk gas in the monolith channel can be treated as incompressible fluid, so that the density of the bulk gas is regarded as a constant and thus separated from the time derivate, namely $\frac{\partial(\rho\phi)}{\partial t}=\rho\frac{\partial\phi}{\partial t}$. The bulk gas is assumed to be perfectly mixed in the radial direction. The species concentration and temperature of the bulk gas only vary in the axial direction of monolithic catalyst. This results in $\frac{\partial}{\partial y}\left(D_j\rho\frac{\partial Y_j}{\partial y}\right)$ =0, $\frac{\partial}{\partial z}\left(D_j\rho\frac{\partial Y_j}{\partial z}\right)$=0, $\frac{\partial(\rho u Y_j)}{\partial y}$ =0, $\frac{\partial(\rho u Y_j)}{\partial z}$ =0, $\frac{\partial}{\partial y}\left(\frac{\lambda}{c_p}\frac{\partial c_p T}{\partial y}\right)$=0, $\frac{\partial}{\partial z}\left(\frac{\lambda}{c_p}\frac{\partial c_p T}{\partial z}\right)$=0, $\frac{\partial(\rho u c_p T)}{\partial y}$ =0 and $\frac{\partial(\rho u c_p T)}{\partial z}$ =0. Axial mass diffusion and heat conduction of the bulk gas are neglected as they are small compared to convective terms, which means $\frac{\partial}{\partial x}\left(D_j\rho\frac{\partial Y_j}{\partial x}\right)$=0 and $\frac{\partial}{\partial x}\left(\frac{\lambda}{c_p}\frac{\partial c_p T}{\partial x}\right)$=0. Specific heat capacity c_p is assumed to be a constant to make it independent from the time derivate and space derivative. The mass fraction Y_j (dimensionless) can be replaced with molar concentration C_j (mol/m^3) for species j by using the relation of $\rho Y_j=\rho_j=M_j C_j$, and the molecular weight M_j (g/mol) of species j does not vary with time and space. Therefore, the

species conservation equation can be reformed in terms of molar concentration C_j instead of mass fraction Y_j for species j. Since the velocity and pressure changes of the flow are small, constant velocity and pressure of the flow are assumed along the channel. Thus, the continuity and momentum conservation equations are out of concern, resulting in only the energy and species conservation equations involved in the model. With these simplifications, the energy and species conservation equations for 1D single channel monolithic catalyst can be rewritten as the followings.

Simplified energy conservation equation:

$$\rho c_p \frac{\partial T}{\partial t} + \rho c_p u \frac{\partial T}{\partial x} = S_T \tag{4-3}$$

Simplified species conservation equation:

$$\frac{\partial C_j}{\partial t} + u \frac{\partial C_j}{\partial x} = \frac{S_j}{M_j} \tag{4-4}$$

4.2 Modelling of an SCR reactor

Modelling of an SCR reactor can be proceeded by discretising the simplified energy and species conservation equations obtained in section 4.1.4 into several identical cells along the flow direction [90]. Each cell is embedded with an SCR chemical kinetics model. The temperature and species concentration of a cell are considered to be uniform inside the cell. The SCR chemical kinetics model will be introduced in the following section.

4.2.1 Chemical kinetics model

The reactions occurring inside SCR catalysts are a complicated process, but it is generally reported that SCR reactions obey the E-R mechanism: the strongly

adsorbed ammonia reacts with the non-adsorbed or weakly adsorbed NO [82]. The adsorption and desorption of ammonia are given in the following reactions:

Ammonia adsorption

$$NH_3 + S = NH_3^* \quad \textbf{(4-5)}$$

Ammonia desorption

$$NH_3^* = NH_3 + S \quad \textbf{(4-6)}$$

Where:

S : Free and active catalyst site

NH_3^*: Stored NH_3 site

The V-based catalysts work effectively from 250 to 450 ℃ and show the best $DeNO_x$ performance in a temperature range of 300-400 ℃, where the standard SCR reaction is performed according to the stoichiometry:

Standard SCR reaction

$$4NH_3^* + 4NO + O_2 = 4N_2 + 6H_2O \quad \textbf{(4-7)}$$

At a low temperature (<250 ℃), the activity of the standard SCR reaction is limited. However, the NO_x conversion rate can be greatly improved by adding NO_2 to the exhaust gases due to the fast SCR reaction happened. The NO_2 concentration can be increased by installing an oxidation catalyst upstream the SCR catalyst. However, this catalytic oxidation of NO to NO_2 still requires temperatures above 170 ℃ [91].

Fast SCR reaction

$$4NH_3^* + 2NO + 2NO_2 = 4N_2 + 6H_2O \quad \textbf{(4-8)}$$

When considering a high temperature range, a slow SCR reaction is comprised in the chemical kinetics model as below:

Slow SCR reaction

$$4NH_3^* + 3NO_2 = 7/2N_2 + 6H_2O \quad \textbf{(4-9)}$$

An overconsumption of NH_3 can be observed when temperature goes above 400 ℃, at which the undesired ammonia oxidation reactions become obvious as the followings:

Ammonia oxidation

$$4NH_3^* + 3O_2 = 2N_2 + 6H_2O \quad \textbf{(4-10)}$$

$$4NH_3^* + 5O_2 = 4NO + 6H_2O \quad \textbf{(4-11)}$$

$$4NH_3^* + 4O_2 = 2N_2O + 6H_2O \quad \textbf{(4-12)}$$

The presence of SO_2 in the exhaust gases causes degradation of the catalysts by forming the deposit covering the surface of the catalysts.

$$NH_3^* + SO_2 + 1/2O_2 + H_2O = NH_4(HSO_4) \quad \textbf{(4-13)}$$

$$2NH_3^* + SO_2 + 1/2O_2 + H_2O = (NH_4)_2SO_4 \quad \textbf{(4-14)}$$

NO takes more than 90% of the NO_x in exhaust gases and NO_2 only takes a small percentage. Thus the fast SCR reaction and slow SCR reaction can be ignored. The standard SCR reaction is considered to contribute to the NO_x conversion. In order to

facilitate the development of modelling and design of model-based urea control strategies, only 4 reactions Equations (4-5) to (4-7), (4-10) (represented by subscripts of *ads, des, st, ox*) are taken into account in the kinetics model. The reaction rates of each reaction are defined according to the following chemical reaction rate laws:

Reaction rate of ammonia adsorption

$$R_{ads} = k_{ads}\left(1-\theta\right)\Omega C_{NH_3} \quad \textbf{(4-15)}$$

Reaction rate of ammonia desorption

$$R_{\mathrm{des}} = k_{\mathrm{des}}\theta\Omega \quad \textbf{(4-16)}$$

Reaction rate of standard SCR reaction

$$R_{st} = k_{st}C_{NO}\theta\Omega \quad \textbf{(4-17)}$$

Reaction rate of ammonia oxidation

$$R_{\mathrm{ox}} = k_{\mathrm{ox}}\theta\Omega \quad \textbf{(4-18)}$$

Where:

ads, des, st, ox: subscripts representing ammonia adsorption, ammonia desorption, standard SCR reaction and ammonia oxidation.

R: Reaction rate, mol/(m^3.s)

k: Reaction rate constant, s^{-1} or m^3/(mol.s)

Ω: NH_3 storage capacity of catalyst, mol/m^3

θ: NH_3 surface coverage fraction

The reaction rate constants can be obtained from Arrhenius equation as below:

$$k_i = A_i e^{-\frac{E_i}{RT}} (i = ads,\ des,\ st,\ ox) \quad \textbf{(4-19)}$$

Where:

A_i: Pre-exponential factor

E_i: Activation energy

R: Universal gas constant, *R* =8.314 J/(mol.K)

T: Catalyst temperature, K

Pre-exponential factor A_i and activation energy E_i can be obtained either by catalyst suppliers or parameter estimation. The species variables involved in the SCR chemical kinetics model are NO, NH_3 and θ that will be solved according to the simplified species conservation equation in Equation (4-4). These 3 variables are regarded as 3 states in the model as they are solved through 3 dynamic expressions which will be introduced in section 4.2.2.

4.2.2 3-state chemical dynamic equations

Upadhyay *et al* [90] developed a 3-state SCR chemical dynamic model which contains the dynamics of NO, NH_3 and θ. Equation (4-4) can be discretised into several cells along the flow direction and each cell can be performed with a 3-state SCR chemical dynamic model which is described as follow.

$$\frac{dC_{NO}}{dt} = \bar{Q} C_{NO,in} - \bar{Q} C_{NO} - k_{st} \theta \Omega C_{NO} \quad \textbf{(4-20)}$$

$$\frac{dC_{NH_3}}{dt} = \bar{Q} C_{NH_3,in} - \bar{Q} C_{NH_3} - k_{ads}(1-\theta)\Omega C_{NH_3} + k_{des}\theta\Omega \quad \textbf{(4-21)}$$

$$\frac{d\theta}{dt} = k_{ads}(1-\theta)C_{NH_3} - k_{st}\theta C_{NO} - k_{ox}\theta - k_{des}\theta \quad \textbf{(4-22)}$$

Where:

C_{NO} : NO concentration in a cell, mol/m^3

$C_{NO,in}$: NO concentration at the inlet of a cell, mol/m^3

C_{NH_3} : NH_3 concentration in a cell, mol/m^3

$C_{NH_3,in}$: NH_3 concentration at the inlet of a cell, mol/m^3

Q : Volumetric flow rate, m^3/s

V : Opening volume of catalyst, m^3

$\bar{Q}$: Normalised flow rate, s^{-1}, $\bar{Q} = \frac{Q}{V}$

4.2.3 1-state chemical dynamic equations

3-state SCR chemical dynamic model uses 3 dynamic equations which are complicated and time-consuming. It is reported by Schär [92] that 3-state SCR chemical dynamic model can be simplified into 1-state SCR chemical dynamic model which is more time-efficient. The dynamic descriptions of NO and NH_3 are represented by static elements compared to the dynamics of θ, namely $\frac{dC_{NO}}{dt} = 0$ and $\frac{dC_{NH_3}}{dt} = 0$. Thus 1-state SCR chemical dynamic model contains only θ as the state:

$$C_{NO} = \frac{\bar{Q}C_{NO,in}}{\bar{Q} + k_{st}\theta\Omega} \quad \textbf{(4-23)}$$

$$C_{NH_3} = \frac{\bar{Q}C_{NH_3,in} + k_{des}\theta\Omega}{\bar{Q} + k_{ads}(1-\theta)\Omega} \quad \textbf{(4-24)}$$

$$\frac{d\theta}{dt} = k_{ads}(1-\theta)C_{NH_3} - k_{st}\theta C_{NO} - k_{ox}\theta - k_{des}\theta$$

1-state SCR chemical dynamic model will be used for developing desired NO concentration control strategy of urea injection which will be introduced in section 5.4.2 as shown in Equation (5-16).

The equations incorporated in the 3-state and 1-state SCR chemical dynamic models have been studied in previous work [90][92]. However, the kinetic parameters of the catalyst vary on different catalyst formulae. Thus, estimating the kinetic parameters of the catalyst is the key of establishing an SCR chemical dynamic model. The estimation of the kinetic paramters for a specific SCR catalyst will be conducted this study and the SCR chemical dynamic models will be used to predict the NO_x reduction rate and NH_3 slip.

4.2.4 Temperature equation

Equation (4-3) presents the simplified energy conservation equation of the flow in monolithic catalyst. However, SCR reactions take place on catalyst surface. The reaction rate is determined by the temperature of monolithic catalyst other than that of the flow. Thus, the temperature of monolithic catalyst is solved and regarded as the temperature of a discretised cell. Assuming that there is no heat conduction between adjacent cells and reaction heat is neglected, the temperature change of a cell is associated with the heat exchange between the cell and the flow and the heat transfer between the cell surface and the ambience. To determine the heat losses of a cell, a simple heat transfer coefficient is used to describe the heat transfer between the cell surface and the ambience. The temperature equation for a cell is presented in Equation (4-25).

$$c_m \frac{M_{cat}}{n} \frac{dT}{dt} = c_p \dot{m}_g \left(T_{in} - T\right) - h_a \frac{A_{cat}}{n} (T - T_\infty) \qquad \textbf{(4-25)}$$

Where:

n : Number of discretized cell

$\dot{m}_g$: Mass flow rate of exhaust gas, kg/s

h_a : Heat transfer coefficient, W/(m^2.K)

c_m : Heat capacity of monolith, J/(kg.K)

c_p : Heat capacity of exhaust, J/(kg.K)

T_{in} : Temperature at the inlet of a cell, K

T_∞ : Ambient temperature, K

T : Temperature at the outlet of a cell which equals cell temperature, K

M_{cat} : Total mass of monolithic catalyst, kg

A_{cat} : Total area of exchange surface between monolithic catalyst and ambient, m^2

The 3-state chemical dynamic equations in conjunction with the temperature equation of a cell are regarded as the SCR reactor model. The unknown parameters of the model will be estimated in section 4.4. The SCR reactor model is beneficial to developing model based control strategies for urea injection which will be introduced in chapter 5.

4.3 Implementation of modelling

The governing equations of the SCR model have been developed in section 4.2. The unknown parameters of the model are adjusted by comparing the simulation results of model predictions with experimental results. When there is a satisfied agreement between the results of model simulation and experiment, the estimated results of the unknown parameters can be regarded acceptable. The number of discretized cells of monolithic catalyst may affect the accuracy of the SCR model. For the purpose of developing a real-time model-based control strategy for urea injection, the monolithic catalyst is considered as a whole cell.

The SCR model is implemented in MATLAB. The ordinary differential equations (ODEs) in the model take the form of Equation (4-26) and are solved by backward Euler method, which is unconditionally stable. Backward Euler method uses the backward difference approximation as the recurrence as shown in Equation (4-27).

$$\frac{dy}{dt} = f(t, y) \tag{4-26}$$

$$y_{n+1} = y_n + hf(t_{n+1}, y_{n+1}) \tag{4-27}$$

At initial condition:

$$y(t_0) = y_0 \tag{4-28}$$

Where:

y : Solution of the ODE

t : Time

f : Time derivative of the solution

y_{n+1} : Approximation of the solution to the ODE at time t_{n+1}

y_n : Approximation of the solution to the ODE at time t_n

h : Time step size

t_0 : Initial time

y_0 : Initial value of the solution to the ODE

4.3.1 Implementation of 3-state chemical dynamic equations

The 3-state chemical dynamic equations presented in section 4.2.2 are solved by backward Euler method. The iteration for NO, NH_3 and θ based on Equations (4-20) to (4-22) are derived as:

$$\begin{aligned} C_{NO,n+1} &= C_{NO,n} + hf\left(t_{n+1}, C_{NO,n+1}\right) \\ &= C_{NO,n} + h\left(\bar{Q}C_{NO,in} - \bar{Q}C_{NO,n+1} - k_{st}\theta_n \Omega C_{NO,n+1}\right) \end{aligned} \quad \textbf{(4-29)}$$

$$\Rightarrow C_{NO,n+1} = \frac{C_{NO,n} + h\bar{Q}C_{NO,in}}{1 + h\left(\bar{Q} + k_{st}\theta_n \Omega\right)} \quad \textbf{(4-30)}$$

$$\begin{aligned} C_{NH_3,n+1} &= C_{NH_3,n} + hf\left(t_{n+1}, C_{NH_3,n+1}\right) \\ &= C_{NH_3,n} + h\left(\bar{Q}C_{NH_3,in} - \bar{Q}C_{NH_3,n+1} - k_{ads}(1-\theta_n)\Omega C_{NH_3,n+1} + k_{des}\theta_n \Omega\right) \end{aligned} \quad \textbf{(4-31)}$$

$$\Rightarrow C_{NH_3,n+1} = \frac{C_{NH_3,n} + h\left(\bar{Q}C_{NH_3,in} + k_{des}\theta_n \Omega\right)}{1 + h\left[\bar{Q} + k_{ads}(1-\theta_n)\Omega\right]} \quad \textbf{(4-32)}$$

$$\begin{aligned} \theta_{n+1} &= \theta_n + hf\left(t_{n+1}, \theta_{n+1}\right) \\ &= \theta_n + h\left[k_{ads}(1-\theta_{n+1})C_{NH_3,n} - k_{st}\theta_{n+1}C_{NO,n} - k_{ox}\theta_{n+1} - k_{des}\theta_{n+1}\right] \end{aligned} \quad \textbf{(4-33)}$$

$$\Rightarrow \theta_{n+1} = \frac{\theta_n + hk_{ads}C_{NH_3,n}}{1 + h\left(k_{ads}C_{NH_3,n} + k_{st}C_{NO,n} + k_{ox} + k_{des}\right)} \quad \textbf{(4-34)}$$

Where:

$C_{NO,n+1}$, $C_{NH_3,n+1}$, θ_{n+1}: NO concentration, NH_3 concentration and θ at time t_{n+1}

$C_{NO,n}$, $C_{NH_3,n}$, θ_n: NO concentration, NH_3 concentration and θ at time t_n

$C_{NO,in}$, $C_{NH_3,in}$: NO concentration and NH_3 concentration at the inlet of a cell

4.3.2 Implementation of 1-state chemical dynamic equations

The iteration for θ in 1-state SCR chemical dynamic model is the same as it shows in Equation (4-34). The iteration for NO and NH_3 are derived based on Equations (4-23) and (4-24) and are presented as the followings:

$$C_{NO,n+1} = \frac{\bar{Q}C_{NO,in}}{\bar{Q} + k_{st}\theta_{n+1}\Omega} \tag{4-35}$$

$$C_{NH_3,n+1} = \frac{\bar{Q}C_{NH_3,in} + k_{des}\theta_{n+1}\Omega}{\bar{Q} + k_{ads}\left(1-\theta_{n+1}\right)\Omega} \tag{4-36}$$

4.3.3 Implementation of temperature equation

Applying backward Euler approximation to Equation (4-25), the recurrence of temperature can be derived as:

$$\begin{aligned} T_{n+1} &= T_n + hf\left(t_{n+1}, T_{n+1}\right) \\ &= T_n + h\left[\frac{c_p\dot{m}_g\left(T_{in} - T_{n+1}\right) - h_a\frac{A_{cat}}{n}\left(T_{n+1} - T_\infty\right)}{c_m\frac{M_{cat}}{n}}\right] \end{aligned} \tag{4-37}$$

$$\Rightarrow T_{n+1} = \frac{c_m\frac{M_{cat}}{n}T_n + h(c_p\dot{m}_g T_{in} + h_a\frac{A_{cat}}{n}T_\infty)}{c_m\frac{M_{cat}}{n} + h(c_p\dot{m}_g + h_a\frac{A_{cat}}{n})} \tag{4-38}$$

Where:

T_{n+1}: Temperature of a cell at time t_{n+1}

T_n: Temperature of a cell at time t_n

T_{in}: Temperature at the inlet of a cell

The temperature equation can be solved independently from the chemical dynamic equations. However, solving the chemical dynamic equations needs coupling with the temperature equation as the temperature of a cell determines the reaction rate of SCR reactions. The heat transfer coefficient h_a in the temperature equation will be estimated first followed by the estimation of the pre-exponential factors A_i and activation energies E_i in the 3-state chemical dynamic equations. The estimation results will be further used in the 1-state chemical dynamic equations to validate the adequacy of 1-state SCR model which will be introduced in section 4.5.

4.3.4 Boundary and initial conditions

The monolithic catalyst is considered as a whole cell. $T_{in}(t)$, $C_{NO,in}(t)$ and $C_{NH_3,in}(t)$ are set as their values given at the inlet of the catalyst. $\theta(0)$, $C_{NO}(0)$ and $C_{NH_3}(0)$ are set as 0 to simulate that SCR catalyst works from an unloaded status. The initial $T(0)$ is set as the ambient temperature of 23 ℃.

4.4 Parameter estimation and model validation

The temperature equation shown in Equation (4-38) is independent from the chemical dynamic equations shown in Equations (4-30), (4-32) and (4-34), thus they can be implemented individually. During the simulation, the heat transfer coefficient h_a is estimated first, followed by the estimation of the pre-exponential factors A_i and activation energies E_i for the 3-state chemical dynamic equations of a cell.

4.4.1 Introduction of parameter estimation

The estimation of the unknown parameters in a model is regarded as an optimisation process. It aims to find the optimal values of the unknown parameters in the model to

make the model much closer to the actual system. This is performed by minimising the sum of the squared residuals between the model calculated values and the measured values of both the temperature and the species concentration after the SCR reactor. The estimation process is conducted by using the least-squares fitting method and realised by the function *lsqurvefit* in the Matlab Optimisation toolbox. Figure 4-7 shows a sketch of parameter estimation process.

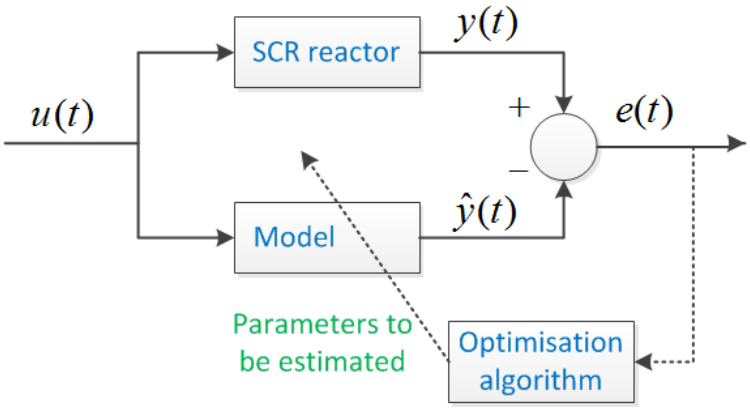

Figure 4-7 Parameter estimation process

The objective function of the temperature equation is defined as to find the heat transfer coefficient h_a that best fit Equation (4-39):

$$J = min\sum_{i}\left(T_{i,s} - T_{i,t}\right)^2 \qquad \textbf{(4-39)}$$

Where:

i: The number of the sample

$T_{i,s}$: Simulated temperature of exhaust gas after the catalyst

$T_{i,t}$: Tested temperature of exhaust gas after the catalyst

$T_{i,s}$ is obtained through Equation (4-38) by simulation and $T_{i,t}$ is obtained by experiment.

The objective function of chemical dynamic equations is defined as to find the NH_3 storage capacity of the catalyst Ω, pre-exponential factors A_i and activation energies E_i that best fit Equation (4-40). Since NH_3 slip is usually controlled under 10 ppm, it is much smaller than the value of NO concentration after the catalyst. In order to better fit NH_3 slip, there needs a weighted factor to scale the proportion of NH_3 slip in the optimisation objective function of Equation (4-40). During the estimation process, the weighted factor is determined as 100 in the simulation to obtain a satisfied fit result of NH_3 slip.

$$J = min\sum_{i}\left[\left(C_{NO,i,s} - C_{NO,i,t}\right)^2 + weighted\ factor \cdot \left(C_{NH_3,i,s} - C_{NH_3,i,t}\right)^2\right] \quad \textbf{(4-40)}$$

Where:

$C_{NO,i,s}$, $C_{NH_3,i,s}$: Simulated concentrations of NO and NH_3 after the catalyst

$C_{NO,i,t}$, $C_{NH_3,i,t}$: Tested concentrations of NO and NH_3 after the catalyst

$C_{NO,i,s}$ and $C_{NH_3,i,s}$ are obtained through Equations (4-30) and (4-32) by simulation for the 3-state SCR model and through Equations (4-35) and (4-36) for the 1-state SCR model. $C_{NO,i,t}$ and $C_{NH_3,i,t}$ are obtained by experiment.

4.4.2 Experiment for parameter estimation

As there are unknown parameters in the SCR model, it needs experimental data of the temperature and the concentrations of NO and NH_3 both before and after the SCR reactor to estimate the values of the unknown parameters. The experiment designed for parameter estimation is conducted on the SCR experimental test rig for a diesel engine of 300 kW as introduced in Appendix 1. Figure 4-8 demonstrates a sketch of the layout of the experimental test rig.

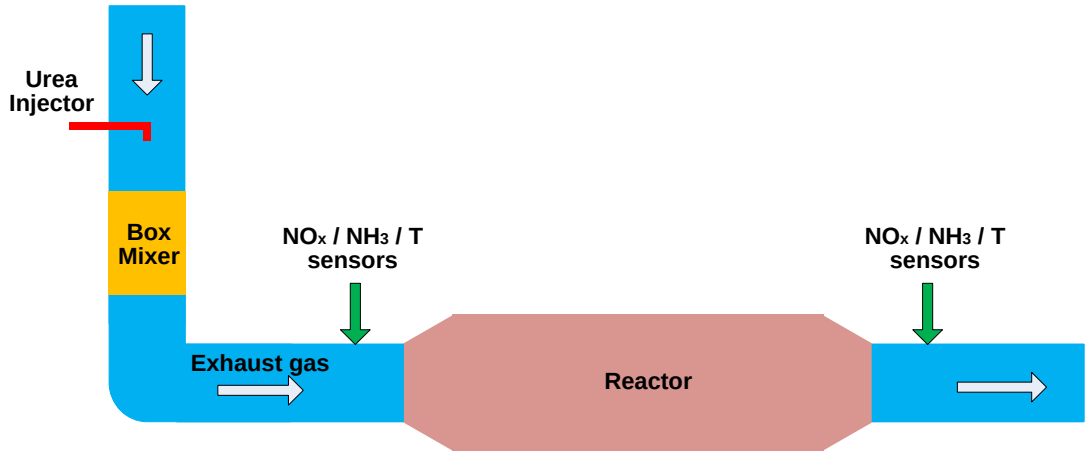

Figure 4-8 Layout of experiment for parameter estimation

During the experiment, the diesel engine operates at a propeller-law mode which should follow in E3 test cycle according to the IMO regulation. Table 4-2 shows the key test parameters for E3 test cycle.

Table 4-2 E3 test cycle for propeller-law-operated engine application

Speed	100%	91%	80%	63%
Power	100%	75%	50%	25%
Weighted factor	0.2	0.5	0.15	0.15

The experiment is conducted within 3 days, including both steady state engine operating mode and transient state engine operating mode. In order to reduce the shut off time of the catalyst at a low temperature, the engine operates at 75% load which is 225 kW at the cold start-up stage to preheat the catalyst. Once it reaches the catalyst operating temperature (> 250 ℃), the warm up process is finished. The engine operates through 25% to 100% loads, i.e. 75 kW up to 300 kW and then back to 25% load in the 1st day experiment in order to cover the whole operating temperature range of the catalyst and simulate the severe temperature increase and decrease process. When each operating point reaches steady state condition, urea injection rate is varied at different values to capture the effect of Normalised Stoichiometric Ratio (NSR) on the catalyst performance. As all the NO_x is considered in the form of NO, NSR is defined as the molar ratio of NH_3 to NO. The experiment procedure in the 2nd day is conducted in a similar way as that in the 1st

day with the operating conditions of 50% load (150 kW) and 75% load (225 kW) instead.

The experiment in the 3rd day is conducted as a transient state engine operating mode. The warm up process is the same as that in the 1st and 2nd day. When the warm up is finished, the engine operates at 50% load (150 kW) for approximate 64 minutes in order to reach a steady temperature of the catalyst. After that, the engine operating condition is changed in a sequence of 150 kW → 300 kW → 75 kW → 225 kW → 75 kW → 300 kW → 150 kW starting from the time point of 145 min for 70 minutes. Each engine operating condition lasts for 10 minutes, during which the urea is dosed at an NSR of 0.95. Followed on that, the engine operating condition maintains at 150 kW and the urea is dosed by a closed loop control strategy which sets the NO_x conversion rate of 90% as the control objective. The maximum urea dosing rate of the closed loop control strategy is limited as a value of 7000 mL/h. At the time point of 330 min, the sequence of 150 kW → 300 kW → 75 kW → 225 kW → 75 kW → 300 kW → 150 kW is repeated with the urea dosed by the closed loop strategy as introduced.

The steady state engine operating mode experiment is used for the purpose of both estimation and validation of the unknown parameters in the model whilst the transient state engine operating mode experiment is only used for model validation. The experimental operating points and corresponding NSR are presented in Table 4-3.

Table 4-3 Experimental operating points and NSR

	E3 test cycle operating points	**NSR ratio**	**Purpose**
Steady state engine operating mode	75 kW	0.8, 1.0, 1.3, 1.6, 2.0	Parameter estimation / Validation
	150 kW	0.8, 1.0, 1.3, 1.5	
	225 kW	0.8, 1.0, 1.3	
	300 kW	0.8, 1.0, 1.3	
Transient state engine operating mode	150 kW → 300 kW → 75 kW → 225 kW → 75 kW → 300 kW → 150 kW	0.95 / Closed loop control strategy	Validation

4.4.3 Initial values of parameter estimation

The parameter estimation process is conducted by the function *lsqurvefit* in the Matlab Optimisation toolbox. The function *lsqcurvefit* might only give local solutions of the estimation results and the initial point of the iteration can have a large effect on the solution. If the estimation process provides the same or worse solutions from various initial points, then the estimation results are much more likely to become the global solutions.

Although there are a number of studies focused on the research of Cu- or Fe- zeolite catalysts [93][94][95][96][97] to improve the performance of SCR systems at low temperature operating conditions, V_2O_5-WO_3/TiO_2 catalysts are still the most extensively used type of catalysts for commercial SCR systems. V_2O_5 (vanadium pentoxide) provides the main activity of the catalyst for NO_x reduction and WO_3 (tungsten trioxide) improves the thermal stability and mechanical properties of the catalyst as well as extends the temperature window of SCR reactions. TiO_2 (titanium dioxide) behaves as a carrier supporting those two active components. The kinetic parameters for V_2O_5-WO_3/TiO_2 catalyst [98][99] as well as Cu-zeolite catalyst [100] and Fe-zeolite catalyst [101][102] are used as a reference to determine the lower and upper boundaries for the unknown parameters during the estimation process. The pre-exponential factors and activation energies have been defined in Equation (4-19).

The activation energy of ammonia desorption reaction can be modified as a variable E_{des}^{*} that changes with NH_3 surface coverage fraction θ, which is presented in Equation (4-41). When the coefficient α =0, $E_{des}^{*} = E_{des}$.

$$E_{des}^{*} = E_{des}(1\text{-}\alpha\theta) \quad \textbf{(4-41)}$$

Where:

E_{des}: Activation energy of ammonia desorption reaction

E_{des}^{*}: Modified activation energy of ammonia desorption reaction

α: A coefficient

θ: NH_3 surface coverage fraction

In Lietti *et al*'s study [98], the reaction rate of standard SCR reaction is modified as:

$$R_{st} = A_{st}exp(\text{-}E_{st} / RT)C_{NO}\theta^{*}\left[1\text{-}\exp(\text{-}\theta/\theta^{*})\right]\Omega \quad \textbf{(4-42)}$$

Where:

R_{st}: Reaction rate of standard SCR reaction

A_{st}: Pre-exponential factor of standard SCR reaction

E_{st}: Activation energy of standard SCR reaction

R: Universal gas constant, *R* =8.314 J/(mol.K)

T: Catalyst temperature, K

C_{NO}: NO concentration

θ^{*}: Coefficient

Ω: NH_3 storage capacity of catalyst, mol/m^3

The kinetic parameters reported in literature are summarised in Table 4-4.

Table 4-4 Kinetic parameters of SCR catalysts given in the references

Author	**Lietti *et al* [98] and Nova *et al* [99]**	**Auvray *et al* [100]**	**Wang *et al* [101]**	**Devarakonda [102]**	**Unit**
Catalyst formula	**V_2O_5-WO_3/TiO_2**	**Cu- zeolite**	**Fe-zeolite**	**Fe-zeolite**	
Ω	270	60.9	200.9	158	mol/m^3
A_{ads}	0.614	9279	0.6	5.25×10^6	m^3/ mol.s
E_{ads}	0	0	0	47	kJ/mol
A_{des}	1.99×10^5	6.8×10^8	2×10^{10}	3.25×10^9	1/s
E_{des}	98	113	180	112	kJ/mol
α	0.448	0.39	0.7	0	----
A_{ox}	3.25×10^6	3.0×10^6	8.36×10^5	4.26×10^6	1/s
E_{ox}	120	99.5	125.3	108	kJ/mol
A_{st}	8.39×10^5	4×10^{13}	7.48×10^6	3.64×10^5	m^3/ mol.s
E_{st}	59	107.8	77	74	kJ/mol
θ^*	0.108	----	----	----	----

Where:

A_{ads}, A_{des}, A_{ox}: Pre-exponential factors of ammonia adsorption reaction, ammonia desorption reaction and ammonia oxidation reaction

E_{ads}, E_{ox}: Activation energies of ammonia adsorption reaction and ammonia oxidation reaction

By consulting the references listed in Table 4-4, the lower and upper boundary limitations for the kinetic parameters can be determined in the simulation. In this study, the reaction rate of standard SCR reaction takes the form of Equation (4-17)

and the coefficient α in Equation (4-41) is set to 0. E_{ads} is set to 0 because it is reported that ammonia adsorption occurs by a non-activated process [98][99][100][101]. Thus, it results in 9 unknown parameters to be estimated, which are h_a, Ω, A_{ads}, A_{des}, E_{des}, A_{ox}, E_{ox}, A_{st}, E_{st}.

For each unknown parameter, it is necessary to choose a large number of initial values within the boundary limitations in order to obtain the solution nearest the global optimum solution. This process can be accomplished by utilising the function *rand* in Matlab. The set number of initial values is determined by a compromise between the boundary ranges and the computational time required. For this reason, 100 sets of initial values are generated and used for parameter estimation. The simulation is repeated several times with the boundary ranges being updated according to the results obtained from previous cycle until it finds reasonable boundary ranges for each unknown parameters. In this way, the unknown parameters can be restricted to a narrow range. By comparing and searching the minimum of the squared 2-norm of the residual at each set of initial values, the estimation results of the unknown parameters are obtained.

4.4.4 Parameter estimation results

The estimation results of the unknown parameters in the 3-state SCR model are presented Table 4-5. The optimisation iteration is converged terminating with a tolerance on the changing of the objective function value less than 1×10^{-6}. By comparing the initial values and optimisation values, it can be seen that the optimisation implementation code performs effectively.

Table 4-5 Estimation results of the parameters in the 3-state SCR model

	Lower boundary	**Upper boundary**	**Initial value**	**Optimisation value**	**Unit**
h_a	0	10	2.58	3.64	W/(m^2.K).
Ω	0	280	116	68	mol/m^3
A_{ads}	0	6000	5430	361	m^3/ mol.s
E_{ads}	0	0	0	0	kJ/mol
A_{des}	1×10^5	2×10^{10}	1.73×10^{10}	5.43×10^9	1/s
E_{des}	70	180	77	111	kJ/mol
A_{ox}	2×10^3	8×10^6	6.97×10^6	1.12×10^5	1/s
E_{ox}	60	130	83	80	kJ/mol
A_{st}	2×10^7	10×10^{10}	7.34×10^{10}	5.57×10^{10}	m^3/ mol.s
E_{st}	80	120	84	117	kJ/mol

4.4.5 Model validation

The estimation results of the unknown parameters in the 3-state SCR model are validated by the experimental data as shown in Figure 4-9 to Figure 4-14. The discrepancies between the temperature and the concentrations of NO and NH_3 after the reactor from the prediction values of the 3-state SCR model and the measurement data are compared.

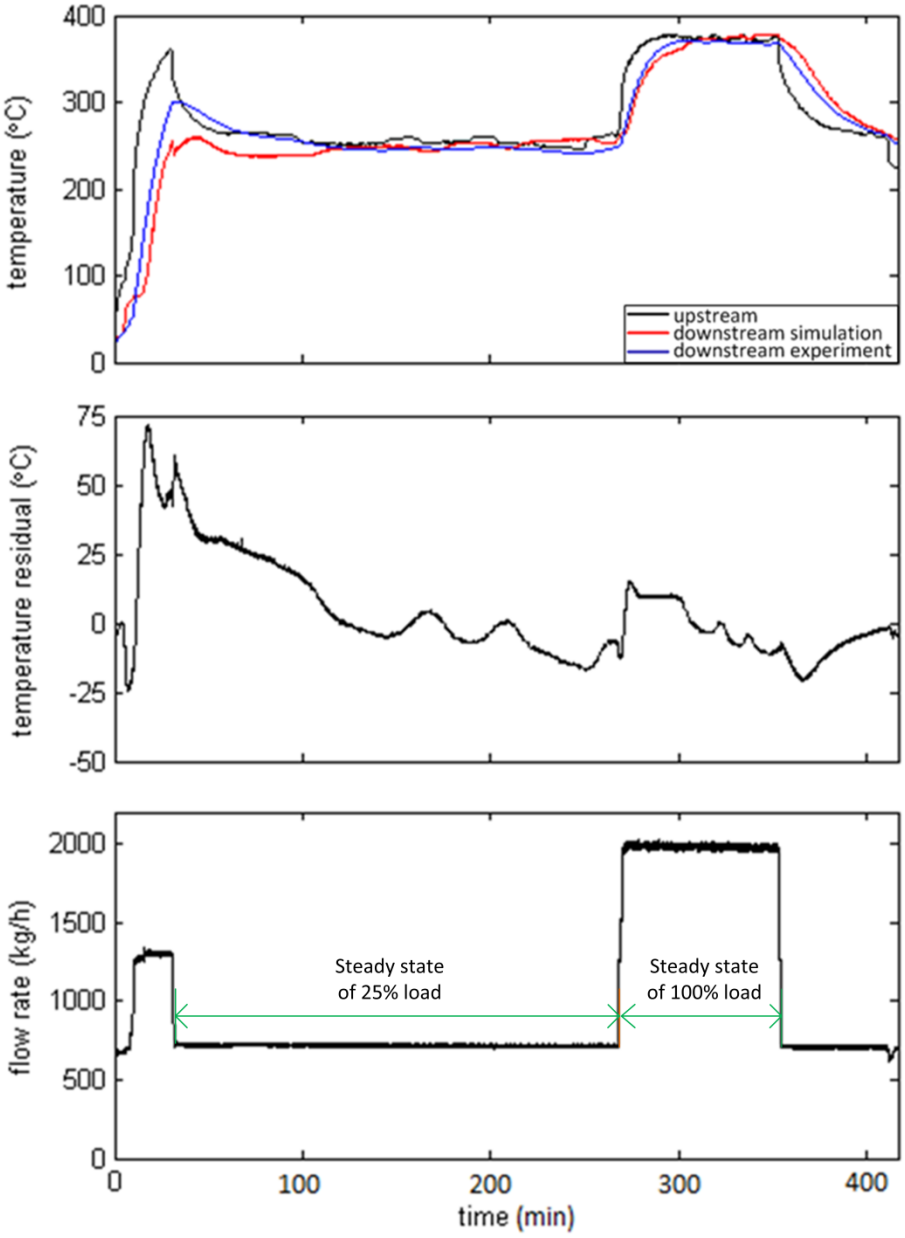

Figure 4-9 Validation of temperature under steady state engine operating points of 25% load (75 kW) and 100% load (300 kW)

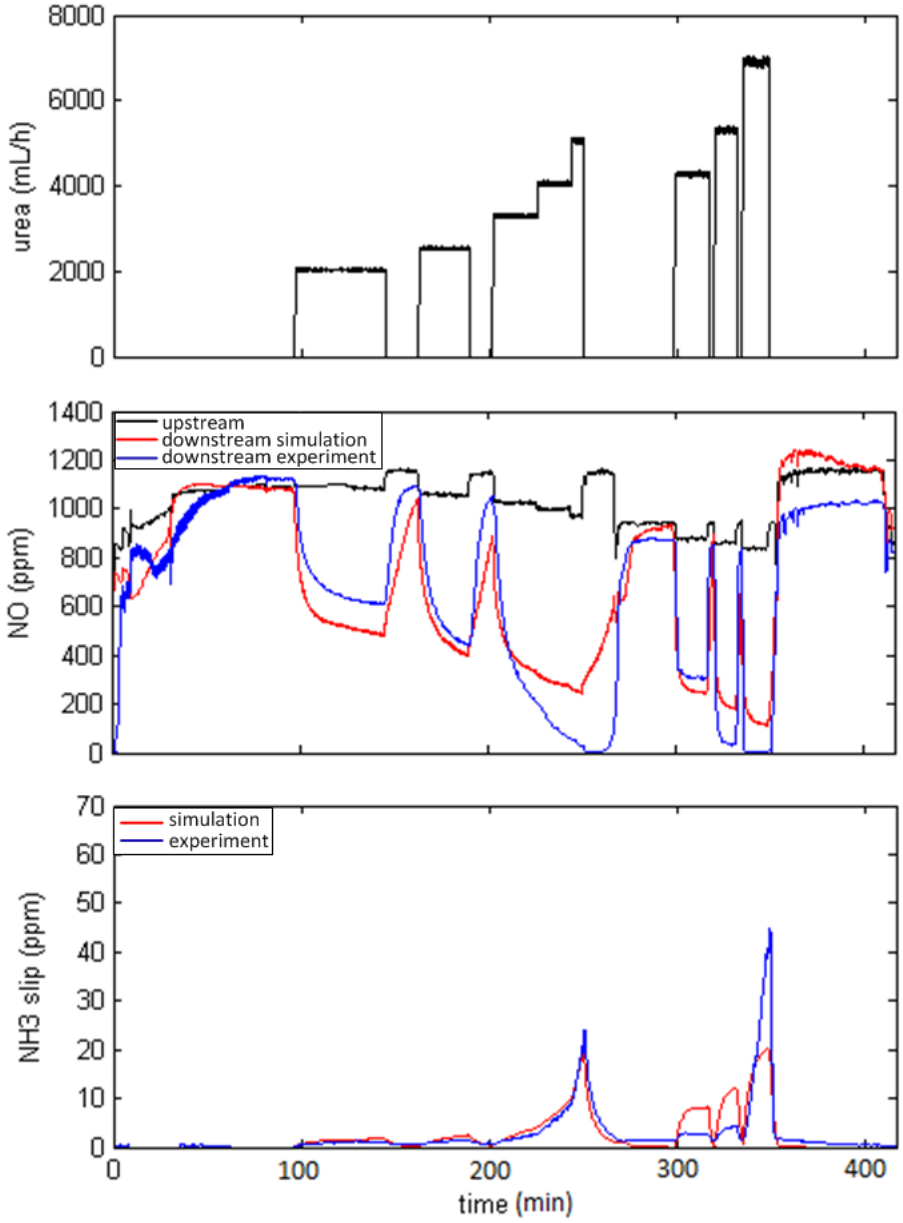

Figure 4-10 Validation of species concentration under steady state engine operating points of 25% load (75 kW) and 100% load (300 kW)

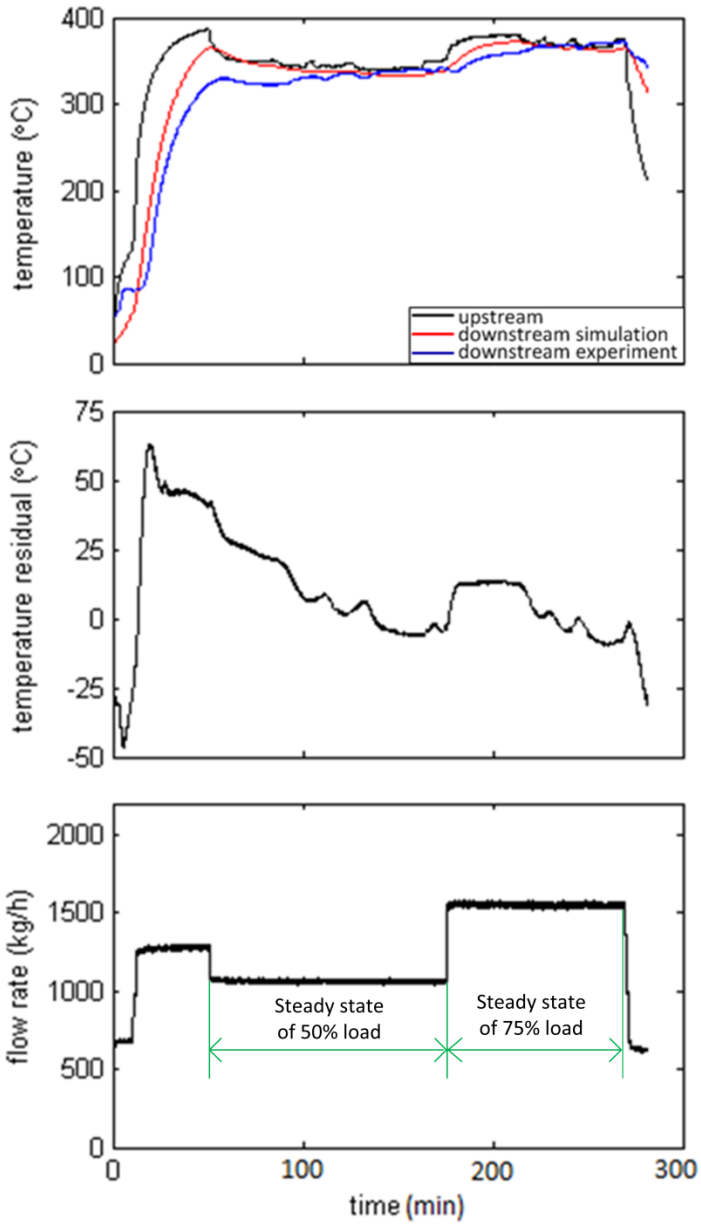

Figure 4-11 Validation of temperature under steady state engine operating points of 50% load (150 kW) and 75% load (225 kW)

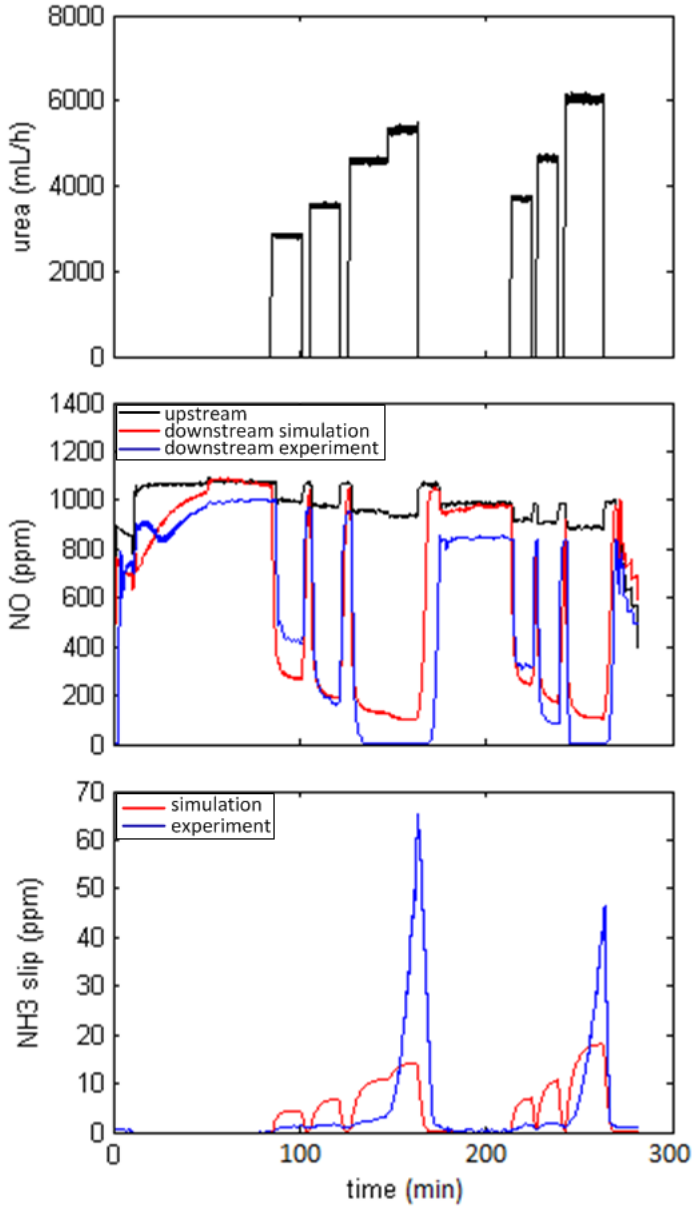

Figure 4-12 Validation of species concentration under steady state engine operating points of 50% load (150 kW) and 75% load (225 kW)

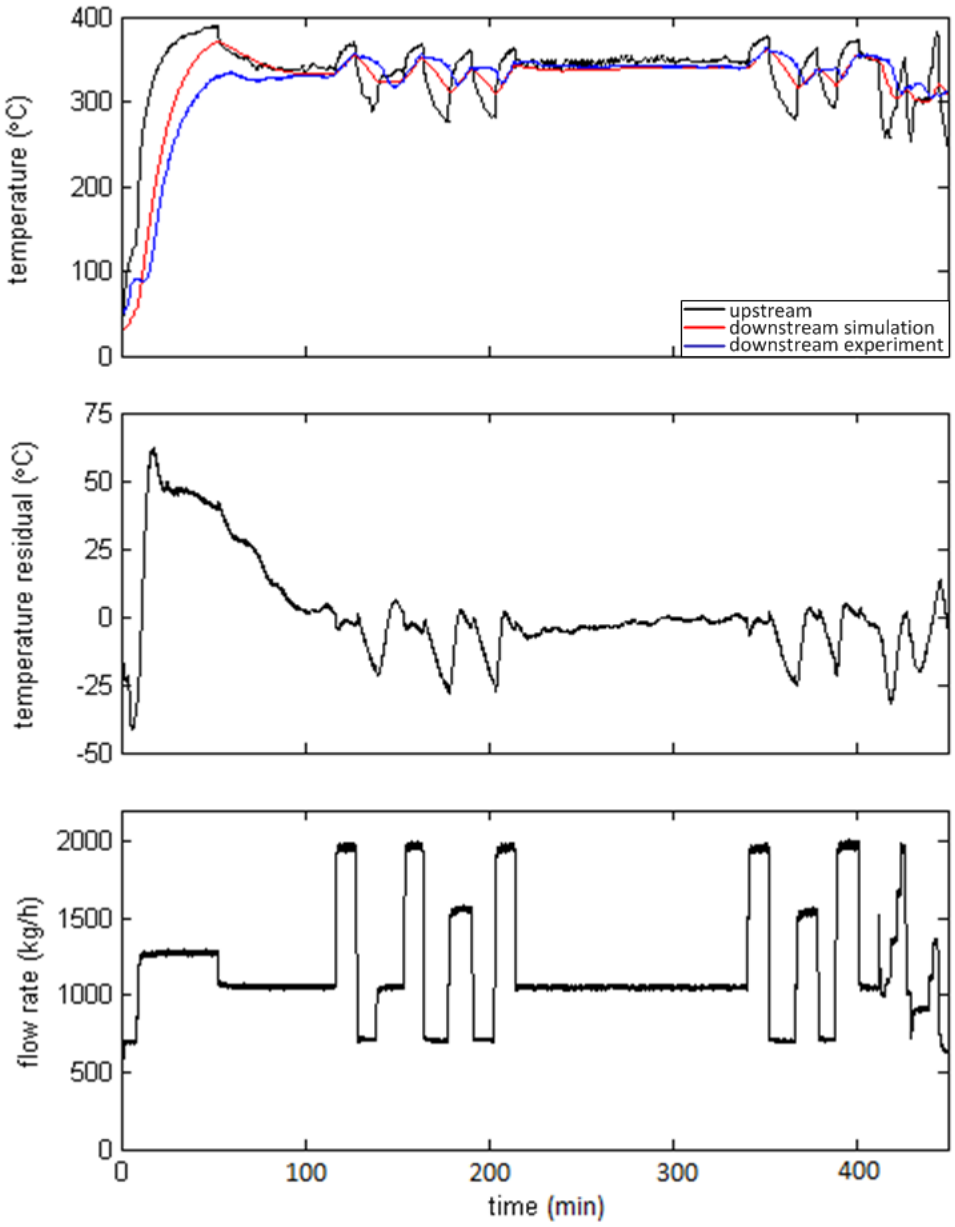

Figure 4-13 Validation of temperature under transient state engine operating condition

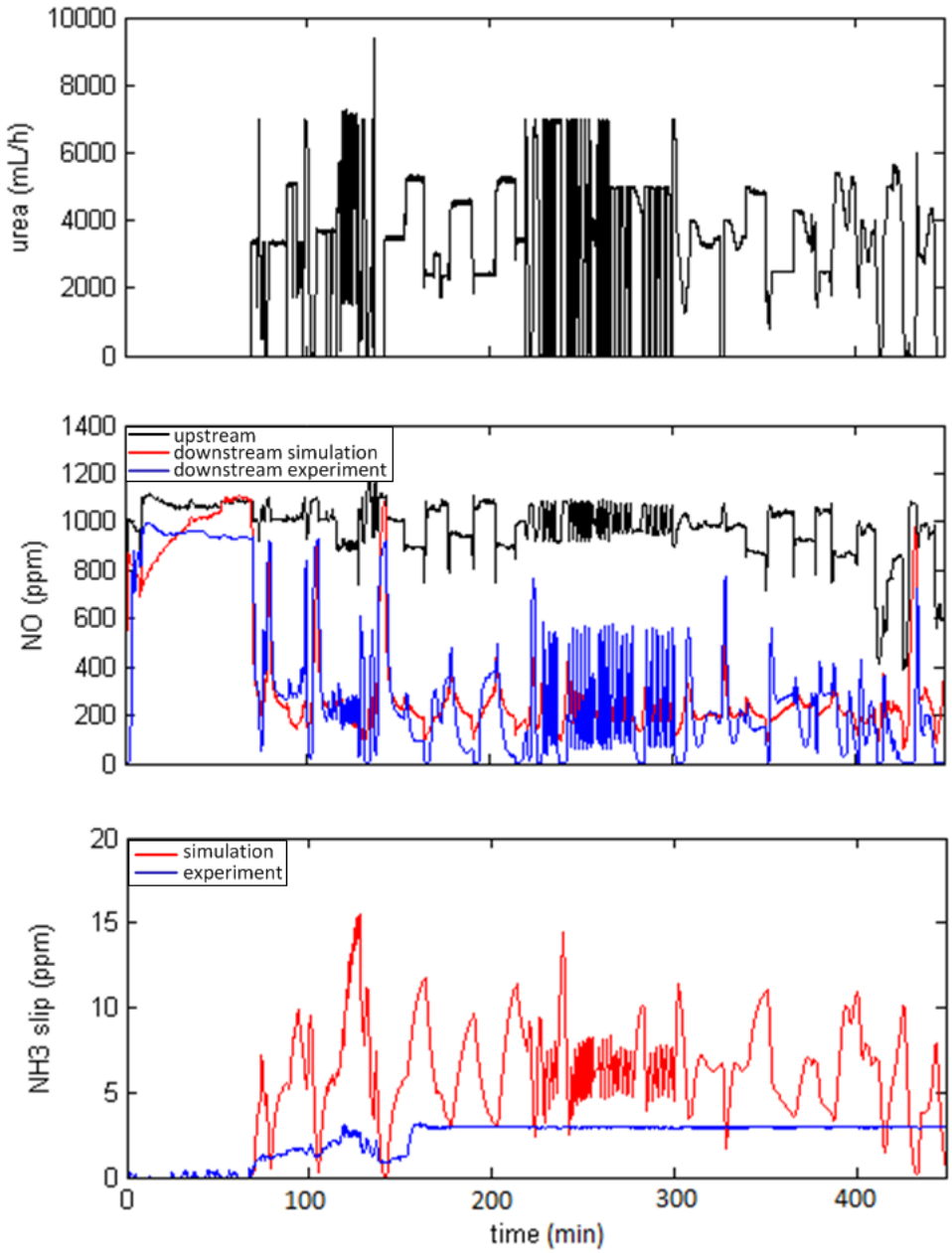

Figure 4-14 Validation of species concentration under transient state engine operating condition

Figure 4-9 and Figure 4-10 present the validation results of the temperature and the concentrations of NO and NH_3 after the reactor under steady state engine operating points of 25% load (75 kW) and 100% load (300 kW). The engine operates at 75% load (225 kW) at the cold start-up stage for approximate 30 minutes to preheat the catalyst. When the temperature downstream the reactor goes above 250 ℃, the engine operates at 25% load for approximate 230 minutes. During this period urea is dosed at an NSR of 0.8, 1.0, 1.3, 1.6 and 2.0 respectively, resulting in different NO conversion rate and NH_3 slip in Figure 4-10. The engine further operates at 100% load for 105 minutes to capture the severe temperature change of the exhaust gas in order to estimate the heat transfer coefficient h_a . The simulated and measured temperature show a satisfied agreement, which means the estimation result of h_a is acceptable. At full load, urea is dosed at an NSR of 0.8, 1.0 and 1.3 to cover the dosing range of urea injection. It can be seen in Figure 4-10 that there is a severe NH_3 slip when urea is dosed at an NSR of 1.3 due to excessive urea injected. The kinetic parameters of the catalyst are determined by compromising the fit results of the NO and NH_3 concentrations after the reactor. The deviations between the simulation and the experiment may be caused by the simplification of the reactions involved in the catalyst. However, the changing tendencies between the concentrations of NO and NH_3 from the simulation and experiment show satisfied agreements.

Figure 4-11 and Figure 4-12 present the validation results for the temperature and the concentrations of NO and NH_3 after the reactor under steady state engine operation at 50% load (150 kW) and 75% load (225 kW). The engine operates at 50% load from the time point of 60 min lasting for 120 minutes and at 75% load from the time point of 180 min lasting for 100 minutes. Figure 4-11 and Figure 4-12 show similar validation results as Figure 4-9 and Figure 4-10 but with a higher measured NH_3 slip during the experiment at the time point of 170 min. This is because that the temperature of the catalyst at 50% load is higher than that at 25% load and more NH_3 is desorbed from the catalyst at high temperature due to a high value of A_{des} obtained in Table 4-5, which results in excess NH_3 slip.

Figure 4-13 and Figure 4-14 present the validation results of the temperature and the concentrations of NO and NH_3 after the reactor under transient state engine operating conditions. The simulated and experimental temperature after the reactor shows a satisfied agreement in Figure 4-13. The deviation between the experimental measuremnts and simulation results of the NO and NH_3 concentrations under transient state engine operating condition are noticeable due to the fast changes of the flow condition as shown in Figure 4-13. The discrepancies may be caused by the simplified SCR reaction mechanism. However, the 3-state SCR reactor model can still be used to predict the behaviour of the SCR reactor and develop model-based urea control strategies which will be introduced in chapter 5.

4.5 Adequacy of 1-state chemical dynamic equations

1-state chemical dynamic equations are the simplified form of 3-state chemical dynamic equations as introduced in section 4.2.3. The estimation results of the parameters in the 3-state SCR model can be directly applied into the 1-state model in order to compare the prediction results of the two models. For the purpose of easy comparison of the difference between the predictions of the two models, the simulation relative errors for the two models are presented in Figure 4-15.

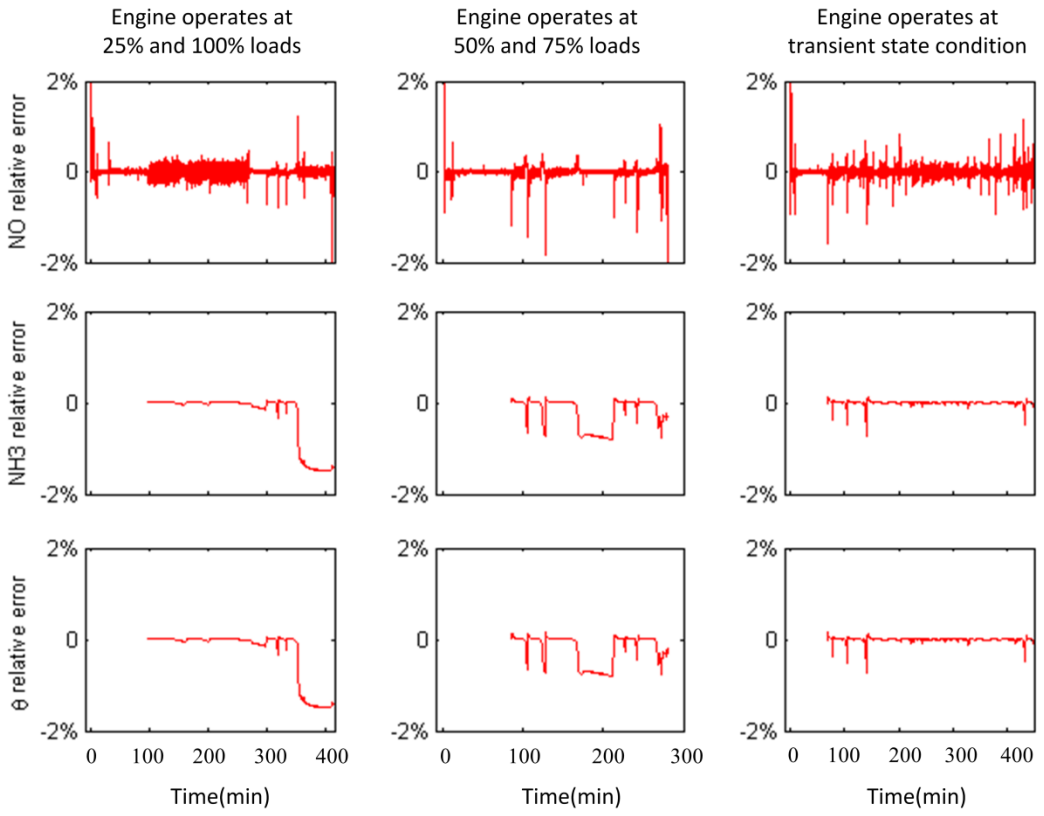

Figure 4-15 Simulation relative errors for 1-state SCR model and 3-state SCR model

Figure 4-15 shows that the simulation relative errors for the two models reside within a error band of $\pm 2\%$ except for the NO relative error at the cold start phase of the SCR reactor. This is because there is no dynamic process for the changing of NO concentration after the reactor in the 1-state SCR model as shown in Equation (4-23). Thus, the predicted value of NO concentration after the reactor of the 1-state SCR model follows instantly of that before the reactor. However, once the reactor starts working this effect is not as severe as that at the cold start phase. The relative errors of the simulated NH_3 surface coverage fraction θ and the NH_3 slip of the two models are presented from the time of approximate 100 min because there is no urea dosed at the beginning of the engine operation. The simulated NH_3 surface coverage fraction θ and the NH_3 slip of both the two models are 0. Thus, the relative errors of the simulated NH_3 surface coverage fraction and the NH_3 slip are not calculated. The relative errors suggest that the accuracy of the 1-state SCR model is adequate to

modelling of the SCR reactor. Thus, the 1-state SCR model can be used to develop model-based urea dosing control strategies which will be introduced in section 5.4.2.

4.6 Chapter summary

This chapter introduces 3-state reactor model and 1-state reactor model for the SCR reactor. The ammonia adsorption reaction, NO_x reduction reaction, ammonia desorption reaction and ammonia oxidation reaction are taken into account in the kinetics model. The unknown parameters in the model are estimated by minimising the sum of the squared residuals between the model calculated values and the measured values of both the temperature and the species concentration after the SCR reactor. The discrepancies between the model prediction and the measurement may be caused by the simplified SCR reaction mechanism. Both the models can be used to predict the behaviour and performance of the SCR reactor investigated in a wide range of operating conditions. The 3-state reactor model and 1-state reactor model will be used to develop model-based urea control strategies which will be introduced in the next chapter.

Chapter 5.

MODEL-BASED UREA CONTROL STRATEGY

The aim of urea control strategy is reducing NO_x emissions meanwhile limiting NH_3 slip to a low value. The SCR reactor model developed in chapter 4 helps to understand the working mechanism of the reactor and is used to develop model-based urea control strategies. Model-based control strategy relies on the 3-state and 1-state reactor models established in chapter 4 to accomplish urea dosing algorithm and is promising in limiting excessive NH_3 slip. Based on the 3-state SCR model, a state observer can be established to estimate the unmeasurable state like NH_3 surface coverage fraction θ. If NH_3 sensor is unavailable, NH_3 slip can also be predicted by the observer using the feedback signal from the NO_x sensor after the catalyst. Section 5.1 describes the basic rules of the developed urea dosing controller. Section 5.2 linearises the nonlinear model of the SCR reactor followed by the controllability and observability analysis of the linear model in section 5.3. Sections 5.4 and 5.5 develop sliding model control strategy and optimal control strategy respectively. Section 5.6 compares and discusses the simulation results of different control strategies.

5.1 Basic rules of the urea dosing controller

The primary aim of a controller is calculating appropriate amount of urea in order to achieve desired NO_x emissions. Beyond that, additional rules should also be involved in the algorithms of the controller. The calculated amount of urea should be limited to a reasonable range before passing the dosing signal to a dosing pump to prevent an excessive NH_3 slip. The actually injected urea is determined as:

$$u_{urea} = \begin{cases} u_{min} & u < u_{min} \\ u & u_{min} < u < u_{\max} \\ u_{max} & u > u_{max} \end{cases} \quad \textbf{(5-1)}$$

Where:

u : Calculated injection amount of urea by controller

u_{urea} : Urea amount actually injected

u_{max} : Upper limitation of urea injection amount, u_{max} =7000 mL/h

u_{min} : Lower limitation of urea injection amount, u_{min} =0

Regarding the low reduction performance of catalysts and urea deposit at a low temperature of exhaust gas, a feasible solution is shutting down urea supply when the temperature of catalyst is below a specific temperature. This specific temperature is set as 200 ℃ in the controller design.

$$u_{urea} = \begin{cases} 0 & T_{cat} < T_{min} \\ u_{urea} & T_{cat} \geq T_{min} \end{cases} \quad \textbf{(5-2)}$$

Where:

T_{cat} : Catalyst temperature

T_{min} : The minimum working temperature of catalyst

The temperature of the catalyst can be taken as the average of the measured temepratue of upstream and downstream exhaust gases:

$$T_{cat} = \frac{1}{2}\left(T_{upstream} + T_{downsteam}\right) \quad \textbf{(5-3)}$$

Where:

$T_{upstream}$: Exhaust temperature upstream SCR reactor

$T_{downsteam}$: Exhaust temperature downstream SCR reactor

A data processor is incorporated in the controller to prepare the information needed for developing urea control algorithm. The data processor calculates the space velocity of exhaust gas and converts the units of measured NO_x and NH_3 from ppm to mol/m^3. After calculating, the controller indicates the amount of urea injection in the unit of mL/h instead of mol/m^3. The performance of the urea control strategy can be evaluated by comparing NO_x reduction efficiency, average NH_3 slip and peak NH_3 slip. Due to the dynamics of the urea injection and sensors, the urea dosing control performance may be changed by control delay. However, this study aims to develop the algorithm of model-based control strategies. Thus the control delay is not considered in the design of developing model-based control strategies. These basic rules will be used in the following design of urea dosing control strategies.

5.2 Linearisation of nonlinear SCR model

According to modern control theory, the nonlinear 3-state chemical dynamic equations shown in section 4.2.2 can be linearised at an equilibrium point [103]. Linearisation of the nonlinear model leads to the following linear state space form:

$$\dot{x} = Ax + Bu + W\omega \quad \textbf{(5-4)}$$

$$y = Cx \quad \textbf{(5-5)}$$

Where:

A: System matrix

B: Input matrix

W: Disturbance matrix

C: Output matrix

x: State vector

y: Output vector

u : Input vector

ω : Disturbance vector

The input vector u is set as the equivalent NH_3 concentration $C_{NH_3,in}$ which is converted from the urea injected into the reactor. ω is set as the concentration of NO upstream the reactor $C_{NO,in}$. With the availability of NH_3 sensor in recent years [104], the output y can be set as the measured NO concentration C_{NO} or NH_3 concentration C_{NH_3} after the reactor.

The states x refer to:

$$x_1 = C_{NO},\ x_2 = \theta,\ x_3 = C_{NH_3} \tag{5-6}$$

The matrix at an equilibrium point ($C_{NO,0}$, θ_0, $C_{NH_3,0}$) is presented in Equation (5-7) [102]:

$$\begin{Bmatrix} \dot{C}_{NO} \\ \dot{\theta} \\ \dot{C}_{NH_3} \end{Bmatrix} = A \begin{Bmatrix} C_{NO} \\ \theta \\ C_{NH_3} \end{Bmatrix} + BC_{NH_3,in} + WC_{NO,in} \tag{5-7}$$

$$A = \begin{bmatrix} A_{11} & A_{12} & 0 \\ A_{21} & A_{22} & A_{23} \\ 0 & A_{32} & A_{33} \end{bmatrix}, B = \begin{bmatrix} 0 \\ 0 \\ \bar{Q} \end{bmatrix}, W = \begin{bmatrix} \bar{Q} \\ 0 \\ 0 \end{bmatrix}$$

$$A_{11} = -\left(\bar{Q} + k_{st}\theta_0\Omega\right),\ A_{12} = -k_{st}\Omega C_{NO,0},$$

$$A_{21} = -k_{st}\theta_0,\ A_{22} = -\left(k_{ads}C_{NH_3,0} + k_{st}C_{NO,0} + k_{ox} + k_{des}\right),\ A_{23} = k_{ads}\left(1-\theta_0\right)$$

$$A_{32} = k_{ads}\Omega C_{NH_3,0} + k_{des}\Omega,\ A_{33} = -\left(\bar{Q} + k_{ads}\left(1-\theta_0\right)\Omega\right)$$

When the feedback signal from the NO_x sensor after the reactor is available, the output matrix is $C=\begin{bmatrix}1 & 0 & 0\end{bmatrix}$ whereas when the feedback signal from the NH_3 sensor is available, the output matrix is $C=\begin{bmatrix}0 & 0 & 1\end{bmatrix}$.

5.3 Controllability and observability analysis

The controllability and observability properties are briefly analysed and the condition when the system becomes uncontrollable or unobservable will be introduced.

The controllability matrix is presented as follow:

$$U_C=\begin{bmatrix}B & AB & A^2B\end{bmatrix}=\begin{bmatrix}0 & 0 & A_{12}A_{23}\bar{Q}\\ 0 & A_{23}\bar{Q} & \left(A_{22}A_{23}+A_{23}A_{33}\right)\bar{Q}\\ \bar{Q} & A_{33}\bar{Q} & \left(A_{23}A_{32}+A_{33}^2\right)\bar{Q}\end{bmatrix} \quad \textbf{(5-8)}$$

The system is controllable if and only if the controllability matrix U_C has a full rank of 3. The controllability matrix U_C will lose its rank if the determinant of the controllability matrix $|U_C|$ is zero. It happens when either A_{12} =0 or A_{23} =0. Considering the physical meanings of A_{12} and A_{23}, $A_{12}\neq 0$. Thus, the only condition when the system is uncontrollable happens when $\theta=1$. $\theta=1$ means that a large amount of urea is dosed in the reactor. This is unlikely to happen in actual situations because it can cause severe NH_3 slip. However, it is important to know when the system becomes uncontrollable before the design of a control strategy.

The observability matrix for NO_x feedback control is given as follow:

$$U_O=\begin{bmatrix}C\\ CA\\ CA^2\end{bmatrix}=\begin{bmatrix}1 & 0 & 0\\ A_{11} & A_{12} & 0\\ A_{11}^2+A_{12}A_{21} & A_{12}\left(A_{11}+A_{22}\right) & A_{12}A_{23}\end{bmatrix} \quad \textbf{(5-9)}$$

The system states are observable if and only if the observability matrix U_O has a full rank of 3. Similarly, the observability matrix U_O will lose its rank if the determinant of the observability matrix $|U_O|$ is zero. It happens when either A_{12}=0 or A_{23}=0. That is the same situation as analysed above for the controllability matrix.

Observability matrix for NH_3 feedback control:

$$U_O = \begin{bmatrix} C \\ CA \\ CA^2 \end{bmatrix} = \begin{bmatrix} 0 & 0 & 1 \\ 0 & A_{32} & A_{33} \\ A_{21}A_{32} & A_{32}\left(A_{22}+A_{33}\right) & A_{23}A_{32}+A_{33}^2 \end{bmatrix} \quad \textbf{(5-10)}$$

The system states are unobservable if the observability matrix U_O loses its rank where it happens when either $A_{21}=0$ or $A_{32}=0$. Considering the physical meanings of A_{21} and A_{32}, $A_{32}\neq 0$. The only condition when the system states are unobservable happens when $\theta = 0$. That means there is no urea injected into the SCR system. Thus the situation is out of consideration.

5.4 Sliding mode control

5.4.1 Sliding mode control theory

Sliding mode control is a nonlinear control method. It has been used to develop urea dosing control strategies in SCR systems in order to limit excessive NH_3 slip during abrupt temperature rising condition [102][103]. The control law of sliding mode control is a discontinuous function of time which switches between two structures. The boundary of the two structures is called sliding surface which is described by $s = 0$. The sliding surface can be approached ($s \to 0$) by accomplishing the condition:

$$S\dot{S} < 0 \quad \textbf{(5-11)}$$

Where:

S : Sliding surface

$\dot{S}$: Time derivative of sliding surface

In order to satisfy the condition, a combination of a uniform approaching law and an exponential approaching law are chosen as $\dot{S}$:

$$\dot{S} = -Msign(S) - KS \tag{5-12}$$

Where:

M , K : Coefficients needed to be tuned in simulation , $M > 0$, $K > 0$

Chattering phenomenon is often generated during the switch of the control law. Many methods have been proposed to reduce the chattering phenomenon [105][106]. A common method is setting a boundary layer for the sliding surface. The signum function $sign(S)$ in Equation (5-12) can be replaced by a saturation function $sat(S/\phi)$. The saturation function $sat(S/\phi)$ is defined as:

$$sat(S/\phi) = \begin{cases} sign(S) & |S| \geq \phi \\ S/\phi & |S| < \phi \end{cases} \tag{5-13}$$

Where ϕ is the thickness of the boundary layer, $\phi > 0$.

The first step of developing a sliding mode control strategy is to determine the sliding surface. The objective function of the sliding mode control can be chosen as a desired NO concentration after the reactor, a desired NO conversion rate or a desired amount of NH_3 slip respectively. The following sections present the detail algorithms of each control strategy based on the different objective functions introduced. The simulation results of the control strategies will be compared in section 5.6.

5.4.2 Desired NO concentration and desired NO conversion rate control strategies

The sliding surface of the desired NO concentration control strategy is defined as the difference between the measured and desired values of NO concentration after the reactor.

$$S = e_{NO} = C_{NO} - C_{NO,des} \tag{5-14}$$

Where:

e_{NO} : The difference of the measured and desired NO concentration after the reactor

C_{NO} : Measured NO concentration after the reactor

$C_{NO,des}$: Desired NO concentration after the reactor

By approaching the sliding surface $s \to 0$, e_{NO} can be eliminated. The necessary condition is:

$$\begin{aligned} S\dot{S} < 0 \Rightarrow \dot{S} &= -M_{NO} sat(S/\phi) - K_{NO} S \\ \Rightarrow \dot{C}_{NO} &= -M_{NO} sat(S/\phi) - K_{NO} S \end{aligned} \tag{5-15}$$

Where:

M_{NO} , K_{NO} : Coefficients needed to be tuned in simulation , $M_{NO} > 0$, $K_{NO} > 0$

Section 4.5 suggests that the 1-state SCR model is adequate to modelling of the SCR reactor. Thus the control algorithm of the desired NO concentration control strategy is developed using the 1-state chemical dynamic equations.

Considering differential of Equation (4-23), it obtains:

$$\dot{C}_{NO} = -\frac{\bar{Q}C_{NO,in}k_{st}\Omega}{\left(\bar{Q}+k_{st}\theta\Omega\right)^2}\dot{\theta} \tag{5-16}$$

Combining Equation (5-16) with Equations (4-22) and (4-24), the following equation is derived:

$$\dot{C}_{NO} = -\frac{\bar{Q}C_{NO,in}k_{st}\Omega}{\left(\bar{Q}+k_{st}\theta\Omega\right)^2}\left(\frac{k_{ads}(1-\theta)\left(\bar{Q}C_{NH_3,in}+k_{des}\theta\Omega\right)}{\bar{Q}+k_{ads}(1-\theta)\Omega}-\frac{k_{st}\theta\bar{Q}C_{NO,in}}{\bar{Q}+k_{st}\theta\Omega}-k_{ox}\theta-k_{des}\theta\right) \tag{5-17}$$

Combining Equations (5-15) and (5-17), the control law of the desired NO concentration control strategy is obtained as:

$$C_{NH_3,in} = \frac{\bar{Q}+k_{ads}(1-\theta)\Omega}{k_{ads}(1-\theta)\bar{Q}}\left((M_{NO}sat(S/\phi)+K_{NO}S)\frac{\left(\bar{Q}+k_{st}\theta\Omega\right)^2}{\bar{Q}C_{NO,in}k_{st}\Omega}+\frac{k_{st}\theta\bar{Q}C_{NO,in}}{\bar{Q}+k_{st}\theta\Omega}+k_{ox}\theta+k_{des}\theta\right)-\frac{k_{des}\theta\Omega}{\bar{Q}} \tag{5-18}$$

The control law of the desired NO conversion rate can be accomplished by substituting the desired NO concentration after the reactor in Equation (5-14) with the expression of NO conversion rate:

$$C_{NO,des} = C_{NO,in}\left(1-\eta_{des}\right) \tag{5-19}$$

Where:

η_{des}: Desired NO concentration rate

The desired NO conversion rate should be taken as an appropriate value according to the NO_x reduction capability of the catalyst. This requires considerable pre-study on the NO_x reduction performance of the catalyst. A target NO_x conversion rate map with a NH_3 slip amount of 10 ppm is generated based on the simulation results of 3-

state reactor and resented in Figure 5-1. The flow rate of the map ranges from 0.2 kg/s to 0.55 kg/s and the temperature ranges from 250 ℃ to 370 ℃ according to the common operating conditions of the SCR reactor. When the operating conditions are outside the map boundaries, the values at the map boundaries are used.

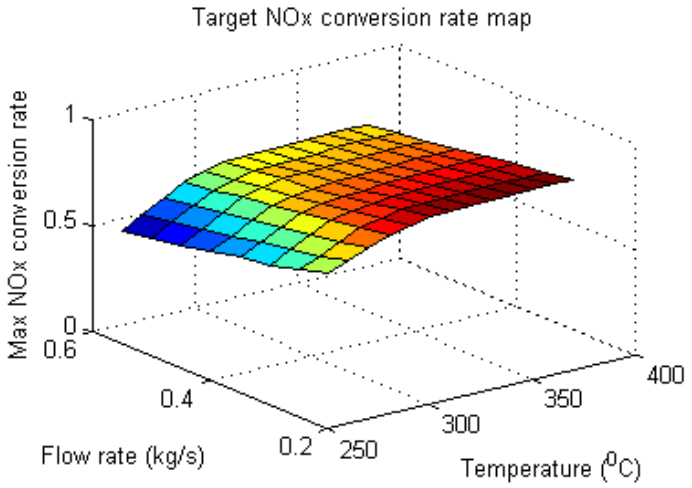

Figure 5-1 Target NO_x conversion rate map

Figure 5-1 shows that within the operating conditions, increasing the temperature and decreasing the flow rate of the exhaust can obtain a high value of NO_x conversion rate. The maximum NO_x conversion rate reaches a value of approximate 90% at the condition of 370℃ and 0.2 kg/s of the exhaust whilst the minimum NO_x conversion rate shows a value of approximate 54% at the exhaust gas condition of 250℃ and 0.55 kg/s.

5.4.3 Desired NH_3 slip control strategy

When the control objective is set as the desired amount of NH_3 slip, the sliding surface of the control strategy can be chosen as the difference between the measured and desired amount of NH_3 slip:

$$S = e_{NH_3} = C_{NH_3} - C_{NH_3,des} \quad \textbf{(5-20)}$$

Where:

e_{NH_3} : The difference of the measured and desired amount of NH_3 slip

C_{NH_3} : Measured amount of NH_3 slip

$C_{NH_3,des}$: Desired amount of NH_3 slip

The necessary condition for approaching the sliding surface is:

$$\begin{aligned} S\dot{S} < 0 \Rightarrow \dot{S} &= -M_{NH_3} sat(S/\phi) - K_{NH_3} S \\ \Rightarrow \dot{C}_{NH_3} &= -M_{NH_3} sat(S/\phi) - K_{NH_3} S \end{aligned} \quad \textbf{(5-21)}$$

Where:

M_{NH_3} , K_{NH_3} : Coefficients needed to be tuned in simulation , $M_{NH_3} > 0$, $K_{NH_3} > 0$

However, taking differential of Equation (4-24) and combining with Equations (4-22) and (4-23) will result in a quadratic form of $C_{NH_3,in}$ in the equation which is complex to solve. Thus, the control law of the desired NH_3 slip control strategy is designed as a combination of a feedforward term and a correction term.

Considering an equilibrium state of the system, where the differential of θ equals zero:

$$\dot{\theta} = k_{ads}(1-\theta)C_{NH_3} - k_{st}\theta C_{NO} - k_{ox}\theta - k_{des}\theta = 0 \quad \textbf{(5-22)}$$

Combining Equation (5-22) with Equations (4-23) and (4-24), $C_{NH_3,in}$ is derived:

$$C_{NH_3,in} = \frac{\left(\frac{k_{st}\theta\bar{Q}}{\bar{Q}+k_{st}\theta\Omega} C_{NO,in} + (k_{ox}+k_{des})\theta\right)\left(\bar{Q}+k_{ads}(1-\theta)\Omega\right)}{k_{ads}(1-\theta)\bar{Q}} - \frac{k_{des}\theta\Omega}{\bar{Q}} \quad \textbf{(5-23)}$$

Equation (5-23) will be used as the feedforward part of the control input. The complete control law can be generated by appending a correction term that penalises the deviation from the sliding surface. Thus the control law of the desired NH_3 slip control strategy is presented as below:

$$C_{NH_3,in} = \frac{\left(\frac{k_{st}\theta\bar{Q}}{\bar{Q}+k_{st}\theta\Omega}C_{NO,in}+\left(k_{ox}+k_{des}\right)\theta\right)\left(\bar{Q}+k_{ads}\left(1-\theta\right)\Omega\right)}{k_{ads}(1-\theta)\bar{Q}} - \frac{k_{des}\theta\Omega}{\bar{Q}} - M_{NH_3}sat(S/\phi) - K_{NH_3}S \quad \textbf{(5-24)}$$

5.4.4 Sliding mode controller implementation

The desired NO conversion rate control strategy and desired NH_3 slip control strategy introduced in section 5.4.2 and section 5.4.3 are implemented in MATLAB / Simulink environment with the 3-state SCR reactor model established in chapter 4 representing the actual SCR reactor. The maximum NO_x conversion rate map in Figure 5-1 is set as the control objective of the desired NO conversion rate control strategy and a constant value of 10 ppm for the amount of NH_3 slip is set the control objective of the desired NH_3 slip control strategy. The coefficients M_{NO}, K_{NO}, M_{NH_3} and K_{NH_3} in Equations (5-18) and (5-24) are tuned in the simulation and determined as: M_{NO} =5×10^{-8} s^{-1}, K_{NO} =80×10^{-4} s^{-1}, M_{NH_3} =1×10^{-2} s^{-1} and K_{NH_3} =2000 s^{-1} to obtain a stable and appropriate control result. The thickness of the boundary layers of the desired NO conversion rate control strategy and desired NH_3 slip control strategy is set as ϕ_{NO} =5 ppm and ϕ_{NH_3} =0.5 ppm respectively to relieve the chattering phenomenon. The diagrams of the desired NO conversion rate control strategy (named as NO sliding mode control strategy) and desired NH_3 slip control strategy (named as NH_3 sliding mode control strategy) are presented in Figure 5-2 and Figure 5-3 individually. The simulation results of the two control strategies will be presented in section 5.6.

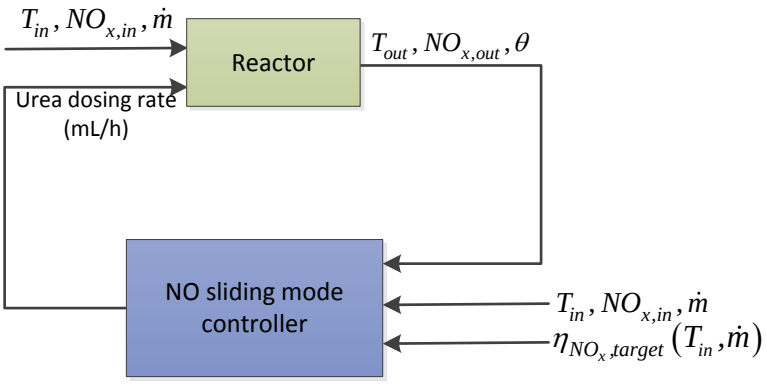

Figure 5-2 NO sliding mode control diagram

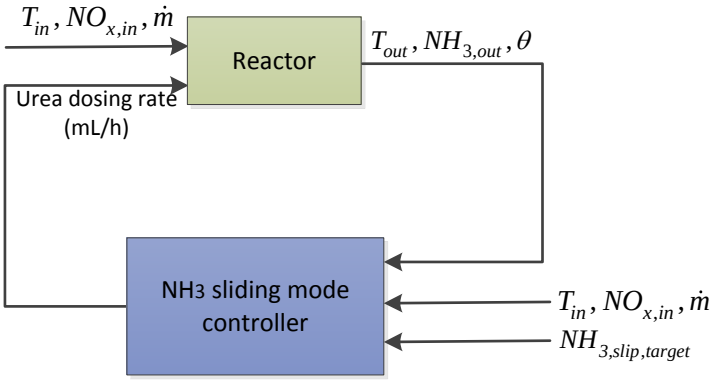

Figure 5-3 NH_3 sliding mode control diagram

5.5 Optimal control

5.5.1 Optimal control theory

The NO_x sliding mode control strategies presented in previous work [90][92] require to set an appropriate control objective of desired NO_x reduction rate in order to accomplish the control algorithm. However, it may be difficult to make compromise between the NO_x reduction rate and NH_3 slip. Thus, an optimal control strategy is developed in the study in order to compromise the NO_x conversion rate with NH_3 slip of an SCR system.

The linearised SCR model in Equation (5-7) can be regarded as a linear system with persistent disturbance. The controllability and observability of the linearised SCR

model analysed in section 5.3 show that the linearised SCR model is controllable and observable. Thus an optimal control strategy can be developed based on the linearised SCR model. The optimal controller can be designed as an infinite-horizon, continuous-time linear-quadratic regulator if the objective function of the control strategy takes the following form:

$$\min J = \frac{1}{2}\int_0^\infty \left(x^T Q x + u^T R u\right) dt \qquad \textbf{(5-25)}$$

Where:

J : Objective function

Q : Positive semi-definite real symmetric matrix, $Q = Q^T \geq 0$

R : Positive definite real symmetric matrix, $R = R^T > 0$

x : State vector

u : Input vector

In order to solve the optimal control problem shown in Equation (5-25) Pontryagin's minimum principle is used. The optimal control law should be chosen to minimise the Hamiltonian function:

$$H = \frac{1}{2}x^T Q x + \frac{1}{2}u^T R u + \lambda^T(t) A x + \lambda^T(t) B u + \lambda^T(t) W \omega \qquad \textbf{(5-26)}$$

Where:

H : Hamiltonian function

A : System matrix

B : Input matrix

W : Disturbance matrix

ω : Disturbance vector

$\lambda(t)$: Co-state variable vector

t : Time

The co-state equation is defined as:

$$\dot{\lambda}(t) = -\frac{\partial H}{\partial x} = -Qx - A^T \lambda(t) \tag{5-27}$$

$$\frac{\partial H}{\partial u} = Ru + B^T \lambda(t) = 0 \tag{5-28}$$

The optimal control law is determined as:

$$u^* = -R^{-1} B^T \lambda(t) \tag{5-29}$$

Where, u^* is the optimum control input.

Substituting the input vector in Equation (5-4) with Equation (5-29), it results in the following differential equations to be solved:

$$\begin{cases} \dot{\lambda}(t) = -Qx - A^T \lambda(t) \\ \dot{x}(t) = Ax - BR^{-1} B^T \lambda(t) + W\omega \end{cases} \tag{5-30}$$

At initial time point:

$$t = 0,\ x(0) = x_0;$$

Where x_0 is the initial value of the states

At infinite time point:

$$t = \infty,\ \lambda(\infty) = 0$$

In order to solve Equation (5-30), set $\lambda(t)$ as [107]:

$$\lambda(t) = Px + \bar{P}\omega \tag{5-31}$$

Where:

P and $\bar{P}$ are matrixes need to be determined

Taking derivatives of Equation (5-31) it results in:

$$\begin{aligned}\dot{\lambda}(t) &= P\dot{x} + \bar{P}\dot{\omega} \\ &= P(Ax - BR^{-1}B^T(Px + \bar{P}\omega) + W\omega) + \bar{P}\dot{\omega} \\ &= (PA - PBR^{-1}B^TP)x - PBR^{-1}B^T\bar{P}\omega + PW\omega + \bar{P}\dot{\omega}\end{aligned} \tag{5-32}$$

At a steady state operating condition, $\dot{\omega}$=0. Thus combining Equations (5-30), (5-31) and (5-32), it derives:

$$(A^TP + PA - PBR^{-1}B^TP + Q)x + (A^T\bar{P} - PBR^{-1}B^T\bar{P} + PW)\omega = 0 \tag{5-33}$$

As Equation (5-33) is applicable to an arbitrary x and ω, solving Equation (5-33) results in an algebraic Riccati equation in Equation (5-34) and a matrix equation in Equation (5-35):

$$A^TP + PA - PSP + Q = 0 \tag{5-34}$$

$$(A - SP)^T\bar{P} = -PW \tag{5-35}$$

Where $S = BR^{-1}B^T = S^T$.

It is known that the algebraic Riccati equation in Equation (5-34) has a unique positive definite solution P>0 if and only if (A, B) is controllable and $(A, Q^{1/2})$ is observable [108]. The existence of the solution of the matrix equation in Equation (5-35) is proved as follows:

For a linear system without disturbance:

$$\dot{x} = Ax + Bu \tag{5-36}$$

Take the same quadratic performance index as the objective function as shown in Equation (5-25), the optimal control law of the linear system without disturbance is:

$$u^* = -R^{-1}B^T Px \tag{5-37}$$

Substituting the input vector u in Equation (5-36) with Equation (5-37), it obtains a closed loop system:

$$\begin{aligned} \dot{x} &= (A - BR^{-1}B^T P)x \\ &= (A - SP)x \end{aligned} \tag{5-38}$$

If the closed loop system in Equation (5-38) is stable the following condition is satisfied:

$$\mathrm{Re}\left[\lambda_i(A - SP)\right] < 0,\ i = 1, 2, \cdots, n \tag{5-39}$$

Where:

Re[]: Take the real part of a complex number

$\lambda_i()$: The eigenvalue of a matrix

Equation (5-39) shows that $\lambda_i((A - SP)^T) \neq 0$, which means Equation (5-35) has a unique solution of $\overline{P}$. Therefore, the co-state variable vector $\lambda(t)$ in Equation (5-31) can be solved and the optimal control law in Equation (5-29) can be obtained.

5.5.2 Optimal controller design

In this section, an optimal controller for urea dosing rate will be designed according to the optimal control theory introduced in section 5.5.1. The objective function of the optimal control strategy is defined in the following quadratic form:

$$\min J = \frac{1}{2}\int_0^\infty \left(\gamma_{NO} C_{NO}^2 + \gamma_{NH_3} C_{NH_3}^2 + u^2\right) dt \qquad \textbf{(5-40)}$$

Where:

γ_{NO}, γ_{NH_3}: Weighted factors, $\gamma_{NO} > 0$, $\gamma_{NH_3} > 0$

Compared Equations (5-25) with (5-40), it obtains that:

$$x = \begin{bmatrix} C_{NO} \\ \theta \\ C_{NH_3} \end{bmatrix}, \; Q = \begin{bmatrix} \gamma_{NO} & 0 & 0 \\ 0 & 0 & 0 \\ 0 & 0 & \gamma_{NH_3} \end{bmatrix}, \; R = 1 \qquad \textbf{(5-41)}$$

Since the weighted factors γ_{NO} and γ_{NH_3} are both positive, Q is a positive semi-definite real symmetric matrix. The observability of $(A, Q^{1/2})$ can be determined by checking the rank of the observability matrix as below:

$$U_O = \begin{bmatrix} Q^{1/2} \\ Q^{1/2}A \\ Q^{1/2}A^2 \end{bmatrix} = \begin{bmatrix} \sqrt{\gamma_{NO}} & 0 & 0 \\ 0 & 0 & 0 \\ 0 & 0 & \sqrt{\gamma_{NH_3}} \\ A_{11}\sqrt{\gamma_{NO}} & A_{12}\sqrt{\gamma_{NO}} & 0 \\ 0 & 0 & 0 \\ 0 & A_{32}\sqrt{\gamma_{NH_3}} & A_{33}\sqrt{\gamma_{NH_3}} \\ \left(A_{11}^2 + A_{12}A_{21}\right)\sqrt{\gamma_{NO}} & \left(A_{11}+A_{22}\right)A_{12}\sqrt{\gamma_{NO}} & A_{12}A_{23}\sqrt{\gamma_{NO}} \\ 0 & 0 & 0 \\ A_{11}A_{32}\sqrt{\gamma_{NH_3}} & \left(A_{22}+A_{33}\right)A_{32}\sqrt{\gamma_{NH_3}} & \left(A_{23}A_{32}+A_{33}^2\right)\sqrt{\gamma_{NH_3}} \end{bmatrix} \quad \textbf{(5-42)}$$

Where:

U_O: Observability matrix

A: System matrix as shown in Equation (5-7)

The observability matrix U_O has a full rank of 3 because that $A_{12} \neq 0$, which means $(A,\ Q^{1/2})$ is observable. Combined with the condition that $(A,\ B)$ is controllable, the algebraic Riccati equation in Equation (5-34) has a unique positive definite solution.

The optimal control law can be written as $u^* = -R^{-1}B^T Px - R^{-1}B^T \bar{P}\omega$ if combining Equations (5-29) and (5-31). It will be regarded as an optimal controller which consists of feedforward and feedback parts. The amount of urea injection from the feedforward part will be calculated according to the value of disturbance, and the amount of urea injection from the feedback part will be calculated based on the rules of pursuing the minimum of the objective function as presented in Equation (5-40).

5.5.3 Optimal controller implementation

The optimal controller developed in section 5.5.2 is implemented in MATLAB / Simulink environment with the 3-state SCR reactor model established in chapter 4

representing the actual SCR reactor. Due to the complexity of solving the algebraic Riccati equation in Equation (5-34), P is calculated by a numerical solution using the function of *CARE* in MATLAB because that it is difficult to obtain the analytic solution for P. The main purpose of developing urea control strategy is to reduce the concentration of NO and NH_3 after the reactor other than saving urea. The weighted factors γ_{NO} and γ_{NH_3} should be chosen as a large number compared to the weighted factor of urea which is 1 as shown in Equation (5-40). Thus, the weighted factors are tuned in the simulation and determined as γ_{NO}=800 and γ_{NH_3}=30000 in order to weaken the proportion of the input u in the objective function in Equation (5-40) and obtain a satisified NO conversion rate and acceptable NH_3 slip. The optimal control strategy diagram is presented in Figure 5-4.

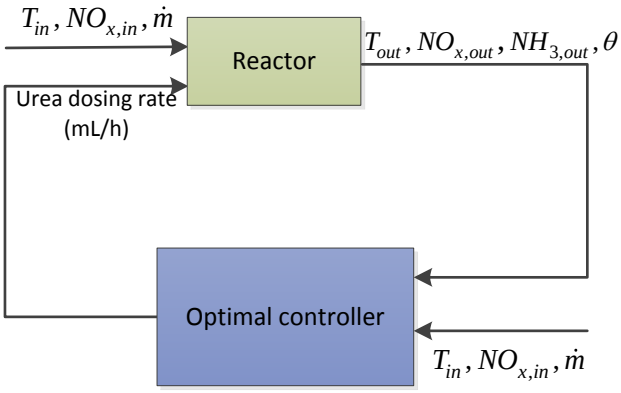

Figure 5-4 Optimal control strategy diagram

5.6 Simulation results

The NO sliding mode control strategy, NH_3 sliding mode control strategy and optimal control strategy were tested in MATLAB / Simulink environment. The SCR operating condition used in the simulation utilises the experimental data shown in section 4.4.2. The simulation results are presented in Figure 5-5 to Figure 5-7.

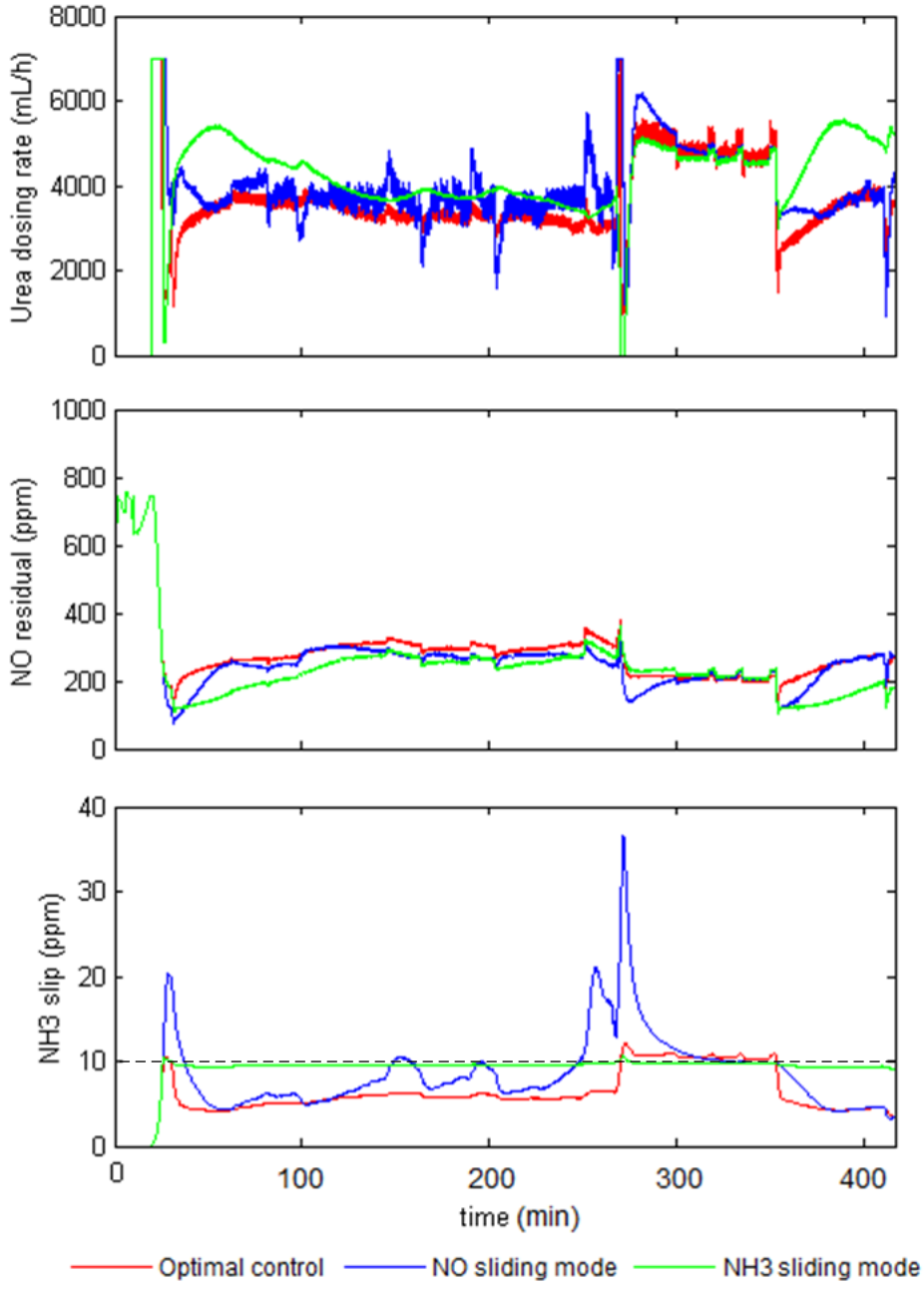

Figure 5-5 Comparison of sliding mode control and optimal control strategies under steady state engine operating points of 25% load (75 kW) and 100% load (300 kW)

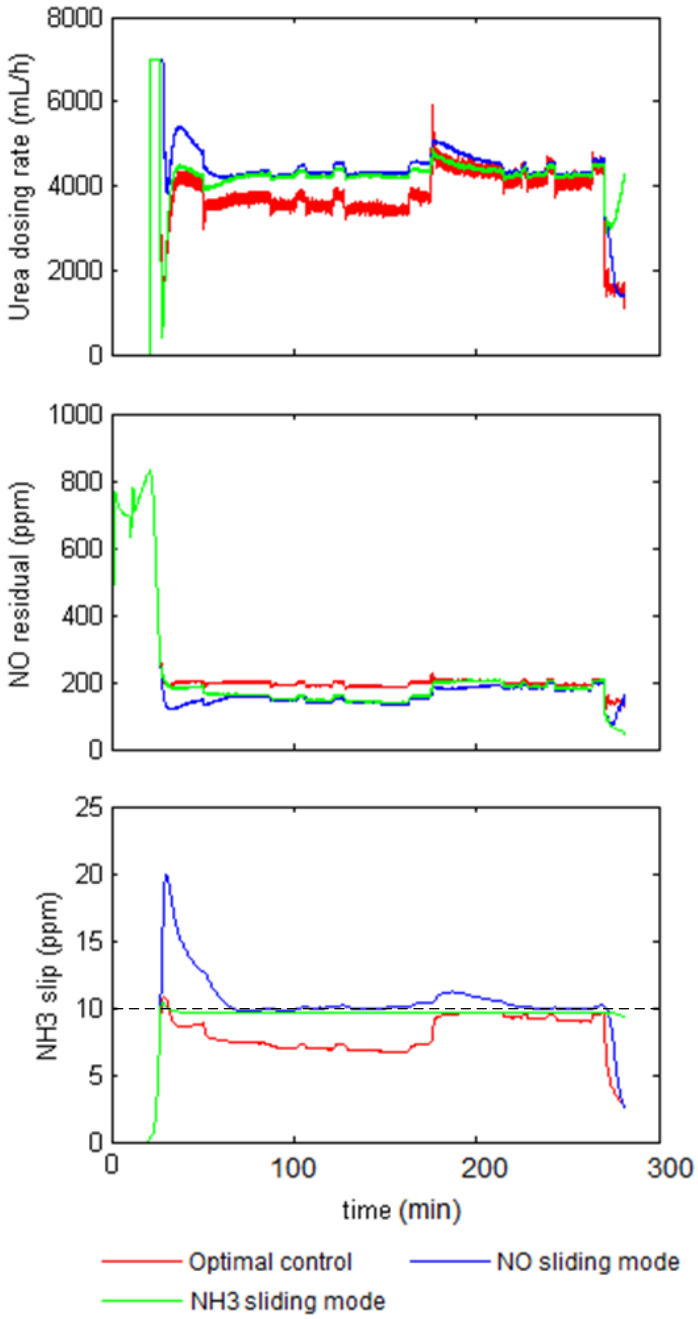

Figure 5-6 Comparison of sliding mode control and optimal control strategies under steady state engine operating points of 50% load (150 kW) and 75% load (225 kW)

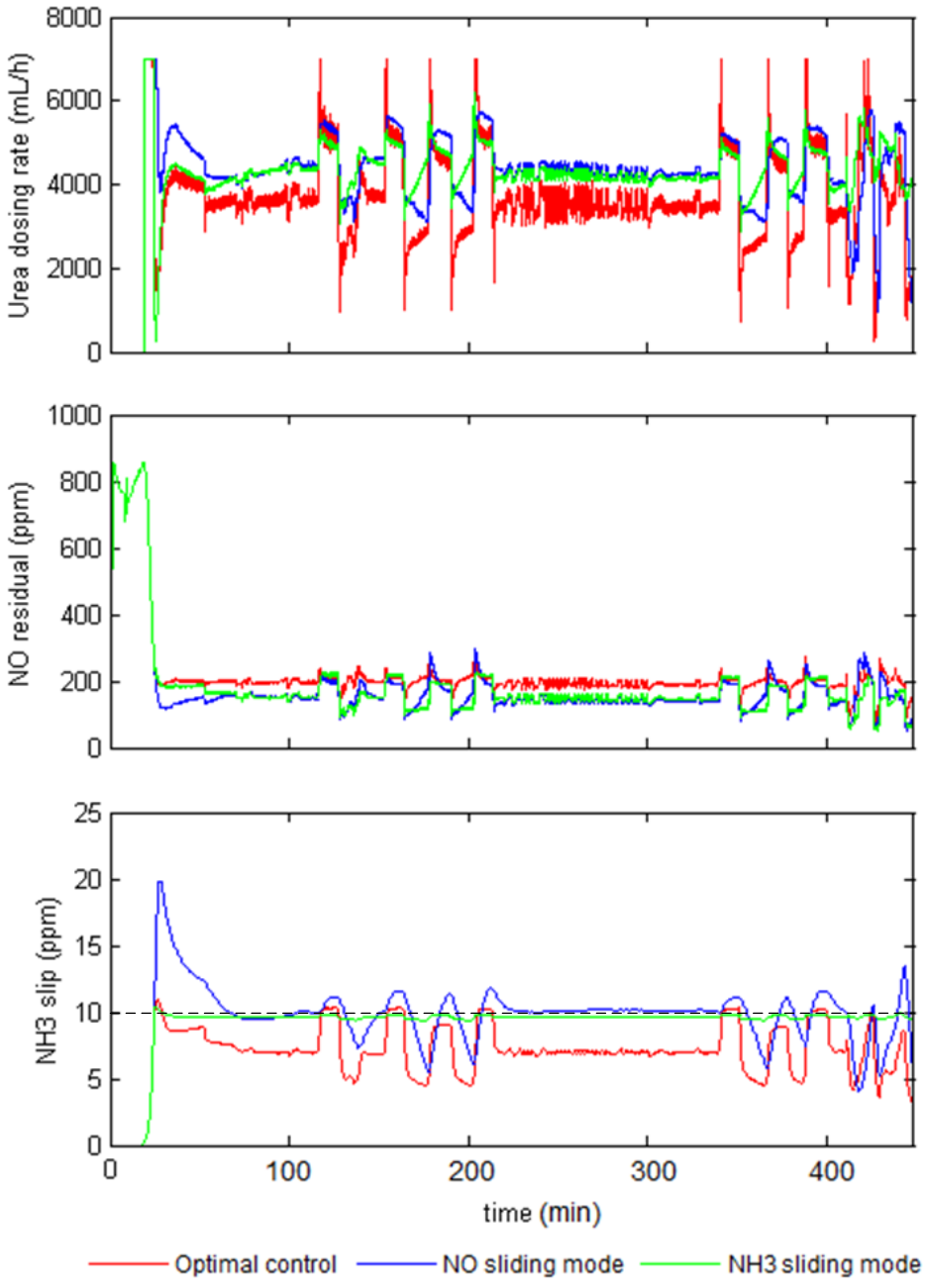

Figure 5-7 Comparison of sliding mode control and optimal control strategies under transient state engine operating condition

Figure 5-5 to Figure 5-7 present that the NO sliding mode control, NH_3 sliding mode control and optimal control show a moderate difference on the values of the urea dosing rate, NO residual and NH_3 slip. When the value of the NO residual satisfies the requirement of NO_x emission regulations, a small value of NH_3 slip and the least urea consumption are pursued. Among the 3 control strategies, the optimal control obtains the smallest value of NH_3 slip due to less urea injected throughout the simulation. At the beginning of the simulation, the NH_3 slip of the NO sliding mode control at the time point of approximate 25 min reaches a value of approximate 20 ppm which is almost twice that of the NH_3 sliding mode control and optimal control. For an easy comparison of each control strategies, the average and peak NH_3 slip, the average NO residual and the total urea consumption in the simulation are also summarised in Appendix 2.

5.7 Chapter summary

This chapter presents the sliding mode urea control strategies which have been studied in previous work [102][103]. The 3-state reactor model developed in chapter 4 is linearised at an equilibrium point which leads to a linear state space model. Based on the linear state space model, the optimal control strategy is developed in order to compromise the NO_x conversion rate with NH_3 slip. The optimal control strategy developed in the study is further compared with the sliding mode control strategies in order to investigate the performance of each control strategies. The simulation uses the experimental data shown in section 4.4.2 as the input data of all the control strategies. The simulation results show that the NO sliding mode control requires a massive pre-study of the NO_x reduction capability of the catalyst in order to set an appropriate control objective for each operating condition. However, this calibration work can be omitted in the optimal control and NH_3 sliding mode control, which mitigates the workload of the controller design. Thus, the NH_3 sliding mode control and the optimal control are recommended for the calculation of urea dosing rate. The model-based control strategies introduced in this chapter require the information of the NH_3 surface coverage fraction θ that can not be measured by

sensors. Thus, a state observer will be established in order to estimate the value of θ in the catalyst. The state estimation process will be discussed in next chapter.

Chapter 6.

STATE ESTIMATION

The model-based control strategies developed in chapter 5 require full information of the system states to calculate urea dosing amount. However some of the system states like NH_3 surface coverage fraction θ cannot be measured by sensors. This problem can be addressed by establishing a state observer which can estimate the system states based on the information of measureable states. The existence of NH_3 in the exhaust may affect the accuracy of NO_x sensors. Thus the NH_3 cross-sensitivity of NO_x sensors needs to be studied. Section 6.1 investigates the NH_3 cross-sensitivity of NO_x sensors and section 6.2 establishes a linear state observer to estimate system states. Section 6.3 presents the simulation results of the observer.

6.1 NH_3 cross-sensitivity of NO_x sensors

The state-of-the-art smart NO_x sensors are cross-sensitive to NH_3, which may overrate the measurement of NO_x emission when ammonia exists in the exhaust. The NH_3 cross-sensitivity of NO_x sensors can be modelled using the following equation [109]:

$$C_{NO_{x,sen}} = C_{NO_x} + K_{cs} C_{NH_3} \quad \textbf{(6-1)}$$

Where:

K_{cs} : Cross-sensitivity factor, ranging from 0.5 to 2 [110]

$C_{NO_{x,sen}}$: Reading from NO_x sensor

C_{NO_x} , C_{NH_3} : Actual concentration of NO_x and NH_3 in exhaust

An experiment has been conducted on the SCR experiential test rig for a diesel generator of 38 kW as introduced in Appendix 1 in order to investigate the NH_3 cross-sensitivity of NO_x sensor. For the experiment, a NO_x sensor was installed upstream the urea injector while another identical NO_x sensor together with a NH_3 sensor was installed downstream the urea injector as shown in Figure 6-1.

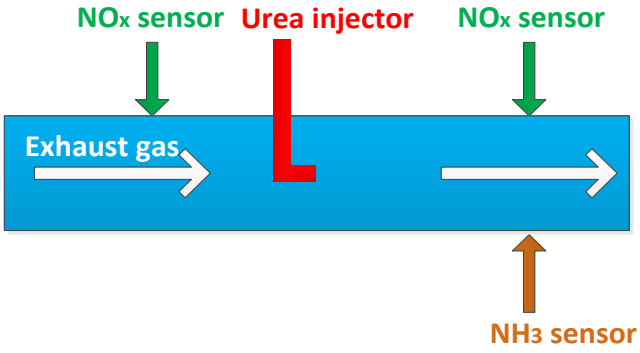

Figure 6-1 Layout of experiment on NH_3 cross-sensitivity of NO_x sensor

The reading of the upstream NO_x sensor can be regarded as the actual NO_x concentration. The measurement from the downstream NO_x sensor may be affected by the presence of NH_3 in the exhaust. In order to observe the NH_3 cross-sensitivity of NO_x sensor under different NH_3 concentration conditions, urea is dosed at a rate to generate NH_3 of a concentration ranging from 50 ppm to 200 ppm in the exhaust. The temperature of the exhaust ranges from 280°C to 350°C. The measured concentration of NO_x and NH_3 in the exhaust and the data fitting results of Equation (6-1) are shown in Figure 6-2.

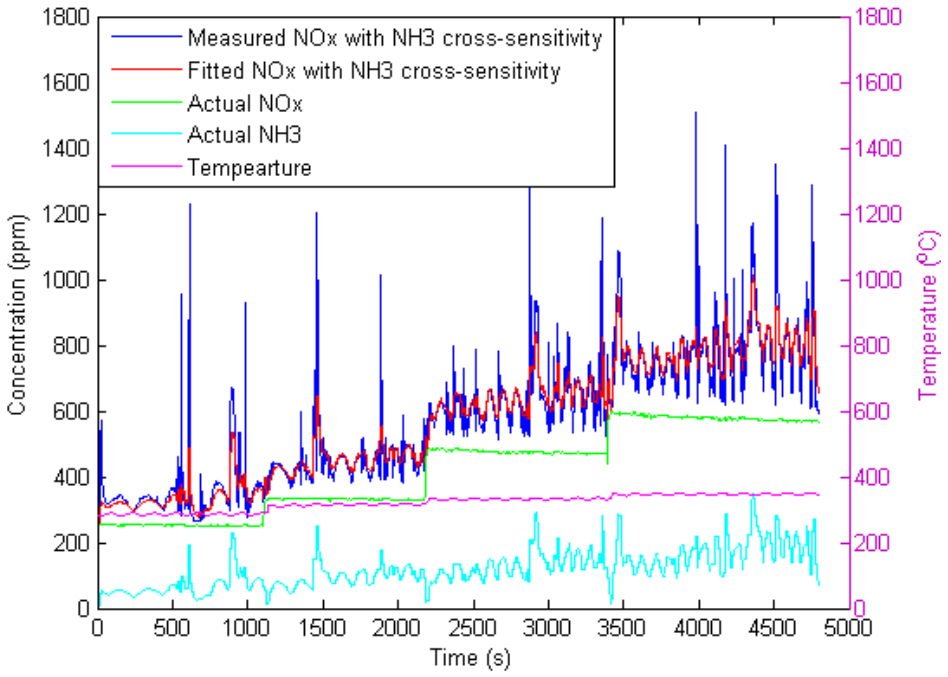

Figure 6-2 Data fitting results of NH_3 cross-sensitivity of NO_x sensor

Figure 6-2 shows a satisfied match between the measured and fitted NO_x concentration downstream the urea injector. The cross-sensitivity factor K_{cs} in Equation (6-1) is thus determined as a constant of 1.239 according to the data fitting results of the measurement values of $C_{NO_{x,sen}}$, C_{NO_x} and C_{NH_3}. The deviation between the measured and fitted NO_x concentration downstream the urea injector in Figure 6-2 mainly exists at the peaks of the measured NO_x concentration, which can be regarded as measurement noise. Thus, Equation (6-1) will be used to provide the value of the NO_x signal from a NH_3 cross-sensitive NO_x sensor in the following simulation studies.

6.2 State observer

The model-based control strategies developed in chapter 6 require full information of the system states (C_{NO}, θ, C_{NH_3}) to calculate urea dosing amount. Although it has been reported that the NH_3 surface coverage fraction θ is measureable by using specific instruments [111], this technique has not been applied to sensors. Thus,

observer design is still the main method to estimate θ. Both linear and nonlinear observers [102][112][113] have been studied in recent years to estimate θ. In this study, a linear observer is used for the purpose of easy implementation:

The linear observer can be written as below:

$$\dot{\hat{x}} = \vec{f}\left(\hat{x}, u, d\right) + \vec{L}\left(C_i - \hat{C}_i\right) \quad \textbf{(6-2)}$$

Where :

$\hat{x}$: Estimated states, $\hat{x} = [\hat{C}_{NO} \quad \hat{\theta} \quad \hat{C}_{NH_3}]$

C_i , $\hat{C}_i$: The measured and estimated values of a variable, $i = NO,\ NH_3$

$\vec{f}$: The 3-state chemical dynamic equations shown in Equations (4-20) to (4-22)

$\vec{L}$: Observer gains

6.3 Observer simulation

The NH_3 cross-sensitivity of NO_x sensors have been modelled in previous work [109][110]. However, the effect of the NH_3 cross-sensitivity of NO_x sensors on the accuracy of the estimation results of the observer has not been revealed. The linear observer in Equation (6-2) can be established based on the feedback signal from either NO sensor or NH_3 sensor after the reactor. Thus two linear observers were implemented in MATLAB Simulink based on the NO_x feedback signal and NH_3 feedback signal respectively. The 3-state SCR reactor model established in chapter 4 is regarded as the actual SCR reactor in the simulation. In order to present the effect of the NH_3 cross-sensitivity of NO_x sensor on the accuracy of the estimation results of the observer, the NO_x feedback signal used in the simulation is a sum of the actual NO concentration and the cross-sensitive NH_3 concentration as presented in Equation (6-1). The simulation runs over 400 s starting from the 7000st s of the experimental data of the steady state engine operating points of 25% load (75 kW) and 100% load (300 kW) as shown in Figure 4-9 and Figure 4-10. The actual states of the 3-state

SCR model at the time point of 7000 s are C_{NO} =520 ppm, C_{NH_3} =1.4 ppm, and θ =0.213. The initial states of the observers are set as $\hat{C}_{NO}$ =520 ppm, $\hat{C}_{NH_3}$ =1.4 ppm, and $\hat{\theta}$ =0.5. The aim of the simulation is to test the tracking performance of the observers to the actual states.

The observer gains $\vec{L}$ should be chosen as values to guarantee the stability of the observer. The sign of each value in matrix $\vec{L}$ can be determined according to the physical process of the SCR reactor, namely, a positive error of $C_{NO}-\hat{C}_{NO}$ should create a positive correction on the state C_{NO} and negative penalties on the states θ and C_{NH_3}. Thus, the first element of the observer gains matrix for NO_x feedback observer should be positive and other elements in the matrix should be negative. In contrast, a positive error of $C_{NH_3}-\hat{C}_{NH_3}$ should create a positive correction on the states θ and C_{NH_3} and negative penalty on the state C_{NO}. Thus, the first element of the observer gains matrix for NH3 feedback observer should be negative and other elements in the matrix should be positive. The observer gains are tuned in the simulation and determined as $\vec{L}=\begin{bmatrix}2; & -1.4; & -1.2\end{bmatrix}$ for NO_x feedback observer and $\vec{L}=\begin{bmatrix}-300 & 280 & 240\end{bmatrix}$ for NH_3 feedback observer in order to fast track the actual states and guarantee the stability of the observers. The open loop observer estimates the states based on the dynamics of the SCR reactions shown in section 4.2.2 without any feedback signals from the measurement, namely, $\vec{L}=\begin{bmatrix}0 & 0 & 0\end{bmatrix}$. The simulation results are presented in Figure 6-3.

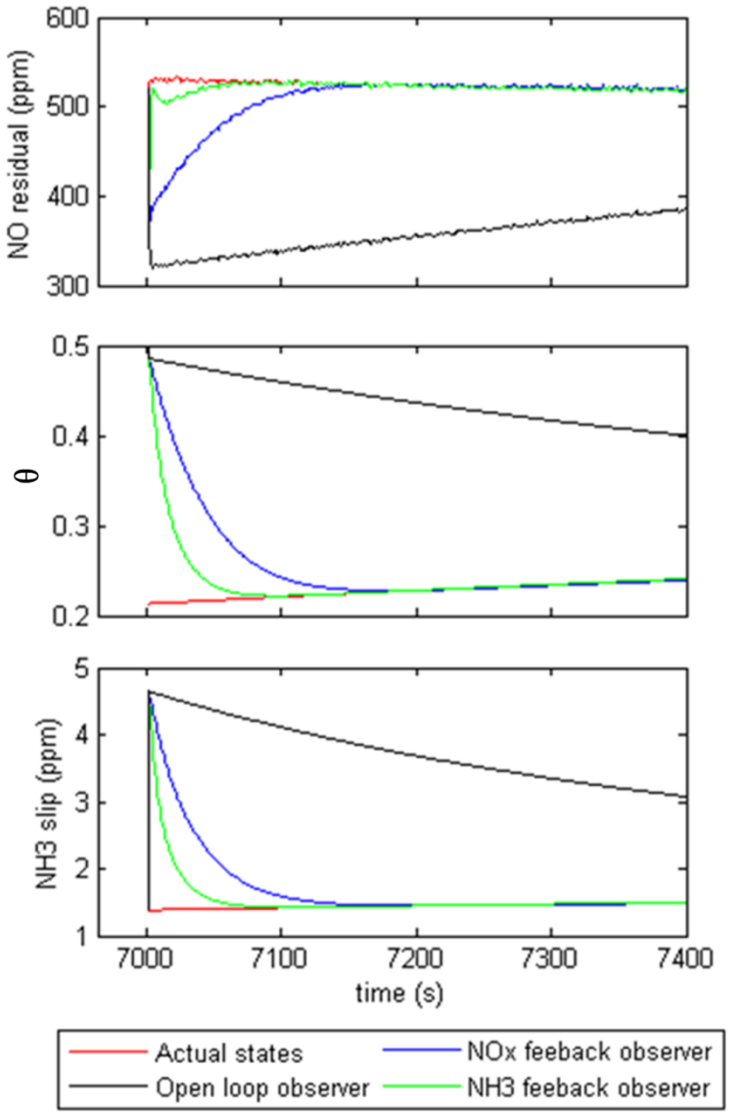

Figure 6-3 Tracking performance of observers to the actual states

Figure 6-3 presents that the NH_3 feedback observer tracks the actual states with a converging time of around 100 s which is faster than that (180 s) of the NO_x feedback observer. The converging time of the open loop observer relies strongly on the initial values of estimation. It responds much slower to the difference between the estimated and actual states due to lack of feedback as shown in Figure 6-3.

In order to investigate the effect of the NH_3 cross-sensitivity of NO_x sensors on the adequacy of the NO_x feedback observer estimation, the NO_x feedback observer and NH_3 feedback observer are further compared in a comprehensive simulation which

comprises a 3-state SCR reactor model, an observer and an optimal controller in the architecture. The observer utilises the feedback signals from either a NH_3 sensor (regarded as NH_3 feedback observer) or a NH_3 cross-sensitive NO_x sensor (regarded as NO_x feedback observer) to investigate the effect of the estimation of the states on the control performance of urea injection. The simulation framework is presented in Figure 6-4.

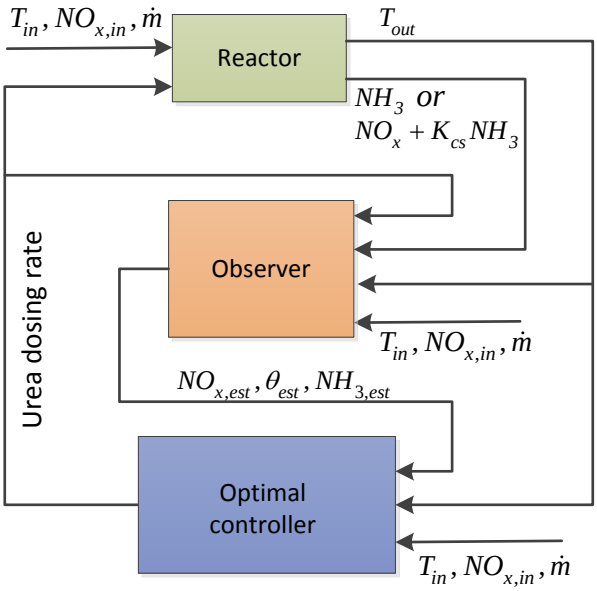

Figure 6-4 Framework of comprehensive control simulation

The simulation runs starting from the 7000st s of the experimental data of the steady state engine operating points of 25% load (75 kW) and 100% load (300 kW) as shown in Figure 4-9 and Figure 4-10. The actual states of the 3-state SCR model at the time point of 7000 s are C_{NO} =520 ppm, C_{NH_3} =1.4 ppm, and θ =0.213. The initial states of the observers are set as $\hat{C}_{NO}$ =520 ppm, $\hat{C}_{NH_3}$ =1.4 ppm, and $\hat{\theta}$ =0.5. The controller uses the estimated states provided by the observer to calculate the urea dosing rate. The simulation results are presented in Figure 6-5.

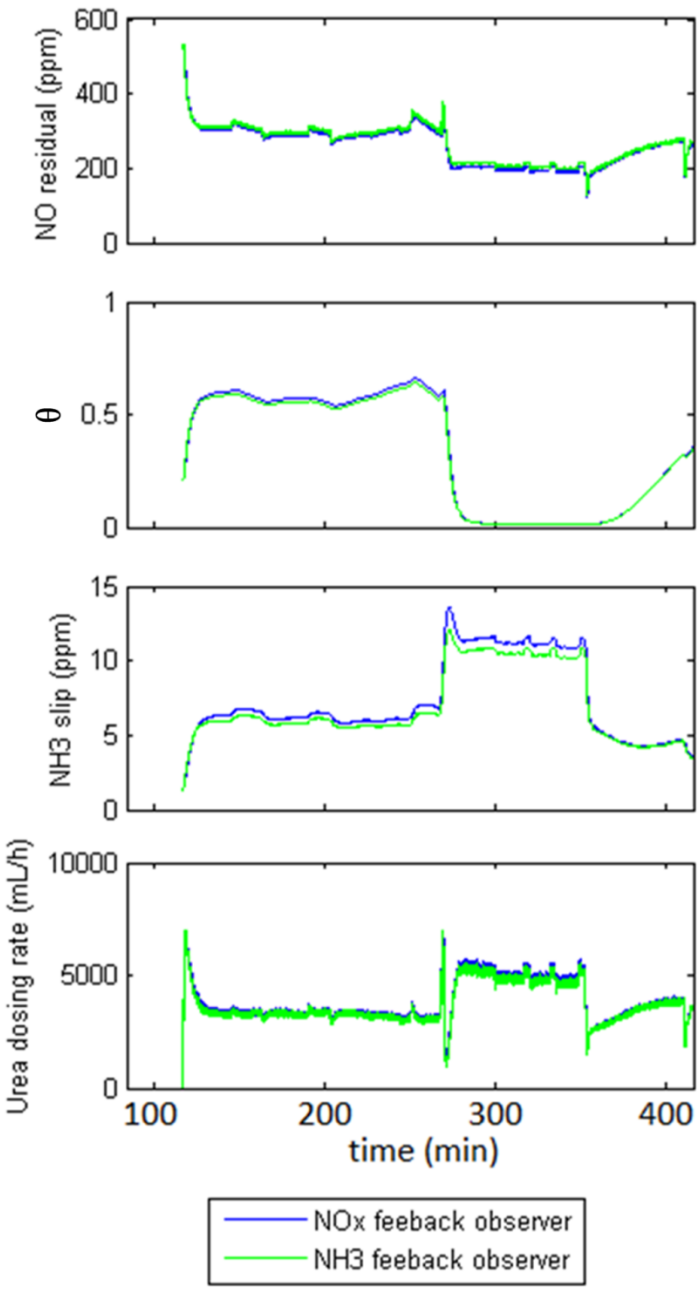

Figure 6-5 Validation of observers in a comprehensive simulation

Figure 6-5 shows that the simulation results of the NO_x feedback observer and the NH_3 feedback observer agree significantly. Although the NO_x feedback observer is not as accurate as the NH_3 feedback observer on the estimation of the states due to the NH_3 cross-sensitivity of NO_x sensor, it has not influenced the control performance of urea injection significantly.

6.4 Chapter summary

This chapter investigates the NH_3 cross-sensitivity of NO_x sensors and establishes a linear state observer in order to estimate the system states based on the information of measureable states. The simulation results of the observer suggest that the NH_3 cross-sensitivity of NO_x sensors can be neglected when NH_3 is of a low concentration of compared to that of NO_x. When NH_3 sensor is unavailable, the NO_x feedback observer is able to estimate the states in the reactor. Thus, both the NO_x feedback observer and the NH_3 feedback observer can be used to estimate the states in the reactor for developing the model-based control strategies introduced in chapter 5.

Chapter 7.

CONCLUSIONS AND RECOMMENDATIONS

7.1 Conclusions

The following conclusions are drawn based on the performed research:

1. The travel distance of UWS droplets depends on the total droplet depletion time, bulk exhaust velocity and droplet initial velocity.

2. The droplet depletion time is influenced by many factors such as the droplet diameter, the mass fraction of urea in the UWS droplet, the relative velocity between the droplet and exhaust, the pressure and temperature of exhaust, and the temperature of the droplet. The velocity of the exhaust in engine pipeline ranges from approximate 30 m/s to 50 m/s. Thus, a distance from 2m to 3m is recommended for the distance between the urea nozzle and reactor for an SCR system design from the perspective of urea decomposition.

3. A uniform mixing of the ammonia and exhaust is pursued during the design of an SCR system in order to achieve a high NO_x conversion rate and a low amount of NH_3 slip. 4 novel static mixers are developed in order to promote the mixing degree of ammonia before the reactor. It is necessary to evaluate the performance of the static mixers comprehensively including the mixing homogenization, velocity uniformity and pressure loss of the flow generated by the static mixers. Both the simulation and experiment show that the Box mixer

performs effectively in respect of these aspects. Thus, the Box mixer is recommended to be applied on SCR systems in order to deal with the mixing problem.

4. 3-state SCR reactor model is established with the unknown parameters of the model estimated by experiment. The 3-state reactor model is further simplified to a 1-state reactor model. Both the 3-state reactor model and 1-state reactor model are capable to predict the behaviour and performance of the SCR reactor investigated in a wide range of operating conditions. Thus, the 3-state reactor model and 1-state reactor model are used to develop model-based urea dosing control strategies.

5. NO_x sliding mode control strategy needs the pre-study of catalyst in order to set an appropriate control objective of desired NO_x conversion rate. For the purpose of omitting massive calibration work, NH_3 sliding mode control is used. In order to compromise the NO_x conversion rate with NH_3 slip of an SCR system, an optimal control strategy is developed in the study. It calculates the urea dosing rate based on the 3-state SCR reactor model, which enables the controller to respond to the variations of operating conditions in advance. The optimal control strategy presents a satisfied control performance in limiting NH_3 slip during transient state engine operating conditions.

6. A linear state observer is established in order to estimate the ammonia surface coverage fraction θ in the SCR reactor. The NH_3 cross-sensitivity of NO_x sensors is described by a linear equation and neglected when NH_3 is of a low concentration in the exhaust. Thus, both the NO_x feedback observer and the NH_3 feedback observer can be used to estiamte the states in the reactor for developing model-based urea control strategies.

7.2 Contributions

The contributions of the study include:

1. The evaporation and decomposition time of UWS droplets in various diameters under different temperature are calculated. The travel distance of UWS droplets calculated is helpful to determining the distance between the urea nozzle and reactor.

2. The evaluation procedure for the static mixers in SCR systems can also be used to evaluate static mixers in other occasions. The Box mixer developed is recommended to be applied on SCR systems to deal with the mixing problem.

3. The kinetic parameters and heat transfer coefficient of the reactor model are estimated for a specific SCR reactor. The reactor model established in the study is used to predict the behaviour and performance of the SCR reactor in a wide range of operating conditions.

4. The optimal control strategy developed is used to compromise the NO_x conversion rate with NH_3 slip of the SCR system.

5. The NO_x feedback observer is used to estiamte the states in the reactor because the NH_3 cross-sensitivity of NO_x sensors can be neglected when NH_3 is of a low concentration in the exhaust.

7.3 Innovations

The innovations of the study are summarised as below:

1. Droplet motion is solved in conjunction with the evaporation and decomposition processes of a UWS droplet.

2. 4 novel static mixers are developed. The Box mixer presents effective mixing ability and low pressure loss over the flow.

3. The static mixers are evaluated comprehensively considering the species homogenisation, velocity uniformity and pressure loss of the flow generated by the static mixers. The 'mixing for free' ability of the mixers is analysed by simulation.

4. The chemical kinetic parameters of the catalytic reactions and the heat transfer coefficient vary with the type of SCR catalyst. For a specific SCR reactor, these parameters are unknown and need to be determined by experiment. This study estimated these unknown parameters for the SCR test rig, which are used to develop the reactor model.

5. Optimal control theory is applied to develop optimal urea control strategy based on the 3-state reactor model.

7.4 Recommendations for future work

Based on the study in this thesis, the following research is recommended for future work:

1. The optimal control strategy developed in the study is investigated by simulation. Thus, physical implementation of the optimal control strategy in a programmable logic controller (PLC) is recommended for future work in order to validate the control performance. Physical implementation of the optimal control strategy requires 2 NO_x sensors which locate before and after the reactor respectively. The 3-state reactor model and the NO_x feedback observer presented in the study need to be embedded in the PLC. The NO_x feedback observer in the PLC estimates the values of the NH_3 surface coverage fraction and the concentration of NH_3 in the reactor based on the measured NO_x concentration from the NO_x sensor after the reactor. The urea dosing rate is thus calculated according to the optimal control algorithm embedded in the PLC.

2. The stability, robustness, response and errors of the controllers will be examined in future study.

3. A monitoring and fault diagnosis system can be developed and incorporated in the controller in order to accomplish a full system control.

4. The formation of soot deposit on the catalyst surface needs to be investigated for the design of a soot blowing system.

Publications

Journals

Xinna Tian, Youhong Xiao, Peilin Zhou, Wenping Zhang. Study on the mixing performance of static mixers in SCR application. Journal of Marine Engineering and Technology, Vol. 14, No. 2, 2015.

Xinna Tian, Youhong Xiao, Peilin Zhou and Wenping Zhang. Optimization of the location of injector in urea-selective catalytic reduction system. Journal of Marine Science and Technology, Vol. 20, No. 2, p. 238-248, 2015.

Xinna Tian, Youhong Xiao, Peilin Zhou and Wenping Zhang. Investigation on performance of V_2O_5-WO_3–TiO_2-cordierite catalyst modified with Cu, Mn and Ce for urea-SCR of NO. Materials Research Innovations, Vol. 18, No. S2, p. 202-206, 2014.

Xinna Tian, Wenping Zhang, Youhong Xiao and Peilin Zhou. Investigation on the effect of ammonia distribution on selective catalytic reduction conversion efficiency. Asian Journal of Chemistry, Vol. 24, No. 12, p. 5889-5893, 2012.

Xinna Tian, Youhong Xiao, Wenping Zhang and Yongwei Chen. Investigation of the performance of V-W based catalysts at low temperature for NO_x reduction with NH_3. Advanced Materials Research, Vol. 197-198, p. 811-816, 2011.

Youhong Xiao, **Xinna Tian**, Peilin Zhou and Wenping Zhang. Study on evaporation and decomposition process of urea water solution in selective catalytic reduction system. Materials Research Innovations, Vol.18, No.S2, p. 908-913, 2014.

Youhong Xiao, **Xinna Tian** and Peilin Zhou. Studying on the emission characteristic of a diesel engine by simulation. Asian Journal of Chemistry, Vol. 24, No. 12, p. 5897-5902, 2012.

Conferences

Xinna Tian, Youhong Xiao and Wenping Zhang. Numerical simulation of urea aqueous solution injection process in a selective catalytic reduction system. 4th International Conference on Bioinformatics and Biomedical Engineering, 2010.

Patents

Xinna Tian, Wenping Zhang, Youhong Xiao, Xinyu Zhang, Pingjian Ming, Yipeng Cao, Gongmin Liu. Preheat-nozzle static mixer. 2012.8.15-2032.4.17, Heilongjiang, China, CN201210111775.7

Wenping Zhang, **Xinna Tian**, Youhong Xiao. Torsion static mixer. 2014.3.5-2033.11.29, Heilongjiang, China, CN201310624960.0

Wenping Zhang, **Xinna Tian**, Youhong Xiao, Pingjian Ming, Xinyu Zhang, Gongmin Liu, Yipeng Cao. Helix static mixer. 2014.3.12-2033.11.29, Heilongjiang, China, CN201310624992.0

Youhong Xiao, **Xinna Tian**, Wenping Zhang, Xinyu Zhang, Pingjian Ming, Gongmin Liu, Yipeng Cao. Baffle static mixer. 2014.2.19-2033.11.20, Heilongjiang, China, CN201310585636.2

Youhong Xiao, **Xinna Tian**, Wenping Zhang, Pingjian Ming, Xinyu Zhang, Yipeng Cao, Gongmin Liu. Boxer static mixer. 2014.2.19-2033.11.20, Heilongjiang, China, CN201310585619.9

Youhong Xiao, **Xinna Tian**, Wenping Zhang, Wei Zheng, Zhenhao Chu, Guoxue, Lyu. A method of measuring the homogenization of ammonia concentration in SCR systems' pipeline. 2014.8.6-2034.5, Heilongjiang, China, CN201410195408.9

References

[1] Goldsworth L. Design of Ship Engines for Reduced Emissions of Oxides of Nitrogen. Available from www.flamemarine.com.

[2] Corbett JJ and Fischbeck P. Emissions from Ships. Science, Vol. 278, No. 5339, p. 823-824, 1997.

[3] Hall L. Sulphur Requirements in IMO Emission Control Areas. 2015. Available from http://www.shipownersclub.com/louise-hall-sulphur-requirements-imo-emission-control-areas/.

[4] Blatcher DJ and Eames I. Compliance of Royal Naval Ships with Nitrogen Oxide Emissions Legislation. Marine Pollution Bulletin, Vol. 74, No. 1, p. 10-18, 2013.

[5] Mohan B, Yang WM and Chou SK. Fuel Injection Strategies for Performance Improvement and Emissions Reduction in Compression Ignition Engines – A review. Renewable and Sustainable Energy Reviews, Vol. 28, p. 664-676, 2013.

[6] Talebizadeh P, Babaie M, Brown R, Rahimzadeh H, Ristovski Z and Arai M. The Role of Non-thermal Plasma Technique in NO_x Treatment: A review. Renewable and Sustainable Energy Reviews. Vol. 40, p. 886-901, 2014.

[7] Jolibois J, Takashima K and Mizuno A. Application of a Non-thermal Surface Plasma Discharge in Wet Condition for Gas Exhaust Treatment: NO_x Removal. Journal of Electrostatics, Vol. 70, No. 3, p. 300-308, 2012.

[8] Guan B, Zhan R, Lin H and Huang Z. Review of State of The Art Technologies of Selective Catalytic Reduction of NO_x from Diesel

Engine Exhaust. Applied Thermal Engineering. Vol. 66, No, 1-2, p. 395-414, 2014.

[9] Fujita K, Nochi K, Wakatsuki Y, Miyanagi A and Hiraoka N. Development of Selective Catalytic Reduction for Low-speed Marine Diesel Engines. Mitsubishi Heavy Industries Technical Review, Vol. 47, No. 3, p. 48-52, 2010.

[10] Azzara A, Rutherford D and Wang HF. Feasibility of IMO Annex VI Tier III Implementation Using Selective Catalytic Reduction. The International Council on Clean Transportation, 2014.

[11] Österman C and Magnusson M. A Systemic Review of Shipboard SCR Installations in Practice. WMU Journal of Maritime Affairs, Vol. 12, No. 1, p. 63-85, 2013.

[12] Hussain J, Palaniradja K, Algumurthi N and Manimaran R. Diesel Engine Emissions and After Treatment Techniques - A Review. Journal of Engineering Research and Studies, Vol. 3, No. 2, p. 34-44, 2012.

[13] Feasibility of IMO Annex VI Tier III Implementation Using SCR. ICCT Working Paper. 2014. Available from http://www.safety4sea.com/feasibility-of-imo-annex-vi-tier-iii-implementation-using-selective-catalytic-re/

[14] Briggs J. The Impact of Tier III NOx Regulation on the Shipping Industry. Bulletin, Vol. 109, No. 5, p. 22-25, 2014. Available from http://www.iaccsea.com/fileadmin/user_upload/pdf/b-5-14-impact_of_tier_iii_nox_regulation.pdf

[15] Hensel S. 2-stroke SCR. 2013. Available from http://wm.am.gdynia.pl/wp-content/uploads/2013/05/SCR_overview.pdf

[16] MAN Engines in Petrofacs Newbuild to Be SCR Equipped. Marinelog, 2014. Available from http://www.marinelog.com/index.php?option=com_k2&view=item&id=8196:man-engines-in-petrofacs-newbuild-to-be-scr-equipped&Itemid=227

[17] Wärtsilä NO_x Reducer. 2011. Available from http://www.wartsila.com/static/studio/assets/content/ss4/wartsila-nox-reducer-presentation.pdf

[18] DANSK TEKNOLOGI. BLUNOX SCR System Retrofitted on Royal Danish Navy Patrol Vessels. Available from http://www.dansk-teknologi.dk/home/scr-systems/scr-references/diana-class.html

[19] DANSK TEKNOLOGI. SCR Systems. Available from http://www.dansk-teknologi.dk/home/scr-systems/scr-system.html

[20] Johnson Matthey. SINOx® Emissions Control. 2009. Available from http://downloads.german-pavilion.com/downloads/pdf/exhibitor_17983.pdf

[21] Yu J. The Study of Urea Decomposition and Deposit Formation in Heavy Duty Diesel Engine SCR System. SAE Paper, C2010P193, 2010.

[22] Smeets RGH, Calis HP, Lugt PM and van den Bleek CM. Catalytic Removal of NO_x from Total Energy Installation Flue Gases: Process Design and Development. Catal Today, Vol. 29, No. 1, p. 133–137, 1996.

[23] Abu-Ramadan E, Saha K and Li XG. Modeling the Depleting Mechanism of Urea-Water-Solution Droplet for Automotive Selective Catalytic Reduction Systems. AIChE J, Vol. 57, No. 11, p.3210–3225, 2011.

[24] Lundström A, Andersson B and Olsson L. Urea Thermolysis Studied Under Flow Reactor Conditions Using DSC and FT-IR. Chem Eng J, Vol. 150, No. 2-3, p. 544–550, 2009.

[25] Yim SD, Kim SJ, Baik JH, Nam I, Mok YS, Lee JH, Cho B and Oh SH. Decomposition of Urea into NH_3 for the SCR Process. Ind Eng Chem Res, Vol. 43, No. 16, p. 4856–4863, 2004.

[26] Wang TJ, Baek SW and Lee SY. Experimental Investigation on Evaporation of Urea-Water-Solution Droplet for SCR Applications. AIChE J, Vol. 55, No. 12, p. 3267–3276, 2009.

[27] Koebel M, Elsener M and Kleemann M. Urea-SCR: A Promising Technique to Reduce NOx Emissions from Automotive Diesel Engines. Catal Today, Vol. 59, No. 3-4, p. 335–345, 2000.

[28] Koebel M, Madia G and Elsener M. Selective Catalytic Reduction of NO and NO_2 at Low Temperatures. Catal Today, Vol. 73, No. 3-4, p. 239–247, 2002.

[29] Ball JC. A Toxicological Evaluation of Potential Thermal Degradation Products of Urea. SAE Paper, 2001-01-3621, 2001.

[30] Koebel M and Strutz EO. Thermal and Hydrolytic Decomposition of Urea for Automotive Selective Catalytic Reduction Systems: Thermo Chemical and Practical Aspects. Ind Eng Chem Res, Vol. 42, No. 10, p. 2093–2100, 2003.

[31] Schaber PM, Colson J, Higgins S, Thielen D, Anspach B and Brauer J. Thermal Decomposition (Pyrolysis) of Urea in An Open Reaction Vessel. Thermochim Acta, Vol. 424, No. 1-2, p. 131–142, 2004.

[32] Schaber PM, Colson J, Higgins S, Dietz E, Thielen D, Anspach B and Brauer J. Study of the Urea Thermal Decomposition (Pyrolysis) Reaction and Importance to Cyanuric Acid Production. Am Lab, Vol. 31, No. 16, p. 13–21, 1999.

[33] Fang HL and DaCosta HFM. Urea Thermolysis and NO_x Reduction with and without SCR Catalysts. Appl Catal B Environ, Vol. 46, No. 1, p. 17–34, 2003.

[34] Stradella L and Argentero M. A Study of the Thermal Decomposition of Urea, of Related Compounds and Thiourea Using DSC and TG–EGA. Thermochim Acta, Vol. 219, Nol 27, p. 315–323, 1993.

[35] Kleemann M, Elsener M, Koebel M and Wokaun A. Hydrolysis of Isocyanic Acid on SCR Catalysts. Ind Eng Chem Res, Vol. 39, No. 11, p. 4120–4126, 2000.

[36] Alzueta MU, Bilbao R, Millera A, Oliva M and Ibanez JC. Impact of New Findings Concerning Urea Thermal Decomposition on the Modeling of the Urea SNCR Process. Energy Fuels, Vol. 14, No. 2, p. 509–510, 2000.

[37] Birkhold F, Meingast U, Wassermann P and Deutschmann O. Analysis of the Injection of Urea-Water-Solution for Automotive SCR DeNOx Systems: Modeling of Two-phase Flow and Spray / Wall-interaction. SAE Paper, 2006-01-0643, 2006.

[38] Birkhold F, Meingast U, Wassermann P and Deutschmann O. Modeling and Simulation of the Injection of Urea-Water-Solution for Automotive

SCR DeNOx-systems. Appl Catal B Environ, Vol. 70, No. 1-4, p. 119–127, 2007.

[39] Zanoelo EF. A Lumped Model for Thermal Decomposition of Urea Uncertainties Analysis and Selective Non-catalytic Reduction of NO. Chem Eng Sci, Vol. 64, No. 5, p. 1075–1084, 2009.

[40] Ebrahimian V, Nicolle A and Habchi C. Detailed Modeling of the Evaporation and Thermal Decomposition of Urea-Water-Solution in SCR systems. AIChE J, Vol. 58, No. 7, p. 1998–2009, 2012.

[41] Ström H, Lundström A and Andersson B. Choice of Urea-spray Models in CFD Simulations of Urea-SCR Systems. Chem Eng J, Vol. 150, No. 1, p. 69–82, 2009.

[42] Stiesch G. Modeling Engine Spray and Combustion Processes. Springer Verlag Berlin Heidelberg, New York, p. 173, 2003.

[43] Samimi Abianeh O and Chen CP. Modelling of Evaporation and Dissolution of Multicomponent Oil Droplet in Shallow Water. WIT Transactions on Engineering Sciences, Vol. 75, p. 231-242, 2012.

[44] Som SK. Introduction to Heat Transfer. PHI Learning Private Limited, New Delhi, p. 503, 2008.

[45] Oh TY, Ko JH, Seong HJ and Min BS. Design Optimization of the Mixing Chamber in SCR System for Marine Diesel Engine. In: Proceedings of the 6th International Symposium on Diagnostics and Modeling of Combustion in Internal Combustion Engines, Vol 6, p. 87–92, 2004.

[46] Sun WH, Boyle JM, Carmignani PG and Sassenrath JM. Small Scale Test Results from New Selective Catalytic NO_x Reduction Process Using Urea. In: Proceedings of the MEGA Symposium, Chicago, 2001.

[47] Calabrese JL, Patchett JA, Grimston K, Rice GW and Davis GW. The Influence of Injector Operating Conditions on the Performance of a Urea–Water Selective Catalytic Reduction (SCR) System. SAE Paper, 2000-01-2814, 2000.

[48] Wurzenberger JC and Wanker R. Multi-scale SCR Modeling, 1D Kinetic Analysis and 3D System Simulation. SAE Paper, 2005-01-0948, 2005.

[49] Schiller L and Naumann AZ. A Drag Coefficient Correlation. VDI, Vol. 77, p. 318–320, 1993.

[50] Tian FZ, Tao YJ, Su LY and Zhou J. Multicomponent Droplet Evaporation Model and Experimental Study. Journal of Propulsion Technology, Vol. 12, No. 6, p. 568-571, 2006.

[51] Ray AK, Davis EJ and Ravindran P. Determination of Ultra-low Vapor Pressures by Submicron Droplet Evaporation. J. Chem. Phys, Vol. 71, No. 2, p. 582-587, 1979.

[52] Kolaitis DI and Founti MA. A Study of Numerical Models for Eulerian-Lagrangian Simulations of Turbulent Evaporating Sprays. International Journal of Heat and Fluid Flow, Vol. 27, p. 424-435, 2006.

[53] Wan JH, Liu SL and Yang YG. Theory and Properties of Fluid Molecule. (In Chinese). Harbin Engineering University Publishing House, p. 377-469, 1994. In: Effect of Ambient Pressure and Thermal Environment on Single Droplet Evaporation. (In Chinese). Master Thesis, p. 21, 2007.

[54] Xu JL, Chen TK and Chen XZ. A Study of Water-Drop Evaporation Constants. (In Chinese). J Eng Therm Energy Power, Vol. 7, No. 5, p. 268–271, 1992.

[55] Ghanem A, Lemenand T, Della Valle D and Peerhossaini H. Static Mixers: Mechanisms, Applications, and Characterization Methods – A Review. Chem Eng Res Des, Vol. 92, No. 2, p. 205-228, 2014.

[56] Thakur RK, Vial C, Nigam KDP, Nauman EB and Djelveh G. Static Mixers in the Process Industries—A Review. Chem Eng Res Des, Vol. 81, No. 7, p. 787-826, 2003.

[57] Hobbs DM and Muzzio FJ. Optimization of a Static Mixer Using Dynamical Systems Techniques. Chem Eng Sci, Vol. 53, No. 18, p. 3199–3213, 1998.

[58] Habchi C, Lemenand T, Della Valle D and Peerhossaini H. Alternating Mixing Tabs in Multifunctional Heat Exchanger Reactor. Chem Eng Process: Process Intensification, Vol. 49, No. 7, p. 653–661, 2010.

[59] Allocca PT. Mixing Efficiency of Static Mixing Units in Laminar Flow. Fiber Prod, Vol. 8, p.12–18, 1982.

[60] Rauline D, Leblevec JM, Bousquet J and Tanguy PA. A Comparative Assessment of the Performance of the Kenics and SMX Static Mixers. Chem Eng Res Des, Vol. 78, No. 3, p. 389–396, 2000.

[61] Theron F and Sauze NL. Comparison between Three Static Mixers for Emulsification in Turbulent Flow. Int J Multiphase Flow, Vol. 37, No. 5, p. 488–500, 2011.

[62] Lisboa PF, Fernandes J, Simões PC, Mota JPB and Saatdjian E. Computational-fluid-dynamics Study of A Kenics Static Mixer as A Heat Exchanger for Supercritical Carbon Dioxide. J Supercrit Fluids, Vol. 55, No. 1, p. 107–115, 2010.

[63] Rahmani RK, Keith TG and Ayasoufi A. Numerical Study of the Heat Transfer Rate in A Helical Static Mixer. J Heat Transfer, Vol. 128, No. 8, p. 769–783, 2006.

[64] Visser JE, Rozendal PF, Hoogstraten HW and Beenackers AACM. Three-dimensional Numerical Simulation of Flow and Heat Transfer in the Sulzer SMX Static Mixer. Chem Eng Sci, Vol. 54, No. 13–14, p. 2491–2500, 1999.

[65] Regner M, Östergren K and Trägårdh C. Effects of Geometry and Flow Rate on Secondary Flow and the Mixing Process in Static Mixers–A Numerical Study. Chem Eng Sci, Vol. 61, No. 18, p. 6133–6141, 2006.

[66] Liu H, Guo T, Yang Y and Lu G. Optimization and Numerical Simulation of the Flow Characteristics in SCR System. Energy Procedia, Vol. 17, Part A, No. 0, p. 801-812, 2012.

[67] Pahl MH and Muschelknautz E. Static Mixers and Their Applications. Int Chem Eng, Vol. 22, No. 2, p. 197–205, 1982.

[68] Lang E, Drtina P, Streiff F and Fleischli M. Numerical Simulation of the Fluid Flow and the Mixing Process in A Static Mixer. Int J Heat Mass Transfer, Vol. 38, No. 12, p. 2239–2250, 1995.

[69] Jensen-Holm H, Topsøe NY and Cui JJ. Implementation of SCR DeNOx Technology on Coal-Fired Boilers in P.R. China. 2006. Available from http://www.topsoe.com/file/implementation-scr-denox-technology-coal-fired-boilers-pr-china

[70] Sulzer Chemtech, Mixing and Reaction Technology. Available from http://www.denwel.cz/editor/filestore/File/Leaflets/Sulzer/01%20Mixing_and_Reaction_Tech-e.pdf

[71] Alstom Power. SCR IsoSwirlTM Mixer and High Efficiency Ammonia Injection. 2015. Available from http://www.alstom.com/Global/Power/Resources/Documents/Brochures/aqcs-scr-isoswirl-mixer-ammonia-injection.pdf

[72] Grosz-Röll F. Assessing Homogeneity in Motionless Mixers. Int Chem Eng, Vol. 20, No. 4, p. 8, 1980.

[73] Kukukova A, Aubin J and Kresta SM. A New Definition of Mixing and Segregation: Three Dimensions of A Key Process Variable. Chem Eng Res Des, Vol. 87, No. 4, p. 633-647, 2009.

[74] Song X, Naber J and Johnson HJ. Nonuniformity and NO_2/NO_x Ratio Effects on the SCR Performance under Transient Engine Conditions. SAE Paper 2014-01-1556. 2014.

[75] Wadley R and Dawson MK. LIF Measurements of Blending in Static Mixers in the Turbulent and Transitional Flow Regimes. Chem Eng Sci, Vol. 60, No. 8–9, p. 2469–2478, 2005.

[76] Hobbs DM, Swanson DP and Muzzio FJ. Numerical Characterizeation of Reynolds Number Flow in the Kenics Static Mixer. Chem Eng Sci, Vol. 53, No. 8, p.1565–1584, 1998.

[77] Kumar V, Shirke V and Nigam KDP. Performance of Kenics Static Mixer over A Wide Range of Reynolds Number. Chem Eng J, Vol. 139, No. 2, p. 284–295, 2008.

[78] Tian XN, Xiao YH, Zhou PL and Zhang WP. Study on the Mixing Performance of Static Mixers in Selective Catalytic Reduction (SCR) Systems. J Mar Eng Technol, Vol. 14, No. 2, p. 57-60, 2015.

[79] Lantec. Monolith Ceramic Catalyst Substrates. Available from http://www.lantecp.com/products/monolith/

[80] Chen JW, Yang H, Wang N, Ring Z and Dabros T. Mathematical Modeling of Monolith Catalysts and Reactors for Gas Phase Reactions. Appl Catal A: General, Vol. 345, No. 1, p. 1-11, 2008.

[81] Fogler HS. Elements of Chemical Reaction Engineering. 4th ed. Prentice Hall, p. 656-657, 2005.

[82] Marbán G, Valdés-Solís T, and Fuertes AB. Mechanism of Low-temperature Selective Catalytic Reduction of NO with NH_3 over Carbon-supported Mn_3O_4 Role of Surface NH_3 species: SCR Mechanism. Journal of Catalysis, Vol. 226, p. 138-155, 2004.

[83] Wang FJ. Computational Fluid Dynamic Analysis -- CFD Software Mechanism and Application. Tsinghua University Press, p. 11, 2004. (In Chinese)

[84] Shamim T, Shen H, Sengupta S, Son S and Adamczyk AA. A Comprehensive Model to Predict Three-way Catalytic Converter Performance. J Eng Gas Turbines Power, Vol. 124, No. 2, p. 421-428, 2002.

[85] Zukerman R, Vradman L, Herskowitz M, Liverts E, Liverts M, Massner A, Weilbel M, Brilhac JF, Blakeman PG and Peace LJ. Modeling and Simulation of A Smart Catalytic Converter Combining NO_x Storage, Ammonia Production and SCR. Chem Eng J, Vol. 155, No. 1-2, p. 419-426, 2009.

[86] Santos H, Costa M. Modelling Transport Phenomena and Chemical Reactions in Automotive Three-way Catalytic Converters. Chem Eng J, Vol. 148, No. 1, p. 173-183, 2009.

[87] Siemund S, Leclerc JP, Schweich D, Prigent M and Castagna F. Three-way Monolith Converter: Simulations versus Experiments. Chem Eng Sci, Vol. 51, No. 15, p. 3709–3720, 1996.

[88] Lee ST, Aris R. On the Effects of Radiative Heat Transfer in Monoliths. Chem Eng Sci, Vol. 32, No. 8, p. 827–837, 1977.

[89] Wanker R, Raupenstrauch H, Staudinger G. A Fully Distributed Model for the Simulation of A Catalytic Combustor. Chem Eng Sci, Vol. 55, p. 4709–4718, 2000.

[90] Upadhyay D and Nieuwstadt MV. Modeling of A Urea SCR Catalyst with Automotive Applications. Proceedings of IMECE2002, p. 707-713, New Orleans, Louisiana, 2002.

[91] Bröer S and Hammer T. Selective Catalytic Reduction of Nitrogen Oxides by Combining A Non-thermal Plasma and A V_2O_5-WO_3/TiO_2 Catalyst. Appl Catal B: Environmental, Vol. 28, No. 2, p. 101-111, 2000.

[92] Schär CM. Control of A Selective Catalytic Reduction Process. PhD thesis, Swiss Federal Institute of Technology, 2003.

[93] Colombo M, Nova I, Tronconi E, Schmeißer V, Bandl-Konrad B and Zimmermann L. NO/NO_2/N_2O–NH_3 SCR Reactions over A Commercial Fe-zeolite Catalyst for Diesel Exhaust Aftertreatment: Intrinsic Kinetics and Monolith Converter Modelling. Appl Catal B: Environmental, Vol. 111– 112, p. 106– 118, 2012.

[94] Colombo M, Nova I and Tronconi E. Detailed Kinetic Modeling of the NH_3–NO_2 SCR Reactions over A Commercial Cu-zeolite Catalyst for Diesel Exhausts After Treatment. Catal Today, Vol. 197, No. 1, p. 243–255, 2012.

[95] Joshi SY, Kumar A, Luo JY, Kamasamudram K, Currier NW and Yezerets A. Combined Experimental and Kinetic Modeling Study of the Bi-modal NOx Conversion Profile on Commercial Cu-SAPO-34 Catalyst under Standard SCR Conditions. Appl Catal B: Environmental, Vol. 165, p. 27–35, 2015.

[96] Supriyanto, Wijayanti K, Kumar A, Joshi S, Kamasamudram K, Currier NW, Yezerets A and Olsson L. Global Kinetic Modeling of Hydrothermal Aging of NH_3-SCRover Cu-zeolites. Appl Catal B: Environmental, Vol. 163, p. 382–392, 2015.

[97] Metkar PS, Harold MP and Balakotaiah V. Experimental and Kinetic Modelling Study of NH_3-SCR of NOx on Fe-ZSM-5, Cu-chabazite and Combined Fe- and Cu-zeolite Monolithic Catalysts. Chem Eng Sci, Vol. 87, p. 51–66, 2013.

[98] Lietti L, Nova I, Camurri S, Tronconi E and Forzatti P. Dynamics of the SCR-DeNOx Reaction by the Transient-Response Method. AIChE J, Vol. 43, No. 10, p. 2559-2570, 1997.

[99] Nova I, Lietti L, Tronconi E and Forzatti P. Transient Response Method Applied to the Kinetic Analysis of the DeNOx-SCR Reaction. Chem Eng Sci, Vol. 56, No. 4, p. 1229-1237, 2001.

[100] Auvray X, Partridge W, Choi J, Pihl J, Coehlo F, Yezerets A, Kamasamudram K, Currier N and Olsson L. Kinetic Modeling of NH_3-SCR over A Supported Cu Zeolite Catalyst Using Axial Species Distribution Measurements. Appl Catal B: Environmental, Vol. 163, p. 393–403, 2015.

[101] Wang TJ, Baek SW, Kwon HJ, Kim YJ, Nam I, Cha M and Yeo GK. Kinetic Parameter Estimation of a Commercial Fe-Zeolite SCR. Ind Eng Chem Res, Vol. 50, No. 5, p. 2850–2864, 2011.

[102] Devarakonda MN. Dynamic Modelling, Simulation and Development of Model-based Control Strategies in A Urea-SCR Aftertreatment System in Heavy Duty Diesel Engines. PhD Thesis, Michigan Technological University, 2008.

[103] Upadhyay D and Nieuwstadt MV. Model Based Analysis and Control Design of A Urea-SCR DeNOx Aftertreatment System. Journal of Dynamic Systems, Measurement, and Control, Vol. 128, No. 3, p. 737-741, 2006.

[104] Delphi. Engine and Transmission. Available from http://www.delphi.com/manufacturers/auto/sensors/engine-and-transmission/diesel/ammonia

[105] Young KD and Özgűner Ü. Frequency Shaping Compensator Design for Sliding Mode. International Journal of Control, Vol. 57, No. 5, p. 1005–1019, 1993.

[106] Tseng ML and Chen MS. Chattering Reduction of Sliding Mode Control by Low-pass Filtering the Control Signal. Asian J Control, Vol. 12, No. 3, p. 392-398, 2010.

[107] Tang GY, Zhang BL and Ma H. Feedforward and Feedback Optimal Control for Linear Discrete Systems with Persistent Disturbances. International Conference on Control, Automation, Robotics and Vision. Vol. 3, p. 1658-1663, 2004.

[108] Ni ML. Existence Condition on Solutions to the Algebraic Riccati Equation. Acta Automatica Sinica, Vol. 32, No. 1, p. 85-87, 2008.

[109] Song Q and Zhu G. Model-based Closed-loop Control of Urea SCR Exhaust Aftertreatment System for Diesel Engine. SAE paper, 2002-01-0287, 2002.

[110] Hsieh MF. Control of Diesel Engine Urea Selective Catalytic Reduction Systems. PhD thesis, The Ohio State University, 2010.

[111] Kubinski DJ and Visser JH. Sensor and Method for Determining the Ammonia Loading of A Zeolite SCR Catalyst. Sensor and Actuator B: Chemical, Vol. 130, No. 1, p. 425-429, 2008.

[112] Hsieh MF and Wang JM. Nonlinear Observer Designs for Diesel Engine Selective Catalytic Reduction (SCR) Ammonia Coverage Ratio Estimation. Proceedings of the 48th IEEE Conference on Decision and Control and 28th Chinese Control Conference, p. 6596-6601, 2009.

[113] Chen PG and Wang JM. Sliding-mode Observers for Urea Selective Catalytic Reduction System State Estimations Based on Nitrogen Oxide Sensor Measurements. Proceedings of the Institution of Mechanical Engineers, Part D: Journal of Automobile Engineering, Vol. 229, No. 7, p. 835-849, 2015.

Appendix 1.

SCR EXPERIMENTAL TEST RIG

Two SCR experimental test rigs are established at Harbin Engineering University in China. One is used for modelling of the SCR reactor and verification of the NO_x conversion efficiency whilst the other is used for investigating the formulae of catalysts and the NH_3 cross-sensitivity of NO_x sensors. The former SCR experimental test rig is designed for a 4-storke marine diesel engine (Model: Weichai X6170ZC-05W). The rated power and speed of the diesel engine are 300 kW and 1000 r/min respectively. The SCR system is placed after the turbine of the turbocharger (Model: SJ140B). The engine load is set by a hydraulic dynamometer (Model: SG1600).

The main components of the SCR experimental test rig built include a reactor, static mixers, urea injection system and a control unit. The reactor is arranged horizontally. The size (3m×0.8m×0.8m) of the reactor is designed to be able to load catalysts with a maximum of 3 layers. However, only 2 layers of catalysts are installed in the reactor for the test rig according to the characteristics of the exhaust gas and the desired NO_x reducing rate. Guide plates are placed at the entrance of the reactor in order to distribute the flow of exhaust gas evenly. The use of the guide plates is beneficial to achieving a high NO_x conversion efficiency. Static mixers are used in the pipelines before the reactor in order to promote the mixing of exhaust and NH_3. Soot blowers are equipped above each layer of catalysts to prevent catalyst degradation due to the accumulation of soot after a long working period. The urea injection system comprises a urea solution tank, a dosing pump, an air compressor and a nozzle. A programmable logic controller (PLC) (Model: SIEMENS PLC

S7-300) is used as the control unit which calculates the amount of urea desired based on either open or closed-loop control strategies according to the characteristics of exhaust gas. The dosing signal from the PLC is thus transferred into the dosing pump to inject UWS at an appropriate rate. 2 NO_x sensors (Model: SIEMENS NGK 'Smart NO_x sensor') and 2 NO analysers (UNISEARCH DOAS NO analyser) are used to measure the NO_x concentration and NO concentration in exhaust gas before and after the reactor respectively. 2 NH_3 analysers (Model: UNISEARCH LasIR R NH_3 online analyser) are used to measure the NH_3 concentration in exhaust gas before and after the reactor. The exhaust temperature is measured by thermocouples. The SCR experimental test rig for the diesel engine of 300 kW is presented below:

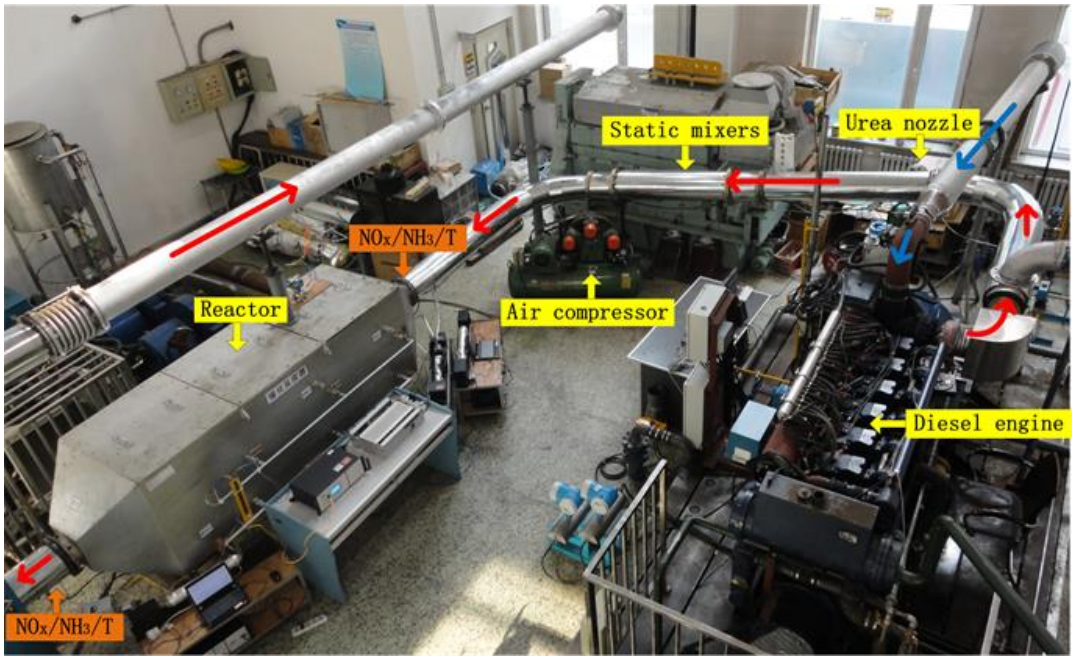

SCR experimental test rig for diesel engine of 300 kW

The other SCR experimental test rig is designed for a diesel generator (Model: KIPOR KDE40ST3) with the rated output of 38 kW. Apart from the components introduced above, an additional electrical heater is used in the pipeline in order to enhance the exhaust temperature. The SCR experimental test rig for the diesel generator of 38 kW is presented below:

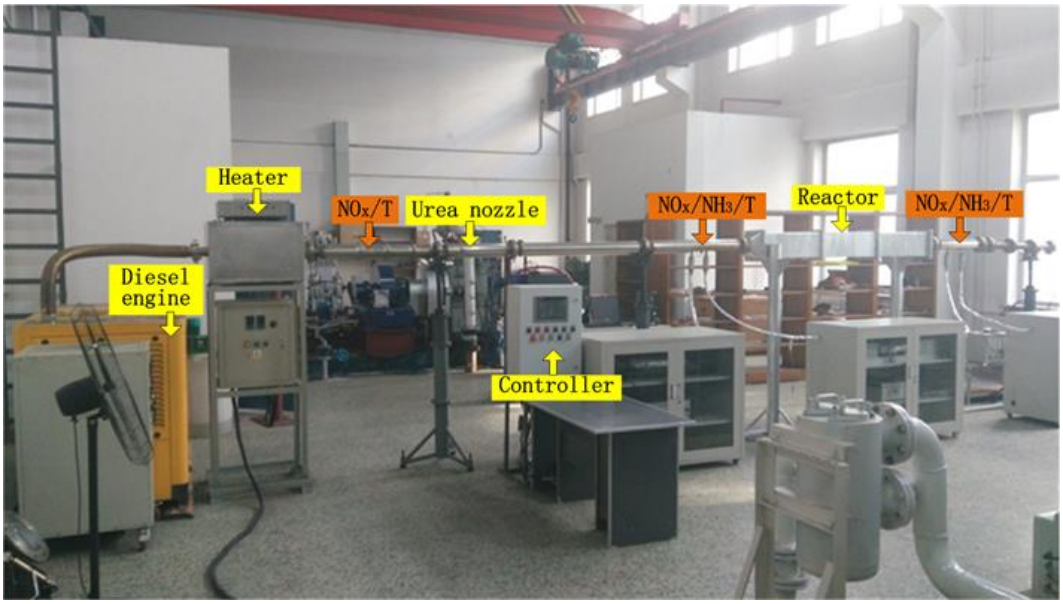

SCR experimental test rig for diesel generator of 38 kW

Appendix 2.

CATALYST PARAMETERS IN SCR REACTOR MODELLING

Parameter	Unit	Value
Number of monolith element	---	32
Cross section of monolith element	mm	150×150
Length of monolith element	mm	450
Number of openings in monolith element	---	30×30
Size of opening	mm	4×4
Heat capacity of monolith	J/(kg.K)	1054
Density of monolith	kg/m^3	1798

Appendix 3.

COMPARISON OF UREA CONTROL STRATEGIES

Comparison of urea control strategies under steady state engine operating points of 25% load (75 kW) and 100% load (300 kW)

Control strategy	Average NH_3 slip (ppm)	Peak NH_3 slip (ppm)	Average NO residual (ppm)	Total urea consumption (L)
NO sliding mode	16.0	36.5	243	26.47
NH_3 sliding mode	9.5	10.7	224	28.44
Optimal control	6.5	12.0	266	24.24

Comparison of urea control strategies under steady state engine operating points of 50% load (150 kW) and 75% load (225 kW)

Control strategy	Average NH_3 slip (ppm)	Peak NH_3 slip (ppm)	Average NO residual (ppm)	Total urea consumption (L)
NO sliding mode	10.4	20.0	224	19.26
NH_3 sliding mode	9.5	10.4	234	18.53
Optimal control	7.9	10.8	261	16.68

Comparison of urea control strategies under under transient state engine operating condition

Control strategy	**Average NH_3 slip (ppm)**	**Peak NH_3 slip (ppm)**	**Average NO residual (ppm)**	**Total urea consumption (L)**
NO sliding mode	9.9	20.0	159	31.66
NH_3 sliding mode	9.5	10.4	162	31.29
Optimal control	7.2	10.9	201	26.84